

1 We thank the referees for their reviews, which were instrumental in making a much  
2 improved manuscript. In response, we have made changes where we felt they were warranted,  
3 and gave replies to all comments. In this response, all of the page and line numbers for  
4 corrections refer to the revised manuscript, while we keep page and line numbers intact from  
5 the original reviews. The manuscript diff document is consistent with the changes described  
6 below.

## 7 1 Responses to Anonymous Referee #1

8 1. *MAJOR COMMENT: Level of Detail: Extensive details associated with the mathemat-*  
9 *ical relationships associated with four dimensional data assimilation will likely reduce*  
10 *the overall target audience. While the air quality community is interested in methods*  
11 *to improve emission estimates, I would expect that much of those details will not be*  
12 *of much interest to the same community. More importantly, it was not clear whether*  
13 *the details on the adjoint are the same as those presented previously in the literature*  
14 *or whether they are new. If the relationships are typical of those of previous adjoint*  
15 *papers, perhaps more of the details could be put into the appendix. The authors should*  
16 *more clearly differentiate what is new and what is not new.*

17 **AUTHOR RESPONSE:** We have reorganized the Introduction and Section 2.3  
18 extensively and added clarifying introductions and transitions to guide the general  
19 audience. Although we still retain significant mathematical details, these are limited  
20 to those necessary for understanding how this approach is different than previous ones,  
21 how the results are obtained, and what those results mean. The unique challenge of the  
22 theoretical portion of this work was in applying an additive preconditioned incremental  
23 4D-Var approach to log-normal control variables. Mutliplicative incremental 4D-Var  
24 for log-normal control variables was discussed in detail by Fletcher and Jones (2014).

### 25 **Manuscript changes:**

26 The Introduction has been modified to include the following: “The modifications to  
27 that system that are required for this work are described in Sec. 2 as well as in Guerrette  
28 and Henze (2015) (GH15). These include new linearized model descriptions (GH15),  
29 memory and I/O trajectory management (GH15), a log-normal emission control vari-  
30 able (Sec. 2.3.2), calculation of posterior variance (Sec. 2.3.4), and improvements to  
31 the Gauss-Newton optimization algorithm to handle nonlinearities (Sec. 2.3.5). As  
32 described in GH15, this approach of assimilating chemical tracer observations in a re-  
33 gional numerical weather prediction and chemistry model is unique in the context of  
34 previous 4D-Var flux constraints.”

35 We combined the opening to Section 2.3 with Sections 2.3.1 and 2.3.3 in a more logical  
36 flow. We now start new Section 2.3.1 with incremental 4D-Var instead of the more  
37 fundamental derivation that is well-known from previous literature. p12, line 2: added  
38 a sentence for clarity on posterior covariance; “While areas where uncertainty has been  
39 reduced from the prior include new information from the observations, areas without  
40 uncertainty reduction are simply a new realization of the prior.”

41 Section 2.3.2 is split. One half is merged with the description of lognormal emissions  
42 (new Sec. 2.3.2). The other is separated into its own subsection that deals with Gaus-  
43 sian errors (new Sec. 2.3.3). The subsections are also reorganized and include new  
44 transition sentences to help clarify why we are discussing specific details and also what  
45 is new versus old. Much of the details in section 2.3.5 have now been removed.

- 46 2. *MAJOR COMMENT: As described in a few of my specific comments, the discussion of*  
47 *what type of observations would be desirable to further constrain the adjoint technique*  
48 *and improve the emission estimates. The aircraft flights that targeted the fires were*  
49 *obviously critical, but would other flight paths be more useful? Or would more cases be*  
50 *useful? Were there only two periods during ARCTAS-CARB that were useful, or were*  
51 *the number of cases examined more limited by the computational expense of adjoint*  
52 *techniques?*

53 **AUTHOR RESPONSE:**

54 There were four flights during the California portion of ARCTAS (20, 22, 24, and 26  
55 June). The 20 June flight characterized Northern California anthropogenic sources  
56 before the fires started. The 26 June flight only flew over California for 3 hours,  
57 and then transited to the next base of operations. The 22 and 24 June observations  
58 were across longer durations and influenced significantly by BB sources. There was  
59 no underlying limitation of 4D-Var that prevented using the other flights, but those  
60 observations were limited in terms of the amount of information they contained about  
61 BB sources, which was our primary interest. We added some of these details to the  
62 manuscript.

63 **Manuscript changes:**

64 pp13, line 21: Addition; “The 20 June flight of ARCTAS-CARB characterized Northern  
65 California anthropogenic sources, but was not influenced by fires.”

66 pp13, line 24: Modification; “The 24 June flight passed back and forth in the downwind  
67 region between Los Angeles and San Diego, measuring the outflow from those cities and  
68 the transportation between them, and 1 day old diluted BB outflow from the north.”

- 69 3. *MAJOR COMMENT: The authors acknowledge that other meteorological factors will*  
70 *affect their analysis. They also mention that mostly clear skies were observed over*  
71 *California, so that complex cloud processes (i.e. wet removal) did not occur in this*  
72 *study. Near the end of the paper they mention it would be useful to have even simpler*  
73 *meteorological conditions to reduce uncertainties in meteorology. But it would seem*  
74 *very difficult to find such cases and one would have to confront complex real-world*  
75 *conditions at some point anyway.*

76 **AUTHOR RESPONSE:** Please see response to “Specific Comment” 19

- 77 1. *Specific Comment: Title: ARCTAS is misspelled.*

78 **Manuscript changes:** The title is corrected.

- 79 2. *Specific Comment: Page 1, line 7: Consider changing “multiple” to “three”. The next*  
80 *line lists 3 inventories.*

81 **Manuscript changes:** We changed “multiple” to “three”.

- 82 3. *Specific Comment: Page 1, line 9: Change the use of “×” and through out the text*  
83 *to write out what they actually mean in terms of a change. I find the usage in this*  
84 *particular sentence to be confusing.*

85 **AUTHOR RESPONSE:** We agree that several of the instances of “×” are difficult  
86 to comprehend. We added terminology in both the abstract and the first paragraph  
87 to introduce × to mean “a factor of”, as in a factor of 2 to 3 (×2 to ×3. Anywhere  
88 this exact phrasing does not fit, we have fixed the text. We also rearranged some other  
89 sentences with this vernacular for ease of reading.

90 **Manuscript changes:** The following sentences are modified:

91 ORIGINAL p1,line9: p1, line 9: “On 22 June, aircraft observations are able to reduce  
92 the spread between a customized QFED inventory and FINNv1.0 from a factor of 3.5  
93 (×3.5) to only ×2.1.”

94 p2, line 10: “Zhang et al. (2014a) concluded that diffusion and loss mechanisms  
95 limit the corresponding responses of domain-wide aerosol burden, AOD, and 2 m  
96 temperature to ×2-3.”

97 p2, line 4: “Bond et al. (2013) cite several inventories of annual U.S. non-BB BC  
98 sources, which are between 260 to 440 Gg yr<sup>-1</sup>, yielding a maximum to minimum ratio  
99 of 1.7.”

100 p14, line 33: “...plus the adjoint (×10 longer than the nonlinear model), the cost of  
101 incremental 4D-Var is approximately ×600 more than that of a single forward simula-  
102 tion...”

- 103 4. *Specific Comment: Page 3, lines 25-35: The motivation of why ARTCAS-CARB cam-*  
104 *campaign is used for their analysis should be improved. The way the paragraph is phrased,*  
105 *it basically just says they are going to use this particular campaign. But this could be*  
106 *changed to upfront state that the campaign had aircraft measurements characterizing*  
107 *both anthropogenic and biomass burning sources of BC and therefore would be useful*  
108 *to test their adjoint-based technique.*

109 **Manuscript changes:** We divided this long paragraph into three smaller ones, and  
110 add language to clarify why we used ARCTAS-CARB.

- 111 5. *Specific Comment: Page 4, line 17: Change “also turned off” to something else. Since*  
112 *it is not available, it is not possible to turn off that option. Also large fires could*  
113 *significantly affect meteorology by dramatically reducing incoming shortwave radiation,*  
114 *so some of the uncertainties in the adjoint technique will be due to this process that is*  
115 *neglected — in addition to the other meteorological processes they note.*

116 **Manuscript changes:** p4, line 3: Modification; “Microphysical and radiative re-  
117 sponses to online aerosols are not taken into account for GOCART aerosols in WRF-  
118 Chem.”

- 119 6. *Specific Comment: Page 4,line 32: The grid spacing of 18 km is rather coarse, espe-*  
120 *cially in resolving terrain-induced circulations in California. There have been numerous*

121 *studies on this subject for California, and it would be useful to point that out. Although*  
122 *not explicitly stated here, the choice of coarse grid spacing is likely due to the compu-*  
123 *tation cost of the adjoint-based technique.*

124 **AUTHOR RESPONSE:** We added the following paragraph as this is an impor-  
125 tant consideration for future work. Please see the updated document for appropriate  
126 references.

127 **Manuscript changes:** “Our horizontal grid spacing was chosen to balance the wall-  
128 time and memory requirements of 4D-Var with model accuracy, and the ACM2 PBL  
129 option was chosen to reduce ADM and TLM development efforts. Angevine et al.  
130 (2012) recommend that the complex terrain in California demands fine tuning of the  
131 WRF horizontal grid spacing, PBL, LSM, and reanalysis initialization. Among other  
132 conclusions, those authors found that at six surface sites near the land-ocean boundary  
133 a 4 km and a 12 km simulation with similar settings had mean wind speed biases of (0.15  
134 to 1.5)  $\text{m s}^{-1}$  and (-0.38 to 1.9)  $\text{m s}^{-1}$ , respectively. Supporting that conclusion, Strand  
135 et al. (2012) used a 36 km resolution chemical transport model (CTM), with offline  
136 meteorology, and found significant negative mean fractional bias (MFB) in modeled  
137  $\text{PM}_{2.5}$  relative to surface observations of fires within narrow Northern California valleys  
138 in July 2008 (MFB=-34.95%) and during autumn 2007 Santa Ana winds (MFB=-  
139 110.22%). During the July 2008 episode, their CTM predictions had a smaller positive  
140 bias (MFB=+21.88%). Therefore, we would expect similar wind and concentration  
141 biases at 18 km resolution, which may or may not be improved by online meteorology.  
142 Incremental 4D-Var provides an opportunity to utilize a different model configuration  
143 (e.g., resolution) for the NLM comparisons of model to observations than that used for  
144 the ADM and TLM simulations. The adaptation of that capability from meteorological  
145 (i.e., Zhang et al., 2014b) to chemical simulations and the subsequent testing is reserved  
146 for future WRFDA-Chem developments.”

- 147 7. *Specific Comment: Page 5, line 5: I could be wrong, but I thought the FINN emissions*  
148 *provided emissions per fire (i.e. point) that did not provide a spatial information on*  
149 *the size of the fire.*

150 **AUTHOR RESPONSE:** According to Wiedinmyer et al. (2011), each fire source is  
151 assumed to cover the entire  $1 \text{ km} \times 1 \text{ km}$  MODIS pixel from which the fire detection  
152 was captured. This area ( $1 \text{ km}^2$ ) is assumed equal to the burned area for that day,  
153 which is used to calculate emissions. There is an exception for grassland/savannas,  
154 which has an assumed area of  $0.75 \text{ km}^2$ , and also when the MODIS VCF product  
155 includes non-zero fractional bare cover for a pixel.

- 156 8. *Specific Comment: Page 5, line 13: I am skeptical of scaling the AOD based on a known*  
157 *high bias in GEOS-5. The bias is not necessarily linearly related to emissions. The*  
158 *problem in AOD in GEOS-5 could be a host of issues, such as representing the right*  
159 *mix of scattering and absorbing aerosols, water uptake of aerosols, and the treatment*  
160 *of aerosol optical properties.*

161 **AUTHOR RESPONSE:** We also don't believe that the GEOS-5 AOD scaling should  
162 give perfect emissions. Still, we wanted to compare these inventories following the



163 methodologies proposed by their creators to see if one has an advantage over the  
164 other. Although we made several modifications when inconsistencies arose with either  
165 observations (AOD for QFED) or known environmental behavior (diurnal pattern of  
166 sunlight), we feel that those fixes were not outside the intentions of those developers.  
167 We added the following paragraph to clarify the corrections we made to the inventories.

168 **Manuscript changes:** p5, line 29-32: Addition; “Any inverse modeling study that  
169 depends on the first guess should start in a region of high probability. In a Bayesian  
170 inversion, the first guess should be unbiased on average. Here we address several  
171 known errors in our prior inventories that we either fix or are unable to fix. All  
172 changes are consistent with either observations or the intended physical descriptions  
173 of the inventories.”

- 174 9. *Specific Comment: Page 6, lines 5-9: Figure 2 shows the location of the MODIS fires,*  
175 *but the discussion is more about the shifts in the fires in the datasets. The text somehow*  
176 *implies Figure 2 illustrates those shifts, which it does not. Please change the text to*  
177 *clarify.*

178 **AUTHOR RESPONSE:** We chose poor colors for Figure 2. In the new figure, the  
179 difference between FINN and QFED gridded emissions is much clearer, especially due  
180 to the zoomed in map.

181 **Manuscript changes:** Replaced Figure 2.

- 182 10. *Specific Comment: Page 14, line 9:the use of “swept out” should be changed. Implies*  
183 *the winds pushed the aircraft over the ocean as opposed to a choice by the scientists or*  
184 *aircraft crew.*

185 **Manuscript changes:** p13, line 21: Modification; “ disembarked from Los Angeles,  
186 swept out over the ocean” changed to “embarked from Los Angeles, transited the  
187 off-shore Pacific inflow”

- 188 11. *Specific Comment: Page 14, lines 3-14: Suggest including the aircraft flight paths in*  
189 *Figure 2 to illustrate the discussion in this paragraph.*

190 **AUTHOR RESPONSE:** The flightpath is added.

191 **Manuscript changes:** Replaced Figure 2.

- 192 12. *Specific Comment: Page 14, line 18: Do you mean “Average” or “re-average”? They*  
193 *mention the 10-s data in the previous sentence, so perhaps that is a 10-s average? If*  
194 *that is the case, the text does not say so. The 90-s averaging is acknowledging the*  
195 *mismatch between the observations and the temporal resolution of the model. What*  
196 *I found missing was a discussion on the mismatch in spatial resolution, or does that*  
197 *even matter in the adjoint technique used? The model grid cell is 18 km, so it cannot*  
198 *resolve small-scale variation, so shouldn't the data be averaged to 18 km intervals?*

199 **AUTHOR RESPONSE:** We intended to say “re-average”. That procedure is de-  
200 scribed in Section 5.1.2 of Guerrette and Henze (2015): “The 10 s resolution ARCTAS  
201 observations of BC concentration, pressure, latitude, and longitude are averaged to  
202 the 90 s model time step, which is approximately the time the DC-8 would take to

203 traverse a single  $18 \text{ km} \times 18 \text{ km}$  column. However, the 10 s resolution ARCTAS BC  
204 concentrations are revision 2 (R2), while a later revision 3 (R3) product was released  
205 at 60 s resolution only. The later revision includes additional mass in the 50-900 nm  
206 size range as a result of applying a lognormal fit. In order to utilize this improved  
207 product, as well as leverage the finer resolution observations, the 10s BC mass is scaled  
208 by the mass ratio between the 60 s R3 and the 60 s average R2 data sets. The scaled  
209 90 s average observations are compared directly with the nearest model grid cell so  
210 that the model values are not interpolated.”

211 The temporal (not spatial) averaging and nearest-neighbor approaches introduce some  
212 mismatch between the observation and adjoint forcing locations. Spatial interpolation  
213 would reduce that error somewhat. We have not tested the impact on the posterior,  
214 but at least the adjoint spatial dispersion should enforce some correction.

- 215 13. *Specific Comment: Page 15, line 18: The authors mention that their adjoint technique*  
216 *requires 600 more computational time than a single simulation. It is good that this*  
217 *is mentioned. What is not included how many man-months or man-years such an*  
218 *effort requires (and that does not need to be included). But I would like to see some*  
219 *discussion at the end of the paper to weigh in on the advantages and disadvantages of*  
220 *the additional computation cost. In other words, is it worth the effort?*

221 **AUTHOR RESPONSE:** An objective answer to this question would require an  
222 extensive meta analysis of the benefits and costs of adjoint-based 4D-Var compared to  
223 other approaches, and would need to examine the valuation of labor versus hardware .  
224 But hopefully the results of this work could contribute to such a study someday. Also,  
225 for clarification we note that a single adjoint simulation in WRFPLUS-Chem requires a  
226 wall-time that is approximately 7 times that of a single forward model simulation, not  
227 600 times. It is the optimization (4D-Var) that requires most of the extra resources.

- 228 14. *Specific Comment: Page 15, lines 22-26: In this section of the details of the adjoint*  
229 *technique, I found it difficult to understand why it is important to show the convergence*  
230 *properties. I found the answer a few lines down on line 26. This rationale is a bit*  
231 *buried. I found the other sections had similar problems in terms of why it was important*  
232 *to visit aspects of the adjoint technique. This is a reflection that the authors assume the*  
233 *audience has a detailed knowledge of data assimilation and the adjoint technique in*  
234 *particular. So I think the concepts could be better communicated to a larger audience.*

235 **AUTHOR RESPONSE:** This paragraph and the following one have been reor-  
236 ganized for clarity and accuracy. In particular, the topic sentence for the following  
237 paragraph was previously misleading for the text within. There was also a sentence  
238 about model uncertainty being higher in locations with higher prior concentrations.  
239 While that is true on average, it is not the dominant error behavior corresponding to  
240 8:00 LT and 8:30 LT on 22 June, where the difference in observation uncertainty is  
241 more evident due to the difference in observed concentration.

242 **Manuscript changes:** See p15, lines 2-23.

- 243 15. *Specific Comment: Page 16, line 12: In relation to “overprediction seems to be less of*  
244 *a problem” to me is a result of the coarse grid spacing. Using  $dx = 18 \text{ km}$ , the model*

245 *should underpredict the peak concentrations of the emissions are correct. Only when*  
246 *the grid spacing is finer will the model resolve details of the smoke plume and there will*  
247 *be periods in which the concentrations could be higher than observed.*

248 **AUTHOR RESPONSE:** While originally we thought that the observation smooth-  
249 ing should be enough to counteract this resolution problem, we now realize a mistake  
250 in that logic. We modify the text as described below.

251 **Manuscript changes:** We removed that sentence and added the following paragraph  
252 (p16, lines 1-9): “For the appreciable measured BC concentrations ( $> 0.25 \mu\text{g m}^{-3}$ ),  
253 that are likely caused by a source within the model domain and simulation period,  
254 the lack of a source-receptor relationship is likely caused by low resolution. Changing  
255 a point source to a grid-scale area source changes its effective location. Temporal  
256 averaging of the observations will not necessarily solve that problem since perfectly  
257 modeled transport could still send a mis-located source in an entirely different direction  
258 than the truthfully located source. This effect is evident for valley fires (Strand et al.,  
259 2012), since placing the sources in the basin or spreading them throughout the basin  
260 and the peaks will result in different “downwind” concentrations. Downwind might  
261 be a very different direction if the convective scale winds contribute more information  
262 than the mesoscale winds to the true source-receptor relationship. Since the emissions  
263 are smoothed in the model and not in reality, the mis-location is more likely to cause  
264 under-prediction than over-prediction.”

265 The coarse resolution offsets the location of the sources relative to the fire detections  
266 (Figure 2), and this would prevent the true sparse BB point sources from aligning  
267 with the model-observation residual error. However, the observed intensity of the true  
268 smoke plume is muted by the temporal averaging. The posterior model concentrations  
269 in Fig. 4 (top) mimic the temporal resolution of those observations. Thus, the model  
270 could achieve the same intensity as the observations with correct emission magnitudes  
271 and locations.

- 272 16. *Specific Comment: Page 16, line 35: A 3.8 factor of uncertainty is used for the emis-*  
273 *sions. Did the authors try using values larger than 3.8?*

274 **AUTHOR RESPONSE:** That value was not arbitrary (see p14, lines 17-23). We  
275 tried values up to a factor of 10 for biomass burning sources in FINN\_STD and  
276 QFD\_STD, but larger uncertainties tended to raise the value of the final cost func-  
277 tion. Since FINN V1.5 is an outlier in this location and at several others, it warrants  
278 a larger uncertainty.

- 279 17. *Specific Comment: Page 18, lines 3-11: The increases in BC emissions in the Fresno*  
280 *area are remarkable, so that it seems to have higher emissions than the LA area (at*  
281 *least from the scale in the figure). The explanation for missing BC emission seems*  
282 *plausible, but would missing railroad emission produce values as high as the entire LA*  
283 *basin? Does this seem realistic?*

284 **AUTHOR RESPONSE:** To make this statement less definitive, we have made the  
285 following modifications.

286 **Manuscript changes:** (1) p17, line 35 to p18, line 2: Modification; “it could be  
287 speculated that the prior is missing diesel rail sources of BC. Another possibility...”  
288 changed to “the inversion results may suggest that the prior is missing diesel rail sources  
289 of BC. However, for locations where the prior magnitude of BB and anthropogenic  
290 emissions are of similar magnitude, their posteriors are subject to projection from one  
291 sector to another. It is more likely ...”

- 292 18. *Specific Comment: Page 21, lines 17-18: Isn't the first phrase in this sentence an*  
293 *obvious one that does not require this study to point out?*

294 **AUTHOR RESPONSE:** What we found important to point out is that alterna-  
295 tive observing strategies are required to characterize emissions. This is not surprising  
296 since IMPROVE was designed specifically to characterize background concentrations.  
297 Showing that this tool can at least tease out that basic observing strategy is the first  
298 step toward using such methods to plan more elaborate ones.

299 **Manuscript changes:** p21, lines 17-19: Modification; “The sparse  $\rho$  map for SURF  
300 in Fig. 13, and the large spike near Fresno illustrate that while near-source surface  
301 measurements can be a powerful constraint, measurements of background concentra-  
302 tions provide relatively little constraints on characterizing CA anthropogenic emissions  
303 on 1-day time scales.”

- 304 19. *Specific Comment: Page 22, lines 9-15: I am not sure what to make with the conclusion*  
305 *in the last sentence. It is true that in the cases examined in this study the aircraft flight*  
306 *paths and surface data might be saying different things about sources (since they are*  
307 *likely decoupled from one another). On other days that might not be the case when the*  
308 *aircraft flies in the boundary layer and will be more similar to h surface measurements.*  
309 *The concluding sentence seems to contract the whole notion of using ARCTAS-CARB*  
310 *for their test of the adjoint technique. However, a large fraction of fires, as well as*  
311 *field campaign data to characterize fires are conducted over forest regions that are often*  
312 *located in areas of complex terrain. It seems to be a problem one has to confront.*

313 **AUTHOR RESPONSE:** We have revised and shortened this paragraph, removing  
314 several sentences. Cross validation is a potentially useful inversion verification tech-  
315 nique. While it did not turn out to be very valuable in this particular case, that alone  
316 doesn't negate the value of the 4D-Var inversion, which we diagnosed using other means  
317 (posterior uncertainty estimates, DOF, etc.).

318 **Manuscript changes:** p22, lines 8-10: “Aircraft and surface observations do not  
319 appear to be useful for cross-validation of each other over the short timescales and  
320 limited set of flights considered here. At least for this study period, when they are not  
321 collocated, each provides some unique information to the inversion.”

- 322 20. *Specific Comment: Page 22: line 27: The authors state upfront and here that the paper*  
323 *focused on emissions only and not other factors that can affect BC concentrations. In*  
324 *the future, will they extend the analysis to meteorology to reduce those factors as well?*

325 **AUTHOR RESPONSE:** For the results of any inversion to be meaningful, one has to  
326 consider the uncertainty introduced by imperfect meteorology. While we attempted to

327 do this by introducing an ensemble-based model variance in  $\mathbf{R}$ , that approach leaves  
328 errors in subgrid vertical mixing that can not be corrected. A more robust (and  
329 expensive) solution is to use an ensemble of data assimilations (EDA) and simultaneous  
330 DA for meteorological and chemical variables. That would be one logical next step for  
331 this work.

- 332 21. *Specific Comment: Conclusion: There are a few points I find missing or poorly artic-*  
333 *ulated. The first is related to recommendation on future sampling. Here and there in*  
334 *the paper the authors mention or allude to changes in the sapling strategy that would*  
335 *help in better constraining the emission. (1) It would be useful to include a summary*  
336 *of  $X$ ,  $Y$ , and  $Z$  they feel would be useful. (2) Second, how many more cases would be*  
337 *needed to have more robust estimates of the emissions? (3) Finally, another discussion*  
338 *I mentioned in an early comment, is the computational cost and effort of using an*  
339 *adjoint technique worth the cost? One could take an alternative approach is to simply*  
340 *perform a small number of sensitivity simulation that scale the emissions to get a better*  
341 *fit. This is of contrast to a brute force method, which is not as mathematically pleasing*  
342 *as the adjoint.*

343 **AUTHOR RESPONSE:** (1) We have revised the manuscript as described below.

344 **Manuscript changes:** p19, line 4: Removal; “Further decreasing uncertainty would  
345 require observing the same phenomena more thoroughly, either for longer periods, with  
346 greater spatial coverage, or with more instruments.”

347 p19, lines 24-27: Addition; “That strategy is consistent with what is generally known:  
348 further decreasing uncertainty requires observing the same phenomena more thor-  
349 oughly. For hourly to daily time scales, more observations are needed close to and  
350 downwind of chemical sources, and at high spatial and temporal resolution (e.g., from  
351 repeated aircraft overpasses, extra aircraft, hourly-average surface sites, satellites).”

352 Also, we again revisit the topic of the types of observations that would be most useful  
353 in the Conclusions:

354 “...high spatial and/or temporal resolution concentration measurements from research  
355 campaigns or geostationary satellites are necessary to provide the sufficient constraints  
356 on inventory errors.”

357 (2) 4D-Var does not provide this information – for that we would need the adjoint of  
358 the adjoint, and of the optimization routine itself. Clearly this goes beyond the scope  
359 of the present work.

360 (3) When comparing the computational and development costs of a Bayesian top-down  
361 method (e.g., adjoint-based 4D-Var, EnKF, or LPDM) to an ad-hoc scaling, one must  
362 consider the differences in the types of solutions that these methods provide. Indeed,  
363 a “small number of sensitivity simulations” can be used to derive low-dimension re-  
364 scalings of the emissions, as we demonstrated in Section 2.2. In contrast, a high  
365 resolution Bayesian posterior has much more spatial-temporal information than can  
366 be provided by a sensitivity study. Further, a Bayesian inversion’s goal goes beyond  
367 getting “a better fit”, which runs the risk of overfitting data that contains noise with-  
368 out regards for prior information or model errors; additionally, Bayesian approaches

369 afford posterior diagnostics regarding the reduction in uncertainty and information  
370 content. This auxiliary information, not available from a simple emissions rescaling  
371 based on low-dimension sensitivity calculations, is useful for evaluating the value of  
372 the observations and the inversion result.

- 373 22. *Specific Comment: Figure 2: The colors used for the vegetation distribution make it*  
374 *difficult to see the red dots denoting the fires. It would be useful to include the aircraft*  
375 *flight paths.*

376 **AUTHOR RESPONSE:** We added the 22 June flight transect, and also added white  
377 outlines to the fires to differentiate them from the surrounding colors.

378 **Manuscript changes:** Replaced Figure 2.

- 379 23. *Specific Comment: Figure 7: Consider changing the color scale, it is very difficult to*  
380 *see changes from one figure to the next.*

381 **AUTHOR RESPONSE:** We smeared out the color scale on the low end to make  
382 the large outliers stick out. Since the variation in neighboring grid cells can be quite  
383 large, it is difficult to pick out single grid cells. Also, with the difference in re-gridding  
384 between QFED and FINN, comparison between the two inventories is tenuous at grid  
385 scale. The posterior-prior increments in Figure 8 and the EA totals in Table 5 serve  
386 as other means of comparison.

- 387 24. *Specific Comment: Figure 9: The caption denotes posterior BB, but it is not clear*  
388 *which lines in the figure are posterior based on the legend.*

389 **Manuscript changes:** Modified caption; “Hourly BB diurnal emission patterns for  
390 the four EAs and all inversion scenarios for 22 June, 00Z-23Z, with the time shown in  
391 LT. The priors are shown as black lines, while the posteriors from specific inversion  
392 scenarios are shown in color. Note that FINNv1.0 did not have any fires in EA4 on 21  
393 June.”

## 394 2 Responses to Anonymous Referee #3

- 395 1. *Specific Comment: One major concern of the MS is that the numerical experiments*  
396 *were only based on two real case forecasting. Since the atmospheric chemistry and*  
397 *meteorological conditions vary day to day. It is suggested that the authors extend the*  
398 *experiments.*

399 **AUTHOR RESPONSE:** Indeed the cross validation was meant to check whether  
400 the posterior scaling factors found on one day are consistent with observations on  
401 subsequent days. They were not. We conclude that an observing strategy that targets  
402 specific source regions for longer periods of time would be more beneficial than, e.g.,  
403 trying to cover the entire state of California in a single campaign. Much of this work  
404 was geared towards seeing what exactly this new tool can accomplish with a given set  
405 of observations. In future work it will be applied to many other observation sets.

- 406 2. *Specific Comment: How many numbers of the control variables in your CHEMDA*  
407 *system? Only BC? Please clarify the observation Operator and its adjoint. If the*  
408 *control variable ?same? as observation, the observation Operator and adjoint is simply*  
409 *as interpolation method. If not, you should clarify in the manuscript. In addition,*  
410 *how to deal with cross correlation between control variables (e.g. NO<sub>3</sub> is correlate with*  
411 *SO<sub>4</sub>) if the number of CV is more than two.*

412 **AUTHOR RESPONSE:** The observation operator includes temporal averaging and  
413 a conversion from  $\mu\text{g BC m}^{-3}$  in the observation to  $\mu\text{g BC (kgdryair)}^{-1}$  in the model.  
414 We describe those details and those of the model adjoint derivation in Guerrette and  
415 Henze (2015). Although BC is the only chemical species for which emissions are con-  
416 strained, the sources are distributed across the entire domain. There are many zero-  
417 emission grid cells for BB sources. In total there are 5080 grid cells with non-zero  
418 emissions (# biomass burning + # anthropogenic), each with a scaling factor every  
419 hour (size(CV) = 121,920 for 24 hours) — i.e., p14, line 35.

- 420 3. *Specific Comment: Incremental method is commonly used method in data assimila-*  
421 *tion. The manuscript appear “incremental” many times. I suggest delete redundant*  
422 *“incremental” in the manuscript.*

423 **AUTHOR RESPONSE:** While we agree that needless repetition of an established  
424 term ought to be avoided, in most cases we specifically refer to the incremental formu-  
425 lation to distinguish it from other approaches that previous authors have followed or  
426 to make note of particular advantages or disadvantages of this method. Here is a list  
427 of places where we feel this is the case:

- 428 • p3, line 25
- 429 • p4, line 14
- 430 • p5, line 15
- 431 • p7, line 3
- 432 • p7, line 6
- 433 • p8, lines 28 and 30
- 434 • p12, line 26
- 435 • p13, line 1
- 436 • p22, line 12

437 **Manuscript changes:** Removed “incremental” at p14, line 33. Removed “4D-Var”  
438 at p22, line 19.

- 439 4. *Specific Comment: Background error covariance (BEC) is important in data assimila-*  
440 *tion. The observation information spread to model grid cells via BEC. The authors*  
441 *mentioned chemical emissions heterogeneous. However, the construction of the “B” in*  
442 *the manuscript seems to be homogeneous?*

443 **AUTHOR RESPONSE:** Yes the chemical emissions are heterogenous. We use mul-  
444 tiplicative uncertainties through a log-normal background term to circumvent the need

445 to use heterogenous Gaussian distributed errors. We also discussed the possibility that  
446 the relative uncertainties are spatially heterogeneous. One might derive such heteroge-  
447 nous uncertainties using a Monte Carlo approach, but the details of such a procedure  
448 are far beyond the scope of this work.

### 449 **3 Additional changes**

- 450 1. We modified the Damped Gauss Newton section to remove needless details. Since  
451 writing the paper, we have added an optimal line search for the damping parameter,  
452 and the new results are nearly identical to those presented in this work. Thus we also  
453 eliminated the discussion of “Heuristic Damped Gauss Newton”.
- 454 2. Modification; the posterior covariance is changed from  $\mathbf{A}$  to  $\mathbf{P}^a$  throughout for consis-  
455 tency with previous literature.
- 456 3. We rearranged the second paragraph (p2, lines 7-13) to improve readability.
- 457 4. “heterogenous” is corrected to “heterogeneous” throughout
- 458 5. p4, line 8: Modification; “incremental 4D-Var in WRFDA-Chem” changed to “WRFDA”
- 459 6. p5, line 34 to p6, line 2: Modification; “For temperate forests QFED scales aerosols by  
460  $\times 4.5$  throughout the world. That vegetation category accounts for 80% of the wild-fire  
461 BC in California during 22-30 June 2008. The ...”
- 462 7. p6, lines 5-6: Addition; ”..., and without it FINNv1.0 and QFED would differ by  $\times 10$   
463 during the ARCTAS-CARB campaign.”
- 464 8. p14, line 19; p14, line 24; p16, line 21: Addition; “relative” as in “..we use a relative  
465 grid-scale BB uncertainty..”
- 466 9. p14, line 23: Addition; “(see Sec. 3.3)”
- 467 10. p16, line 27: Modification; changed “in” to “at” as in “Meanwhile, at other times...”
- 468 11. p17, line 24: Reference Correction; “Zhang et al., 2012” fixed to “Zhang et al., 2014a”
- 469 12. p18, line 15: Removal; “and ” as in “..., and additional inversions, ”
- 470 13. p21, line 23: Removal; “Even before carrying out such a test, ” as in “Even before  
471 carrying out such a test, the heterogeneous adjoint ...”
- 472 14. p22, line 4: Modification; “in any” changed to “derived from”
- 473 15. p22, line 27: Added reference to Song et al. (2016).



# Four dimensional variational inversion of black carbon emissions during ~~ARCTAS-CARB~~ ARCTAS-CARB with WRFDA-Chem

J. J. Guerrette<sup>1</sup> and D. K. Henze<sup>1</sup>

<sup>1</sup>Department of Mechanical Engineering, University of Colorado, Boulder, CO, 80309, U.S.A.

*Correspondence to:* Jonathan Guerrette (jonathan.guerrette@colorado.edu)

**Abstract.** Biomass burning emissions of atmospheric aerosols, including black carbon, are growing due to increased global drought, and comprise a large source of uncertainty in regional climate and air quality studies. We develop and apply new incremental 4D-Var capabilities in WRFDA-Chem to find optimal spatially and temporally distributed biomass burning (BB) and anthropogenic black carbon (BC) aerosol emissions. The constraints are provided by aircraft BC concentrations from the Arctic Research of the Composition of the Troposphere from Aircraft and Satellites in collaboration with the California Air Resources Board (ARCTAS-CARB) field campaign and surface BC concentrations from the Interagency Monitoring of PROtected Visual Environment (IMPROVE) network on 22, 23, and 24 June, 2008. We consider ~~multiple~~ three BB inventories, including Fire INventory from NCAR (FINN) v1.0 and v1.5 and Quick Fire Emissions Database (QFED) v2.4r8. On 22 June, aircraft observations are able to reduce the spread between ~~QFED~~  $\times \frac{1}{3}$  a customized QFED inventory and FINNv1.0 from a factor of 3.5 ( ~~$\times 3.5$  to~~) to only  $\times 2.1$ . On 23 and 24 June, the spread is reduced from  $\times 3.4$  to  $\times 1.4$ . The posterior corrections to emissions are ~~heterogenous~~ heterogeneous in time and space, and exhibit similar spatial patterns of sign for both inventories. The posterior diurnal BB patterns indicate that multiple daily emission peaks might be warranted in specific regions of California. The U.S. EPA's 2005 National Emissions Inventory (NEI05) is used as the anthropogenic prior. On 23 and 24 June, the coastal California posterior is ~~sealed by~~  $\times \frac{1}{2}$  reduced by  $\times 2$ , where highway sources dominate, while inland sources are increased near Barstow by  ~~$\times 5$~~   $\times 5$ . Relative BB emission variances are reduced from the prior by up to 35% in grid cells close to aircraft flight paths and up to 60% for fires near surface measurements. Anthropogenic variance reduction is as high as 40% and is similarly limited to sources close to observations. We find that the 22 June aircraft observations are able to constrain approximately 14 degrees of freedom of signal (DOF), while surface and aircraft observations together on 23/24 June constrain 23 DOF. Improving hourly to daily scale concentration predictions of BC and other aerosols during BB events will require more comprehensive and/or targeted measurements and a more complete accounting of sources of error besides the emissions.

## 1 Introduction

Black carbon (BC) makes significant contributions to short term climate (Bond et al., 2013) and human health (Janssen et al., 2012) as a component of aerosolized fine particulate matter (PM<sub>2.5</sub>) in the atmosphere. BC is emitted through incomplete combustion from natural and anthropogenic burning of biomass and fossil fuels. Open biomass burning (BB), which includes

natural wild fires, deforestation, and agricultural waste and prescribed burning, accounts for 40% of total global BC emissions, while anthropogenic energy related sources (e.g., on- and off-road diesel and gasoline engines, industrial coal, residential cooking and heating) make up the remaining 60% (Bond et al., 2013). Future climate conditions that increase drought and fire prevalence (e.g., Spracklen et al., 2009) and increasingly regulated anthropogenic sources might lead to a reversal of these ratios in California (Mao et al., 2011) and globally (Jolly et al., 2015). In California, BB events have been shown to increase surface PM<sub>2.5</sub> concentrations by a factor of 3 to 5 ( $\times 3$  to  $\times 5$ ), compared to non-fire periods (Wu et al., 2006). The heterogeneity in BC emission and loss patterns and difficulty in replicating transport contribute to prediction uncertainty.

Despite the recognized importance of biomass emissions, large discrepancies remain in inventories in terms of biomass consumed and emitted chemical species. ~~Zhang et al. (2014a) considered seven~~ Fu et al. (2012) considered two different inventories during ~~February 2010 over Africa, which gave a range of  $\times 12$  in January and April 2006 over Southeast and East Asia, where the~~ total emitted OC and BC throughout the month. ~~Fu et al. (2012) differed by  $\times 12$ .~~ Zhang et al. (2014a) found similar variability between only two inventories in Southeast and East Asia during January and April 2006. seven inventories in Africa during February 2010. Zhang et al. (2014a) concluded that diffusion and loss mechanisms limit the ~~effect of the monthly emission variability to only a  $\times 2-3$  range of monthly average~~ corresponding responses of domain-wide aerosol burden, AOD, and 2 m temperature to  $\times 2-3$ . However, the inventory spread ~~of emission magnitudes from larger sources led to column burden ranges for larger source magnitudes led to modeled column burden spreads~~ of  $\times 16-30$  at ~~the~~ hourly to daily grid scales.

The large range in inventories at small fine scales results from the differing ways in which they are built. In order to be globally applicable, fire locating algorithms use remotely sensed hot spots from polar-orbiting satellites. Some provide additional regional locational and diurnal information with geostationary instruments. In all cases, daily emissions in a grid cell are calculated as the product of activity (kg burned) and emission factors for each species and vegetation class combination (kg emitted (kg burned)<sup>-1</sup>). Bottom-up inventories combine rough estimates of burned area with vegetation densities and percent biomass burned associated with different Land Cover Types (LCT) to determine fire activity (e.g., Wiedinmyer et al., 2011; Reid et al., 2009; van der Werf et al., 2010). Top-down approaches use fire radiative power (FRP) measured by polar-orbiting or geostationary satellites and the LCT-specific energy content (e.g., Kaiser et al., 2012; Zhang et al., 2012), which circumvents using uncertain estimates of burned areas (Boschetti et al., 2004). A third approach combines the FRP with top-down constraints of aerosol optical depth (AOD) (e.g., Ichoku et al., 2012; Darmenov and da Silva, 2013). All three of these approaches cross reference fire locations with biome lookup tables to obtain the species-specific emission factors for each fire.

Improving short-term, local BC concentration predictions requires characterizing fine-scale spatial and diurnal patterns of BB emissions. The weakness of using only polar-orbiting data (e.g., Moderate Resolution Imaging Spectroradiometer (MODIS) instruments aboard Terra and Aqua) in bottom-up fire inventories is that there are nominally four overpasses per day, often with missed detections due to cloud- and smoke-cover or fire sizes beyond the instrument detection limits. Thus, these observations provide little information about the diurnal pattern of fire counts and FRP. Zhang et al. (2012) and Andela et al. (2015) devise methods for deriving climatological diurnal FRP patterns using geostationary observations. Both provide new information to modelers, but the former is not generalizable to grid-scale diurnal variability and the latter precludes the possibility that diurnal

FRP (Zhang et al., 2012) and emissions (Saide et al., 2015) patterns may be bimodal for specific LCT's and fire regimes, or due to local meteorology.

In contrast to their BB counterparts, anthropogenic emissions of BC are periodic across weekly and annual time scales. Their spatial distributions are relatively well-known in developed countries, and less so in developing countries (Bond et al., 2013).  
5 Global estimates of annual anthropogenic BC emissions vary by  $\times 2$  (Bond et al., 2013), national annual BC emissions in Asian countries and regions have uncertainties from  $\times 2$  to  $\times 5$  (Streets et al., 2003). In North America, including in California, uncertainties still persist in terms of characterizing the magnitude of emissions in a particular year, seasonal variability, and long term trends in activity and control strategies (Grieshop et al., 2006; McDonald et al., 2015). Bond et al. (2013) cite several inventories ~~that give a range of  $\times 1.7$  for of~~ annual U.S. ~~anthropogenic BC emissions~~non-BB BC sources, which are  
10 between 260 to 440 Ggyr<sup>-1</sup>, yielding a maximum to minimum ratio of 1.7. However, like many other inventories, the U.S. EPA National Emission Inventory (Reff et al., 2009) does not specify uncertainty bounds either for the whole country or at state and county levels.

These challenges in characterization of both BB and anthropogenic emissions of BC and co-emitted species have led to the proliferation of top-down constraint methods of varying complexity and utility. Several studies have used adjoint-free methods  
15 for anthropogenic emissions in Los Angeles, California using aircraft measurements during the 2010 California Research at the Nexus of Air Quality and Climate Change (CalNex) campaign. Brioude et al. (2012) constrained CO, NO<sub>x</sub>, and CO<sub>2</sub>, and Cui et al. (2015) constrained CH<sub>4</sub>; both applied a Lagrangian Particle Dispersion Model (LPDM). Peischl et al. (2013) constrained CH<sub>4</sub> using a mass balance approach and light alkane signatures from multiple sectors. LPDM benefits from being able to resolve sources on as fine of a grid resolution as is used in the underlying model. Both LPDM and mass balance are limited  
20 to linear tracer problems where observations are recorded under specific meteorological conditions. Wecht et al. (2014) used GEOS-Chem in an analytical inversion to compare constraints from the CalNex aircraft measurements with those from present and future satellite observations of CH<sub>4</sub> throughout California. Although an analytical inversion does not require an adjoint, the approach is limited, computationally, to constraining only a few sources, which imposes aggregation error (Mao et al., 2015). Adjoint-based four-dimensional variational data assimilation (4D-Var) is able to account for nonlinear behavior between the  
25 emission sources and observation receptors by calculating exact gradients across physical processes. Such an approach does not have the limitations imposed by mass balance, LPDM, or analytical inversions, but does require development of an adjoint. The gradients are usually calculated through an adjoint model, although recent work (Saide et al., 2015) performs 4D-Var on a limited area fire without an adjoint. That new approach, while easier to implement, is limited to solving for only a few spatially-distributed sources due to computational limitations.

In this study, we adapt the adjoint-based incremental ~~four dimensional variational data assimilation (incremental 4D-Var )~~  
30 used in the WRFDA weather forecasting system (Barker et al., 2005; Huang et al., 2009) to solution of tracer surface flux estimation problems. The modifications to that system that are required for this work are described in Sec. 2 as well as in Guerrette and Henze (2015) (GH15). These include new linearized model descriptions (GH15), memory and I/O trajectory management (GH15), a log-normal emission control variable (Sec. 2.3.2), calculation of posterior variance (Sec. 2.3.4), and  
35 improvements to the Gauss-Newton optimization algorithm to handle nonlinearities (Sec. 2.3.5). As described in GH15, this

approach of assimilating chemical tracer observations in a regional numerical weather prediction and chemistry model is unique in the context of previous 4D-Var flux constraints.

We apply the resulting tool, WRFDA-Chem, to constrain anthropogenic and BB sources of BC throughout California during the Arctic Research of the Composition of the Troposphere from Aircraft and Satellites in collaboration with the California Air Resources Board (ARCTAS-CARB) field campaign. In June 2008, ARCTAS-CARB characterized aerosols and trace gases throughout California with DC-8 aircraft flights on 20 (Friday), 22 (Sunday), 24 (Tuesday), and 26 (Wednesday) June (Jacob et al., 2010). Sahu et al. (2012) used BC total mass measurements from a single-particle soot photometer (SP2) and other simultaneous gas-phase measurements to identify and characterize anthropogenic and BB plumes in California. ~~We assess the capability of these same~~ By using these observations and every-3<sup>rd</sup>-day surface measurements from the Interagency Monitoring of PROtected Visual Environment (IMPROVE) network ~~to constrain errors in,~~ we provide top-down estimates of BC surface fluxes ~~when used in using~~ 4D-Var. ~~As described in (Guerrette and Henze, 2015), this approach of assimilating chemical tracer observations in a regional numerical weather prediction and chemistry model is unique in the context of previous 4D-Var flux constraints. We also estimate emissions, their associated uncertainties, and provide diagnostics for observing system evaluation at high spatio-temporal resolution (hourly, 18 × 18).~~ The mixture of anthropogenic and BB sources distributed across complex terrain and biomes is a difficult system to characterize. Still, this scenario is typical of daily smoke exposure forecasting during acute wild fire events, and is a relevant first test case for the new 4D-Var system.

The approach taken in this work is described in Sec. 2, including the forward, adjoint, and tangent linear models, the prior inventories and domain, and the ~~incremental 4D-Var method implemented in WRFDA-Chem~~ adaptation of WRFDA. Section 3 describes the application of WRFDA-Chem to the BB and anthropogenic emission inversion problem during ARCTAS-CARB. We conclude with a summary and recommendations for future ~~measurement campaigns~~ measurements and emission inversion research.

## 2 Method

### 2.1 Nonlinear, adjoint, and tangent linear models

Incremental 4D-Var requires forward nonlinear (NLM), adjoint (ADM), and tangent linear (TLM) models. The NLM is nearly identical to WRF-Chem (Grell et al., 2005) with the addition of emission scaling factors. The GOCART option facilitates 19 species, including 4 gas and aerosol species for sulfate chemistry, hydrophobic and hydrophilic BC and organic carbon, 5 size bins for dust, 4 bins for sea salt, and 2 diagnostic species for PM<sub>2.5</sub> and PM<sub>10</sub>. While we use GOCART, the results presented are limited to BC. The model configuration is the same as was used in Guerrette and Henze (2015), and is summarized as follows: ACM2 PBL mixing (Pleim, 2007a, b), Pleim-Xiu land surface model (Xiu and Pleim, 2001; Pleim and Xiu, 2003; Pleim and Gilliam, 2009) and surface layer (Pleim, 2006) mechanisms without soil moisture and temperature nudging, Wesely dry deposition velocities (Wesely, 1989), GSFC shortwave and Goddard long wave radiation, and microphysics turned off. Microphysical and radiative responses to online aerosols are ~~also turned off, because they are not included in WRF-Chem for GOCART~~ not taken into account for GOCART aerosols in WRF-Chem.

We utilize the recently developed WRFPLUS-Chem (Guerrette and Henze, 2015), which contains ADM and TLM code extending the original WRFPLUS software (Zhang et al., 2013). WRFPLUS-Chem describes chemical tracers in the context of planetary boundary layer (PBL) mixing, emissions, dry deposition, and GOCART aerosols. ADM and TLM gradients have been verified against finite difference approximations. Second-order checkpointing reduces the memory footprint to a feasible level for ADM and TLM simulations over longer durations ( $>\sim 6$  hr) and/or that use many chemical tracers ( $>\sim 10$ ). Guerrette and Henze (2015) applied the ADM in calculating sensitivities relevant to the emission inversion carried out here. Sec. 3.5 includes a comparison of the results of that study with the posterior emissions here.

The model domain is similar to that used by Guerrette and Henze (2015). The spatial extent encompasses California and other southwest U.S. states. We conduct two emission inversions, the first on 22 June with a focus on biomass burning sources, and the second on 23-24 June with a focus on anthropogenic sources. We generated chemical initial conditions by running WRF-Chem from 15 June 2008, 00:00:00 up until the beginning of each inversion period. We used the default WRF-Chem boundary condition for BC concentration of  $0.02 \mu\text{g kg}^{-1}$ , which was found to be consistent with observations with an upwind flight on 22 June. Meteorological initial and boundary conditions are interpolated from 3 h, 32 km North American Regional Reanalysis (NARR) fields. The horizontal resolution is 18 km throughout  $80\times 80$  columns, and there are 42 vertical levels between the surface and model top at 100 hPa.

Our horizontal grid spacing was chosen to balance the wall-time and memory requirements of 4D-Var with model accuracy, and the ACM2 PBL option was chosen to reduce ADM and TLM development efforts. Angevine et al. (2012) recommend that the complex terrain in California demands fine tuning of the WRF horizontal grid spacing, PBL, LSM, and reanalysis initialization. Among other conclusions, those authors found that at six surface sites near the land-ocean boundary a 4 km and a 12 km simulation with similar settings had mean wind speed biases of  $(0.15$  to  $1.5) \text{ m s}^{-1}$  and  $(-0.38$  to  $1.9) \text{ m s}^{-1}$ , respectively. Supporting that conclusion, Strand et al. (2012) used a 36 km resolution chemical transport model (CTM), with offline meteorology, and found significant negative mean fractional bias (MFB) in modeled  $\text{PM}_{2.5}$  relative to surface observations of fires within narrow Northern California valleys in July 2008 (MFB= $-34.95\%$ ) and during autumn 2007 Santa Ana winds (MFB= $-110.22\%$ ). During the July 2008 episode, their CTM predictions had a smaller positive bias (MFB= $+21.88\%$ ). Therefore, we would expect similar wind and concentration biases at 18 km resolution, which may or may not be improved by online meteorology. Incremental 4D-Var provides an opportunity to utilize a different model configuration (e.g., resolution) for the NLM comparisons of model to observations than that used for the ADM and TLM simulations. The adaptation of that capability from meteorological (i.e., Zhang et al., 2014b) to chemical simulations and the subsequent testing is reserved for future WRFDA-Chem developments.

## 2.2 Prior emission inventories

The prior includes sources of BC from anthropogenic activity and natural wild fires. Anthropogenic emissions are taken from the U.S. EPA's 2005 National Emissions Inventory (NEI05) for mobile and point sources, including for example diesel on-road and power production from coal. The individual sectors are lumped together for each grid cell. We represent BB emissions using three different wild fire inventories, FINNV1.0 and v1.5 both at  $1 \text{ km} \times 1 \text{ km}$  resolution (Wiedinmyer et al., 2011,

2006), and QFEDv2.4r8 at  $0.1^\circ \times 0.1^\circ$  resolution (Darmenov and da Silva, 2013). FINNv1.5 is readily available through NCAR (<http://bai.acom.ucar.edu/Data/fire/>) to WRF-Chem users, while FINNv1.0 is no longer supported. However, we include FINNv1.0 in this study, because it shows equivalent value as a prior. FINN and QFED fall into the first (bottom-up) and third (top-down constraint with AOD) category of BB inventories described in Sec. 1, respectively.

5 Any inverse modeling study that depends on an initial guess should start in a region of high probability. In a Bayesian inversion, the first guess should be unbiased. Here we address several known errors in our prior inventories that we either fix or are unable to fix. All changes are consistent with either observations or the intended physical descriptions of the inventories.

QFED scales global aerosol emissions from four biome types through multiple linear regression between observed MODIS aerosol optical depth (AOD) and modeled GEOS-5 AOD during the years 2004-2009. For temperate forests ~~-, which produce~~  
10 ~~80% of the wild-fire BC in California during this modeling study (June 2008),~~ QFED scales aerosols by  $\times 4.5$  throughout the world. ~~This~~ That vegetation category accounts for 80% of the wild-fire BC in California during 22-30 June 2008. The global scaling is problematic for the California fires, because the GEOS-5 AOD is biased high in the Western U.S. during the summer fire seasons of 2006-2008 (Fig. C14 of Darmenov and da Silva, 2013). In order to match the regional climatological AOD scaling factors for the Western U.S., we scale all QFED BC sources by  $\times \frac{1}{3}$ . This scaling is already taken into account in  
15 the prior emissions shown in Sec. 3.3, and without it FINNv1.0 and QFED would differ by  $\times 10$  during the ARCTAS-CARB campaign.

The WRF preprocessor distributed with the FINN inventory is used to distribute ASCII formatted lists of both FINN and QFED daily speciated fire emissions to hourly netcdf files readable by WRF. The diurnal profile follows the Western Regional Air Partnership profile WRAP (2005), and is defined by a flux peak from 13:00 to 14:00 Local Time (LT), and flat fluxes equal  
20 to 2.5% of the peak value between 19:00 LT and 09:00 LT. Through modeling experience, we found two bugs with how the FINN preprocessor interprets the WRAP profile and have fixed them for this case study. The total FINNv1.0 emissions across the model domain before and after fixing these bugs are plotted in Fig. 1 along with MODIS active fire counts (?). The first bug relates to how the timezone of a particular fire is calculated from longitude. The preprocessor converts a decimal longitude to integer time zone bins; this allows a fire at  $120.1^\circ\text{W}$  to be an hour earlier in the diurnal profile than a fire at  $119.9^\circ\text{W}$ ,  
25 even though they should be at nearly identical positions in the WRAP profile. Such behavior might apply to anthropogenic emissions, where cities near time zone borders follow different daily cycles of activity, but not to natural activity related to the  $15^\circ$  per hour cycle of the sun.

The second bug, and the one most visible in Fig. 1, is in the redistribution of UTC fire detections in to LT emissions. MODIS Terra and Aqua overpass times are distributed around noon and midnight LT globally, with some adjustment as the image  
30 capture location moves farther from the equator. The fire hot spots are detected in UTC days, and their emissions are profiled according to LT periods corresponding to the same UTC day as the detection. In California, where the LT is UTC minus 8 hours, the noon overpass corresponds to 20:00 UTC, and 00:00 UTC corresponds to 16:00 LT on the previous day (sun cycle). Therefore, when a fire is detected during nearly peak heat and emission fluxes at noon, a large fraction of the flux is apportioned to the previous afternoon. For locations east of the International Date Line, the LT reallocation is in the opposite direction. In  
35 either case, some portion of the profile is shifted by 24 hours. This error is apparent as a temporal discontinuity in the case

of transient fires that vary significantly in magnitude from one day to the next, especially after a recent ignition. Since the domain used here is nearly confined to a single time zone, we simply move the emissions forward one day for times between 16:00-23:00 LT (00:00-07:00 UTC). A more robust fix will need to be implemented in a future preprocessor.

Another error in the prior BB emissions is less easily resolved. Figure 2 shows where the MODIS active fires are located relative to the inventory fire locations. Since QFED fires are provided on a LAT-LON grid, the fire centers do not coincide with its grid centers. When the inventory is distributed to the 18 km model grid, some emissions are shifted over by one column relative to the FINN locations. There are several additional spurious emission locations in QFED, where no active fires were detected on either 21 or 22 June. In a month-long simulation, differences in fire gridding between several inventories can be averaged out. In the shorter term inversions over California presented in Sec. 3, the locational differences do affect the results.

## 10 2.3 WRFDA-Chem inversion system

### 2.3.1 Incremental 4D-Var

The aim of data assimilation (DA) is to optimally combine uncertain observations with uncertain model predictions to provide an improved estimate of the state of a system than either gives alone. ~~In Bayesian statistics, the probability distribution of a set of control variables~~ Here we apply incremental 4D-Var as first introduced by Courtier et al. (1994), utilizing the existing software architecture in WRFDA, and extended to accommodate positive definite emissions with large associated uncertainties (Sec. 2.3.2). In Appendix A, we show (similar to Lawless et al. (2005); Gratton et al. (2007); Tshimanga et al. (2008)) that incremental 4D-Var is equivalent to a Gauss-Newton (GN) optimization, where a cost function,

$$\begin{aligned}
 \min_{\delta \mathbf{x}^k} J(\delta \mathbf{x}^k) &= \frac{1}{2} [\delta \mathbf{x}^k + (\mathbf{x}^{k-1} - \mathbf{x}_b)]^\top \mathbf{B}^{-1} \\
 &\quad \sim [\delta \mathbf{x}^k + (\mathbf{x}^{k-1} - \mathbf{x}_b)] \\
 &\quad + \frac{1}{2} (\mathbf{G}^{k-1} \delta \mathbf{x}^k - \mathbf{d}^{o,k-1})^\top \mathbf{R}^{-1} \\
 &\quad \sim (\mathbf{G}^{k-1} \delta \mathbf{x}^k - \mathbf{d}^{o,k-1}),
 \end{aligned} \tag{1}$$

is linearized around a current guess of a control variable vector (CV),  $\mathbf{x} \in \mathcal{R}^n$ , conditional on available observations,  $\mathbf{y}^o$ , is proportional to the product of two known distributions,

$$\underline{P(\mathbf{x}|\mathbf{y}^o)} \propto P(\mathbf{x}) P(\mathbf{y}^o|\mathbf{x}).$$

The first distribution on the right hand side is called the prior, background, or first guess; the second is the likelihood of model-observation mismatch, where here both are assumed to be Gaussian. They are found through the solution of the



minimization problem-

$$\min_{\mathbf{x}} J(\mathbf{x}) = \frac{1}{2}(\mathbf{x} - \mathbf{x}_b)^\top \mathbf{B}^{-1}(\mathbf{x} - \mathbf{x}_b) + \frac{1}{2}(G(\mathbf{x}) - \mathbf{y}^o)^\top \mathbf{R}^{-1}(G(\mathbf{x}) - \mathbf{y}^o),$$

where  $\mathbf{x}_b \in \mathbb{R}^n$ , minimized, then relinearized, and so on.  $\delta \mathbf{x}^k$  is the CV perturbation sought in the  $k^{\text{th}}$  linearization.  $\mathbf{x}_b$  is the vector of prior CVs,  $\mathbf{B}$  is the background covariance matrix, and  $\mathbf{R}$  is the model-observation error covariance matrix. The

5 nonlinear operator,

$$G(\mathbf{x}) = \begin{pmatrix} H_1(\mathbf{x}) \\ \vdots \\ H_i(\mathbf{x}) \\ \vdots \\ H_N(\mathbf{x}) \end{pmatrix}, \quad (2)$$

is similar to that applied by Weaver et al. (2005) and Tshimanga et al. (2008), and is composed of the model-observation operators, with each  $H_i$  mapping  $\mathbf{x}$  to observation time  $i$ . The measurements at each acquisition time,  $y_i^o \in \mathcal{R}^{m_i}$ ,  $y_i^o \in \mathbb{R}^{m_i}$ , are expressed independently for  $N$  acquisition times by

$$10 \quad \mathbf{y}^o = [\mathbf{y}_1^{o\top}, \dots, \mathbf{y}_N^{o\top}]^\top \in \mathbb{R}^m, \quad (3)$$

where  $\sum_{i=1}^N m_i = m$ . The  $o$  superscript denotes that  $\mathbf{y}^o$  are observations.  $\mathbf{d}^{o,k-1}$  is the innovation between observations and model values in the previous linearization:

$$\mathbf{d}^{o,k-1} = \mathbf{y}^o - G(\mathbf{x}^{k-1}). \quad (4)$$

The linearized cost function is derived under the assumption that

$$15 \quad G(\mathbf{x}^k + \delta \mathbf{x}) \approx G(\mathbf{x}) + \mathbf{G}^{k-1} \delta \mathbf{x}, \quad (5)$$

where  $\mathbf{G} \in \mathbb{R}^{n \times m}$  is the Jacobian of  $G$ . The superscript on  $\mathbf{G}^{k-1}$  denotes that it is linearized around the state from the previous iteration, i.e.,

$$\mathbf{G}^{k-1} = \begin{pmatrix} \mathbf{H}_1|_{\mathbf{x}^{k-1}} \\ \vdots \\ \mathbf{H}_i|_{\mathbf{x}^{k-1}} \\ \vdots \\ \mathbf{H}_N|_{\mathbf{x}^{k-1}} \end{pmatrix}. \quad (6)$$



The In an emission inversion for a single chemical species,  $n = n_x n_y n_t = O(10^5 - 10^6)$ , depending on the domain size and temporal aggregation of posterior emissions. Since the number of members in  $\mathbf{B}$  is equal to  $n^2$ , finding its inverse is computationally infeasible. To circumvent that challenge, Barker et al. (2004) implemented the control variable transform (CVT) through a square root preconditioner (Lorenc, 1988),  $\mathbf{U}$ , in WRFDA. The increment is transformed as  $\delta \mathbf{x}^k = \mathbf{U} \delta \mathbf{v}^k$ ,

5 where  $\mathbf{B} = \mathbf{U}\mathbf{U}^\top$ ,  $\mathbf{U}^\top \mathbf{B}^{-1} \mathbf{U} = \mathbf{I}_n$ , and  $\mathbf{I}_n \in \mathbb{R}^{n \times n}$  is the identity matrix. The transformed minimization problem is

$$\begin{aligned} \min_{\delta \mathbf{v}^k} J(\delta \mathbf{v}^k) &= \frac{1}{2} (\delta \mathbf{v}^k - \mathbf{d}^{b,k-1})^\top (\delta \mathbf{v}^k - \mathbf{d}^{b,k-1}) \\ &\quad + \frac{1}{2} (\mathbf{G}^{k-1} \mathbf{U} \delta \mathbf{v}^k - \mathbf{d}^{o,k-1})^\top \mathbf{R}^{-1} \\ &\quad \quad (\mathbf{G}^{k-1} \mathbf{U} \delta \mathbf{v}^k - \mathbf{d}^{o,k-1}), \end{aligned} \quad (7)$$

where the background departure, summed over all previous outer iterations, is

$$\mathbf{d}^{b,k-1} = - \sum_{k_o=1}^{k-1} \delta \mathbf{v}^{k_o}. \quad (8)$$

In addition to circumventing calculating  $\mathbf{B}^{-1}$ , the preconditioner reduces the condition number of the problem, speeding up the minimization process.

The solution to Eq. 1 is found by setting its gradient equal to zero, i.e.,

$$\begin{aligned} \nabla_{\delta \mathbf{v}} J &= (\delta \mathbf{v}^k - \mathbf{d}^{b,k-1}) \\ &\quad + \mathbf{U}^\top \mathbf{G}^{k-1 \top} \mathbf{R}^{-1} (\mathbf{G}^{k-1} \mathbf{U} \delta \mathbf{v}^k - \mathbf{d}^{o,k-1}) \\ &= \mathbf{0}. \end{aligned} \quad (9)$$

This yields to solution to the  $k^{\text{th}}$  linearization:

$$\begin{aligned} \delta \mathbf{v}^k &= \left( \mathbf{I}_n + \mathbf{U}^\top \mathbf{G}^{k-1 \top} \mathbf{R}^{-1} \mathbf{G}^{k-1} \mathbf{U} \right)^{-1} \left( \mathbf{d}^{b,k-1} + \mathbf{U}^\top \mathbf{G}^{k-1 \top} \mathbf{R}^{-1} \mathbf{d}^{o,k-1} \right) \\ &= - [\mathcal{H}_{\delta \mathbf{v}}]^{-1} \nabla_{\delta \mathbf{v}} J|_{\delta \mathbf{v}^k = \mathbf{0}}, \end{aligned} \quad (10)$$

15 where  $\mathcal{H}_{\delta \mathbf{v}} = \nabla_{\delta \mathbf{v}}^2 J$  is the Hessian of Eq. 7. In addition to their large size,  $\mathbf{G}$  and  $\mathbf{G}^\top$  are not often known explicitly and can only be multiplied by vectors through the integration of a TLM or ADM, respectively. As a result,  $\mathcal{H}_{\delta \mathbf{v}}$  and its inverse are too large to store and calculate explicitly. The inverse Hessian is generally approximated through an iterative minimization (e.g., conjugate gradient), called the inner loop, while the successive relinearizations are performed across outer loop iterations. Finite precision and the problem dimension,  $n$ , prevent Eq. 9 from being exactly equal to zero. Increasing the number of  
20 inner loop iterations to approach such an objective does not necessarily speed up convergence for the full nonlinear problem. Large innovations,  $\mathbf{d}^{o,k}$ , may remain after relinearization around the new state,  $\mathbf{x}^k = \mathbf{x}^{k-1} + \mathbf{U} \delta \mathbf{v}^k$ . The balance between computational expense and accuracy is chosen for each application.

### 2.3.2 Log-normal Control Variables

The positive definite nature of atmospheric chemical emissions combined with uncertainties that are potentially greater than 100% sets them apart from most CVs sought in meteorological data assimilation. The cost function in Eq. ?? is derived for 1 is derived assuming unbiased Gaussian statistics in both the background errors and model-observation errors. When grid-scale CV uncertainties are greater than 100%, as is often the case for chemical emissions, that assumption allows the posterior to be either positive or negative. While net surface flux rates can be negative when accounting for upward and downward rates together, emission rates are themselves positive. To ensure this, Emissions are more likely to be log-normally distributed, since individual sources are found from the products of variables which themselves are also positive definite. In order to ensure positive definiteness the ratio of modeled (posterior,  $E_a$ ) to tabulated inventory (prior,  $E_b$ ) emissions in all grid cells are gathered into a vector,  $\beta = e^{x_a}$ , such that

$$E_{a,j} = E_{b,j}\beta_j, \quad (11)$$

for CV member  $j$ . Each  $\beta_j$  is a “linear scaling factor, while”, while “exponential scaling factors” comprise the posterior CV vector,  $x_a$ . Fletcher and Zupanski (2007) showed that this approach — which was previously utilized in emission inversions by, e. g., Müller and Stavrakou (2005), Elbern et al. (2007), and Henze et al. (2009) — converges toward the median of a multivariate log-normal distribution for  $\beta$ . In this framework,  $x_b$  is the background exponential scaling factor. Setting  $x_b = 0$  is equivalent to assuming that the inventory emissions are the prior. Equation 11 is expressed within the  $G$  operator and its Jacobian.  $x$  is resolved on the grid scale and across hourly discretized emission rates; the temporal resolution is customizable for particular applications.

Although other emission scaling forms have proven effective (Bergamaschi et al., 2009; Jiang et al., 2015), we stick with exponential scaling factors here both as a first demonstration, and to be consistent with log-normal statistics for emission rates.  $x$  is resolved on the grid scale and across hourly discretized emission rates; the temporal resolution is customizable. Fletcher and Zupanski (2007) showed that a cost function utilizing this exponential transform — which was previously applied to emission inversions by, e.g., Müller and Stavrakou (2005), Elbern et al. (2007), and Henze et al. (2009) — converges toward the median of a multivariate log-normal distribution for  $\beta$ . Our approach enables the use of existing WRFDA optimization algorithms, with a simple modification described in Sec. 2.3.5.

### 2.3.3 **Incremental 4D-Var**

Here we apply incremental 4D-Var as first introduced by Courtier et al. (1994), utilizing the existing software architecture in WRFDA, and extended to accommodate exponential emission scaling factor CVs. Incremental 4D-Var starts from the assumption that model evaluations of perturbed CVs at observation time  $k$  can be expressed by

$$G(x + \delta x) \approx G(x) + G\delta x,$$

where  $G$  is the Jacobian. The full matrix is too large to store in memory, but the product  $G\delta x$  is found through the TLM, transforming increments in CV space to perturbations in observation space. With the assumption, Model-observation concentration

errors might also be treated as being log-normally distributed, since concentrations are positive definite. Still, the positive definite constraint on emissions ensures that the same applies to modeled concentrations, and we find that treatment to be effective. Introducing log-normality in the observations would corrupt the quadratic form of Eq. 5, the linearized problem is

$$\begin{aligned} \min_{\delta \mathbf{x}^k} J(\delta \mathbf{x}^k) &= \frac{1}{2} \frac{[\delta \mathbf{x}^k + (\mathbf{x}^{k-1} - \mathbf{x}_b)]^\top \mathbf{B}^{-1}}{[\delta \mathbf{x}^k + (\mathbf{x}^{k-1} - \mathbf{x}_b)]} \\ &\quad - \frac{1}{2} \frac{(\mathbf{G}^{k-1} \delta \mathbf{x}^k - \mathbf{d}^{o,k-1})^\top \mathbf{R}^{-1}}{(\mathbf{G}^{k-1} \delta \mathbf{x}^k - \mathbf{d}^{o,k-1})}. \end{aligned}$$

- 5 Each increment-1, which is necessary to derive the closed form solution of the additive increment in Eq. 10. Two alternatives to our approach that include log-normal observations are proposed by Fletcher and Jones (2014), who introduced a geometric incremental formulation with a non-quadratic cost function, and Song et al. (2016), who devised a quadratic approximation to the additive incremental log-normal cost function.

The scaling factor control variables necessitate a special treatment of prior error variance. The common practitioner may have some intuition about multiplicative emission uncertainties in  $\beta$  space (e.g., “factor of 2,  $\delta \mathbf{x}^k$ , is found in sequential outer loop iterations, where the inner loop solves the quadratic cost function in Eq. 1 using linear optimization.  $k$  is the number of the current outer loop. The superscript on  $\mathbf{G}^{k-1}$  denotes that it is linearized around the state from the previous iteration, 3, 4, etc.”), but not of the variance in exponential CV ( $\mathbf{x}$ ) space that would populate the diagonal terms of  $\mathbf{B}$ . A vector that follows a multivariate log-normal distribution ( $\beta \sim \mathcal{LN}(\boldsymbol{\mu}, \mathbf{B})$ ) is simply the exponential of a different vector that follows a multivariate Gaussian distribution (i.e.,  $\mathbf{x} \sim \mathcal{N}(\boldsymbol{\mu}, \mathbf{B})$ ). According to, e.g., Halliwell (2015), the sample mean and covariance of  $\beta$  across many realizations are

$$\mathbf{G}^{k-1} \mathbb{E}[\beta^0]_i = \underbrace{\boldsymbol{\mu}_{\beta^0}} = \exp\left(\underbrace{x_{b,i} + \frac{1}{2} \mathbf{B}_{x,ii}}\right) \quad (12)$$

$\mathbf{d}^{o,k-1}$  is the innovation between observations and model values in the previous iteration:

$$\mathbf{d}^{o,k-1} = \mathbf{y}^o - \mathbf{G}(\mathbf{x}^{k-1}).$$

20 and

$$\mathbf{B}_{\beta^0,ij} = \exp\left[x_{b,i} + x_{b,j} + \frac{1}{2}(\mathbf{B}_{x,ii} + \mathbf{B}_{x,jj})\right] (\exp \mathbf{B}_{x,ij} - 1), \quad (13)$$

respectively, where  $i$  and  $j$  are general indices coinciding with individual CV members,  $\mathbb{E}$  is the expectation operator and  $\exp$  is the natural exponential function. The subscript  $\beta^0$  indicates a variable is evaluated in log-normal space in the zeroth outer iteration, when  $k = 0$ , and the subscript  $x$  indicates an evaluation in Gaussian CV space. In that Gaussian space,  $\mathbf{x}_b$  is the mean, median, and mode. As Eq. 12 shows, the expected value, or mean, of  $\beta^0$  is not equal to its median,  $\exp x_{b,i}$ , the latter being the central tendency we find by minimizing Eq. 7.

In an emission inversion for a single chemical species,  $n = n_x n_y n_t = O(10^5 - 10^6)$ , depending on the domain size and temporal aggregation. Since the number of members in  $\mathbf{B}$  is equal to  $n^2$ , finding its inverse is computationally infeasible. To circumvent that challenge, Barker et al. (2004) implemented a control variable transform (CVT) through a square root preconditioner,  $\mathbf{U}$ , in WRFDA. The increment is transformed as  $\delta \mathbf{x}^k = \mathbf{U} \delta \mathbf{v}^k$ . Equation 13 has not been used in previous

5 emission inversions to translate relative emission uncertainties into the exponential space. When grid scale relative emission uncertainties are less than  $\times 3$ , there is not much error in assuming that

$$(\sigma_{\beta^0, i} + 1)^2 \approx \frac{\exp(x_{b, i} + \sigma_{x_{b, i}})}{\exp(x_{b, i} - \sigma_{x_{b, i}})} = (\exp \sigma_{x_{b, i}})^2,$$

which is equivalent to

$$\sigma_{\beta^0, i} + 1 \approx \exp \sigma_{x_{b, i}}, \quad (14)$$

10 and its inverse

$$\sigma_{x_{b, i}} \approx \log(\sigma_{\beta^0, i} + 1). \quad (15)$$

$(\sigma_{\beta^0} + 1)$  is the multiplicative uncertainty. For example,  $\sigma_{\beta^0} = 2$  gives a factor of three ( $\times 3$ ) relative emission uncertainty. For our case, where  $\mathbf{B} = \mathbf{U}\mathbf{U}^\top$ ,  $\mathbf{U}^\top \mathbf{B}^{-1} \mathbf{U} = \mathbf{I}_n$ , and  $\mathbf{I}_n \in \mathcal{R}^{n \times n}$  is  $\mathbf{x}_b = \mathbf{0}$ , Eq. 14 diverges from Eq. 13 by less than 3% in terms of an error in  $(\sigma_{\beta^0, i} + 1)$  for  $\sigma_{x_{b, i}} \in [0, \log(2)]$ , but reaches 100% mismatch at  $\sigma_{x_{b, i}} = \log(4.2)$ . The procedure we describe

15 below should be followed when grid-scale uncertainties are probably above  $\times 2$ , such as for high-resolution inversions of BB sources. Simplifying Eq. 13 for a diagonal term, the identity matrix. The transformed minimization problem is

$$\begin{aligned} \min_{\delta \mathbf{v}^k} J(\delta \mathbf{v}^k) &= \frac{1}{2} \frac{(\delta \mathbf{v}^k - \mathbf{d}^{b, k-1})^\top (\delta \mathbf{v}^k - \mathbf{d}^{b, k-1})}{(\mathbf{G}^{k-1} \mathbf{U} \delta \mathbf{v}^k - \mathbf{d}^{o, k-1})^\top \mathbf{R}^{-1} (\mathbf{G}^{k-1} \mathbf{U} \delta \mathbf{v}^k - \mathbf{d}^{o, k-1})}, \end{aligned}$$

where the background departure, summed over all previous outer iterations, is

$$\mathbf{d}^{b, k-1} = - \sum_{k_o=1}^{k-1} \delta \mathbf{v}^{k_o}.$$

20 In addition to circumventing calculating  $\mathbf{B}^{-1}$ , the preconditioner reduces the condition number of the problem, speeding up the minimization process.  $i^{\text{th}}$  prior variance of  $\beta^0$  is

$$\sigma_{\beta^0, i}^2 = \exp \left[ 2x_{b, i} + (\sigma_{x_{b, i}})^2 \right] \left[ \exp(\sigma_{x_{b, i}})^2 - 1 \right]. \quad (16)$$

This is identical to the variance transformation between univariate log-normal and Gaussian distributions. However, we want the inverse of this relationship,

$$25 \quad \sigma_{x_{b, i}} = \sqrt{\log \left[ 1 + \frac{(\sigma_{\beta^0, i})^2}{\exp(2x_{b, i} + (\sigma_{x_{b, i}})^2)} \right]}. \quad (17)$$

With an initial guess of  $\sigma_{x_{h,i}} = 0$ , Eq. 17 converges in recursion for reasonable ranges of  $\sigma_{\beta^0,i}$ . This transformation only needs to be applied during preprocessing, and only once for each unique value of prior relative emission uncertainty.

### 2.3.3 Error-Gaussian covariance

WRFDA-Chem utilizes a very similar CVT as WRFDA, with some modification for the scaling factor control variables. The error covariance matrices in Eq.7 are estimated using existing knowledge of the underlying system. We assume that the off-diagonal covariances in  $\mathbf{B}$  are Gaussian in nature. These are defined through the CVT in WRFDA-Chem, which only differs from that of WRFDA in order to account for the temporal distribution of emissions. The transform  $\delta\mathbf{x}^k = \mathbf{U}\delta\mathbf{v}^k$  is performed through two separate operations as  $\mathbf{U} = \mathbf{U}_t\mathbf{U}_h$ . Although the horizontal transform ( $\mathbf{U}_h$ ) only deals with correlations in the  $x$  and  $y$  directions, and the temporal transform ( $\mathbf{U}_t$ ) only does so in the temporal dimension, they are both  $n \times n$ , with sub-matrices along the diagonal of dimension  $(n_x n_y) \times (n_x n_y)$  and  $(n_t) \times (n_t)$ , respectively. The computational overhead of multiplying by either transform is reduced by only handling the non-zero elements.  $\mathbf{U}_h$  is carried out using recursive filters (Barker et al., 2004) and the scalar correlation length scale,  $L_h$  (Barker et al., 2004).

The temporal transform,  $\mathbf{U}_t$ , is constructed in a similar fashion as the vertical transform in WRFDA for meteorological CVs (Barker et al., 2004), except that herein we use all of its eigenmodes. The user specifies the duration of emission scaling factor bins (in minutes), the temporal correlation timescale ( $L_t$ , in hours), and the grid-scale relative emission uncertainty,  $\sigma_x$ . WRFDA-Chem converts these selections to a covariance sub-matrix  $\mathbf{B}_t = \Sigma\mathbf{C}\Sigma \in \mathbb{R}^{n_t \times n_t}$   $\mathbf{B}_t = \Sigma\mathbf{C}\Sigma \in \mathbb{R}^{n_t \times n_t}$ , where  $\mathbf{C}$  is the temporal correlation matrix and  $\Sigma = \sigma_x \mathbf{I}_{n_t}$ .  $\mathbf{B}_t$  is square, symmetric, and positive-definite. Similar to Saide et al. (2015),  $\mathbf{C}$  is defined using an exponential decay,

$$C_{ij} = e^{-\frac{\Delta t}{L_t}}, \quad (18)$$

where  $\Delta t$  is the time elapsed between the beginning of two particular emission steps. The covariance is decomposed into eigenmodes as  $\mathbf{B}_t = \mathbf{E}_t \Lambda_t \mathbf{E}_t^\top$ ; these are readily calculated, because the dimension of  $\mathbf{B}_t$  is the square of the number of emission time steps (e.g., 24 steps for hourly scaling factors in a single day inversion). Throughout the optimization, the temporal transform is carried out through multiplication by

$$\mathbf{U}_t = \begin{bmatrix} \mathbf{E}_t \Lambda_t^{1/2} & \dots & \mathbf{0} \\ \vdots & \ddots & \vdots \\ \mathbf{0} & \dots & \mathbf{E}_t \Lambda_t^{1/2} \end{bmatrix} \quad (19)$$

and its transpose.

In general, the prior variances are estimated in the form of multiplicative emission uncertainty in  $\beta$  space (e.g., “factor of 2, 3, 4, etc.”), not in the exponential CV ( $x$ ) space. The covariances (off-diagonal terms of  $\mathbf{B}$ ) defined previously are The observation-model errors are also assumed to be applicable in CV space. Transformations between the expectations and covariances of a multivariate log-normal ( $\beta \sim \mathcal{LN}(\mu_{\beta^0}, \mathbf{B}_{\beta^0})$ ) and a Gaussian distribution (i.e.,  $x \sim \mathcal{N}(x_b, \mathbf{B}_x)$ ) are derived

by, e.g., Halliwell (2015), as

$$\mathbb{E}[\beta^0]_i = \mu_{\beta^0} = \exp\left(x_{b,i} + \frac{1}{2}\mathbf{B}_{x,ii}\right) \quad (20)$$

and

$$\mathbf{B}_{\beta^0,ij} = \exp\left[x_{b,i} + x_{b,j} + \frac{1}{2}(\mathbf{B}_{x,ii} + \mathbf{B}_{x,jj})\right] (\exp \mathbf{B}_{x,ij} - 1), \quad (21)$$

- 5 respectively, where  $i$  Gaussian, and  $j$  are general indices coinciding with individual CV members,  $\mathbb{E}$  is the expectation operator and  $\exp$  is the natural exponential function. The subscript  $\beta^0$  indicates a variable is evaluated in lognormal space in the previous iteration, when  $k=0$ , and the subscript  $x$  indicates an evaluation in CV space. Since the CVs are normally distributed,  $x_b$  is the mean, median, and mode. As Eq. 12 shows, the expected value, or mean, of  $\beta^0$  is not equal to its median,  $\exp x_{b,i}$ , the latter being the characteristic we use here. The prior linear scaling factor variances are

$$10 \quad \sigma_{\beta^0,i} = \exp\left[x_{b,i} + \frac{1}{2}(\sigma_{x_b,i})^2\right] \left[\exp(\sigma_{x_b,i})^2 - 1\right]^{\frac{1}{2}}. \quad (22)$$

This is identical to the variance transformation between univariate log-normal and Gaussian distributions. With an initial guess of  $\sigma_{x_b,i} = 0$ , the recursive inverse relation,

$$\begin{aligned} \sigma_{x_b,i} &= \sqrt{\log\left[1 + \frac{(\sigma_{\beta^0,i})^2}{(\mu_{\beta^0,i})^2}\right]} \\ &= \sqrt{\log\left[1 + \frac{(\sigma_{\beta^0,i})^2}{\exp(2x_{b,i} + (\sigma_{x_b,i})^2)}\right]}. \end{aligned} \quad (23)$$

converges for reasonable ranges of  $\sigma_{\beta^0,i}$ , which is the additive uncertainty in  $\beta$ . Earlier emission inversion works (e.g., Elbern et al., 2007) a

- 15 that

$$(\sigma_{\beta^0,i} + 1)^2 \approx \frac{\exp(x_{b,i} + \sigma_{x_b,i})}{\exp(x_{b,i} - \sigma_{x_b,i})} = (\exp \sigma_{x_b,i})^2,$$

which is equivalent to

$$\sigma_{\beta^0,i} + 1 \approx \exp \sigma_{x_b,i}, \quad (24)$$

and its inverse

$$20 \quad \sigma_{x_b,i} \approx \log(\sigma_{\beta^0,i} + 1). \quad (25)$$

$(\sigma_{\beta^0} + 1)$  is the multiplicative error in emissions. For example,  $\sigma_{\beta^0} = 2$  gives a factor of three ( $\times 3$ ) uncertainty. In our case  $x_{b,i} = 0$  and Eq. 14 gives an error in  $\sigma_{\beta^0,i} + 1$  less than 3% for  $\sigma_{x_b} \in [0, \log(2)]$ , but reaches 100% mismatch at  $\sigma_{x_b} = \log(4.2)$ . Previous works that use Eq. 15 with relative emission errors less than  $\times 3$  do not warrant corrections. However, utilizing Eq. 17

is important for high-resolution inversions of BB sources, where grid-scale uncertainties are probably above that threshold. Sections 3.3 and 4 include further discussion of emission uncertainty.

The observation model their covariance matrix,  $\mathbf{R}$ , is assumed diagonal. For each  $p$  measurement, measurement,  $p$ , the total variance is defined as the sum of observation ( $\sigma_{p,o}^2$ ) and model ( $\sigma_{p,m}^2$ ) components, following the approach by Guerrette and Henze (2015).  $\sigma_{p,m}$  is determined from an ensemble of 156 WRF-Chem model configurations. Each member uses a unique combination of options for PBL mixing, surface layer, LSM, and longwave and shortwave radiation options, as well as includes or excludes microphysics and subgrid cumulus convection.  $\sigma_{p,o}$  accounts for instrument precision, representativeness error, and averaging of measurements to the model resolution. We do not use the weighting term previously defined by Guerrette and Henze (2015), because small residuals with low uncertainty do not appear to hinder the inversion process. Refer to that work for more particular details of how  $\sigma_{p,m}^2$  and  $\sigma_{p,o}^2$  are calculated.

### 2.3.4 Linear optimization

With all of the terms in Eq. 7 defined, the linear optimization proceeds as follows. The inner loop seeks the optimal  $\delta \mathbf{v}^k$ , at which point

$$\begin{aligned} \nabla_{\delta \mathbf{v}} J &= \underline{\underline{(\delta \mathbf{v}^k - \mathbf{d}^{b,k-1})}} \\ &+ \underline{\underline{\mathbf{U}^\top \mathbf{G}^{k-1 \top} \mathbf{R}^{-1} (\mathbf{G}^{k-1} \mathbf{U} \delta \mathbf{v}^k - \mathbf{d}^{o,k-1})}} \\ &= \underline{\underline{\mathbf{0}}}. \end{aligned}$$

The action of  $\mathbf{G}^{k-1 \top}$  on a vector is calculated with the ADM. Solving for the CVT increment,

$$\begin{aligned} \delta \mathbf{v}^k &= \underline{\underline{(\mathbf{I}_n + \mathbf{U}^\top \mathbf{G}^{k-1 \top} \mathbf{R}^{-1} \mathbf{G}^{k-1} \mathbf{U})^{-1} (\mathbf{d}^{b,k-1} + \mathbf{U}^\top \mathbf{G}^{k-1 \top} \mathbf{R}^{-1} \mathbf{d}^{o,k-1})}} \\ &= \underline{\underline{-[\mathcal{H}_{\delta \mathbf{v}}]^{-1} \nabla_{\delta \mathbf{v}} J|_{\delta \mathbf{v}^k = \mathbf{0}}}}, \end{aligned}$$

where  $\mathcal{H}_{\delta \mathbf{v}} = \nabla_{\delta \mathbf{v}}^2 J$  is the Hessian of Eq. 7.  $\mathcal{H}_{\delta \mathbf{v}}$  and its inverse are too large to store and calculate explicitly. Through an iterative process, the inner loop linear optimization estimates the product of the inverse Hessian with the initial cost function gradient. Finite precision and the problem dimension,  $n$ , prevent Eq. 9 from being exactly equal to zero. Increasing the number of inner loop iterations to approach such an objective does not necessarily speed up convergence in the nonlinear problem of Eq. ???. Large innovations,  $\mathbf{d}^{o,k}$ , may remain after relinearization around the new state  $\mathbf{x}^k$ .

The two linear optimization algorithms available in WRFDA are Conjugate Gradient and the Lanczos recurrence described on p. 493 of Golub and Van Loan (1996). We use Lanczos, which aids the estimation of posterior error as described in Sec. 2.3.4. Linear optimization strategies are designed to solve a quadratic problem

$$\begin{aligned} \min_{\hat{\mathbf{x}}} F(\hat{\mathbf{x}}) &= \underline{\underline{\frac{1}{2} \hat{\mathbf{x}}^\top \mathbf{A}' \hat{\mathbf{x}} - \hat{\mathbf{x}}^\top \mathbf{b} + c}} \\ \mathbf{A}' \hat{\mathbf{x}} &= \underline{\underline{\mathbf{b}}}. \end{aligned}$$

The equivalence of incremental 4D-Var (Eqs. 7) and Gauss-Newton (GN) to solve Eq. ?? is demonstrated in Appendix A; there, we repeat some derivations by Lawless et al. (2005), Gratton et al. (2007), and Tshimanga et al. (2008) using the notation defined herein. The advantage of this equivalence is that any studies pertaining to issues and advances with GN have the potential to inform incremental 4D-Var; we exploit this in Sec. 2.3.5 to improve the relinearization behavior for nonlinear CVs.

5

### 2.3.4 Posterior Error

Posterior uncertainty is a useful measure to diagnose the value of an emission inversion. While areas where uncertainty has been reduced from the prior include new information from the observations, areas without uncertainty reduction are simply a new realization of the prior. In a region of linear behavior of the full a nonlinear DA cost function, Eq. ??, and when  $\delta x$  is

10 normally distributed, the posterior covariance, AP<sup>a</sup>, is equal to the inverse Hessian of Eq. 1 (e.g., Thacker, 1989; Fisher and Courtier, 1995):

$$\underline{\mathbf{A}\mathbf{P}^a} = [\mathcal{H}_{\delta x}]^{-1}, \quad (26)$$

where

$$\mathcal{H}_{\delta x} = \mathbf{B}^{-1} + \mathbf{G}^{k-1\top} \mathbf{R}^{-1} \mathbf{G}^{k-1}. \quad (27)$$

15 Combining this with the expression for the Hessian of Eq. 7 we used in Eq. 10 gives a conversion from the transformed variable space

$$\mathcal{H}_{\delta v} = \mathbf{U}^\top \mathcal{H}_{\delta x} \mathbf{U}. \quad (28)$$

Using a Lanczos recurrence to solve the inner loop optimization problem in Eq. 7 has the benefit of producing the means to approximate  $[\mathcal{H}_{\delta v}]^{-1}$ , which we demonstrate in Appendix AB. The final result of that derivation is the posterior error,

$$\begin{aligned} \underline{\mathbf{A}\mathbf{P}^a} &= \mathbf{U} [\mathcal{H}_{\delta v}]^{-1} \mathbf{U}^\top \\ &\approx \mathbf{B} + \sum_{k_i=1}^l (\lambda_{k_i}^{-1} - 1) (\mathbf{U} \hat{\mathbf{v}}_{k_i}) (\mathbf{U} \hat{\mathbf{v}}_{k_i})^\top, \end{aligned} \quad (29)$$

in terms of the eigenvectors of  $\mathcal{H}_{\delta v}$ ,  $\hat{\mathbf{v}}_{k_i} = \mathbf{Q}_l \hat{\mathbf{w}}_{1k_i}$ . Each inner iteration,  $k_i$ , leading up to the current iteration  $l$  of the Lanczos optimization, produces (1) a new *Lanczos vector* in the orthonormal matrix  $\mathbf{Q}_l = [\hat{\mathbf{q}}_1, \dots, \hat{\mathbf{q}}_l]$  and (2) a new row and column in a tridiagonal matrix  $\mathbf{T}_l$ , whose  $k_i^{\text{th}}$  eigenpair is  $(\lambda_{k_i}; \hat{\mathbf{w}}_{1k_i})$ . AP<sup>a</sup> is a low-rank update to  $\mathbf{B}$ , because  $l \ll n$  due to the wall-clock requirements of running the TLM and ADM once per iteration. Equation 29 is consistent with earlier publications

25 (Fisher and Courtier, 1995; Meirink et al., 2008).

### 2.3.5 Damped-Gauss-Newton Nonlinear Optimization



Each CV increment  $\delta x^k$  must be small enough to keep the error associated with the tangent linear TL assumption, Eq. 5, below some threshold. Otherwise the cost function may actually increase between successive  $k$ 's. However, the nonlinearity of the log-normal prior emission errors contributes to failures in that respect. For demonstration, we consider the treatment of  $\beta \in \beta$  and  $x \in x$  associated with a single grid cell. At the end of an outer loop,  $x$  is updated, and  $\beta$  is

$$\beta^k = e^{x^{k-1} + \delta x^k} = \beta^{k-1} e^{\delta x^k}.$$

Thus, the increment in  $\beta$  is

$$\delta \beta^k = \beta^k - \beta^{k-1} = \beta^{k-1} (e^{\delta x^k} - 1),$$

which reveals the nonlinear nature of the emission increment. This contrasts with the TLM version of the transform in Eq. 11, which states

$$\delta \beta^k = e^{x^{k-1}} \delta x = \beta^{k-1} \delta x^k.$$

The ratio of  $\delta \beta^k / \delta \beta^k$  gives the multiplicative error in the tangent linear assumption during relinearization:

$$\epsilon_{TL} = \frac{e^{\delta x^k} - 1}{\delta x^k}.$$

Around  $\delta x^k = 0$ , the tangent linear relationship very closely matches the nonlinear equation, giving  $\epsilon_{TL} \approx 1$ . For  $\delta x^k > 0$ ,  $\epsilon_{TL}$  grows nearly exponentially toward  $\infty$ , reaching  $\times 2$  at  $\delta x^k \approx 1.26$ . When  $\delta x^k < 0$ ,  $\epsilon_{TL}$  shrinks asymptotically toward zero, reaching  $\times 0.5$  at  $\delta x^k \approx -1.59$ . As  $\epsilon_{TL}$  is farther from unity, it is more likely that the linear optimization will generate  $J(x^k) > J(x^{k-1})$ . Not only do we never want that to happen, but we would prefer to advance toward a more optimal solution as quickly as possible.

Violation of the TL assumption and potential solutions are discussed in several DA works. The prevailing strategy in chemical 4D-Var is to apply a non-incremental nonlinear optimization strategy quasi-Newton optimization (e.g., Henze et al., 2009; Bergamaschi et al., 2009), eliminating the inner-outer loop structure of GN. Implementing this approach in WRFDA with posterior error estimation would be a considerable additional effort. The use of Also, as we mentioned in Sec. 2.1, using the tangent linear model in the inner loop also presents computational advantages for dual resolution multi-incremental 4D-Var (e.g., Zhang et al., 2014b). Alternatively,

There are several alternative approaches, which stem from the equivalence between incremental 4D-Var and GN. Gratton et al. (2013) discuss application of GN in a trust region framework, which has the limitation that a portion of the computationally expensive outer loop increments will be rejected. Some authors have successfully applied the Levenberg-Marquardt algorithm in EnKF (e.g., Chen and Oliver, 2013; Mandel et al., 2016) by adding a regularization term to the cost function.

A simpler approach yet That method requires performing the inner loop approximation of  $[\mathcal{H}_{\delta x}]^{-1}$  multiple times, once for each value of a scalar regularization parameter. A similar and cheaper approach is damped GN (DGN), which changes the

inner loop increment in Eq. 10 to

$$\delta v^k = -\eta^k [\mathcal{H}_{\delta v}]^{-1} \nabla_{\delta v} J|_{\delta v^k=0}, \quad (30)$$

and uses a line search to find an optimal scalar  $\eta^k \in (0, 1]$  ~~at~~after the completion of each outer loop iteration (Kelley, 1999).

DGN is based on the Armijo rule, which states that the increment found by GN points toward a direction of lower  $J$ ; if the step size terminus is outside the linear behavior of the model, decrease the step size. This strategy is implemented in WRFDA-Chem  
5 ~~uses a non-optimal variant we call heuristic DGN, that requires user intervention to determine  $\eta^k$ . Results with a simplified test problem in MATLAB indicate that the resultant CV's near the optimum are nearly identical either with the line search or heuristic damping. However, heuristic DGN likely increases the number of outer iterations required to converge, and motivates implementing the line search in future work. The same MATLAB tests showed that applying a range of damping coefficient~~  
10 ~~values before the Lanczos process has no impact on the estimated  $\mathcal{H}_{\delta v}^{-1}$  for log-normally distributed emission errors.~~

~~The heuristics to determine  $\eta^k$  are a function of the prior covariance. As the uncertainty increases,  $\eta^k$  should be smaller, because the initial gradient and resulting increments will be larger in magnitude. Additionally,  $\eta^k$  should increase in each subsequent outer loop iteration as the nonlinear optimum is approached, since the diminishing increment magnitude will eventually satisfy the tangent linear assumption. We found that a prior multiplicative emission uncertainty of  $\times 3.8$ , coinciding  
15 ~~with CV uncertainty of  $\sigma_x = 1.099$ , requires  $\eta^0 = 0.4$  in the first outer loop iteration.  $\eta^0$  should be adjusted in inverse proportion to  $\sigma_x$ . Presumably there is some lower limit of  $\sigma_x$  where no damping is required. In WRFDA-Chem, the damping ramps linearly back to 1 in the final outer loop.~~~~

### 3 ARCTAS-CARB Case Study

#### 3.1 Inversion setup

20 From late May until 20 June 2008, the southwest U.S. experienced a very dry period with little to no cloud cover appearing in MODIS true color imagery, and no recorded rainfall for most of California. On 21 June, the Aqua and Terra satellites recorded cloud cover for much of Northern California, south of San Francisco, and along the Sierra Nevada mountain range, and there were wide-spread lightning strikes over night. As is shown in Fig. 1, there was a spike in fire detections during the night between 21 and 22 June. Thus, from the morning through evening of 22 June, California experienced a transient fire  
25 initiation event. The wild fires burned well into July, exacerbating poor air quality throughout the state. The ~~22-20~~ June flight of ARCTAS-CARB ~~disembarked~~characterized Northern California anthropogenic sources, but was not influenced by fires. The  
22 June flight embarked from Los Angeles, ~~swept out over the ocean~~transited the off-shore Pacific inflow, flew directly through smoke from forest fires in Northern California, then returned down the coastline. That flight encountered anthropogenic sources of BC in the morning, and BB sources for the remainder after returning to land. The 24 June flight passed back and forth in the  
30 downwind region between Los Angeles and San Diego, measuring the outflow from those cities and the transportation ~~lines~~  
~~between them. A third~~between them, and 1 day old diluted BB outflow from the north. A fourth flight on 26 June flew in the free troposphere from Los Angeles, north over the fires, and exited the model domain to the east.

We use WRFDA-Chem 4D-Var to constrain BB and anthropogenic aerosols on three days during ARCTAS-CARB using aircraft and IMPROVE surface observations. We utilize aircraft measurements of absorbing carbonaceous aerosol at 10 s intervals from the single particle soot photometer (SP2) on 22, 24, and 26 June (Sahu et al., 2012). For this study, we assume equivalency between the SP2 measurement and modeled BC, and re-average to the 90 s model time step using the revision 3 product, a process described in Guerrette and Henze (2015). We also use 24-hour average surface observations of light absorbing carbon (LAC) on 23 and 26 June (Malm et al., 1994), assuming an equivalence with modeled BC, and ignoring the 7% high bias relative to the SP2 found by Yelverton et al. (2014). All treatments of observations are identical to those described in Guerrette and Henze (2015), including an analysis of model-observation BC mismatch that feeds into the inverse modeling study.

Using measurements from 22, 23, and 24 June, the 4D-Var system constrains anthropogenic and BB sources simultaneously. Data collected between 07:00:00-16:00:00 LT on 22 June is used in an inversion from 22 June, 00:00:00 UTC to 23 June, 00:00:00 UTC, during which time WRF-Chem is run freely, without nudging. The emission scaling factors for this 24-hour time period for both source types are applied to subsequent days from 23-26 June in a cross validation experiment. The 24 and 26 June aircraft and 23 and 26 June surface observations are used to analyze the utility of observationally constrained scaling factors found on one day to fix source errors on subsequent days. The 23 and 24 June surface and aircraft data is used in a 48-hour inversion from 23 June, 00:00:00 UTC to 25 June, 00:00:00 UTC, also without nudging. Cross validation is performed for these source estimates using 26 June surface and aircraft data.

Through preliminary testing, we found that horizontal correlation length scales on the order of the grid spacing provides the lowest posterior cost function. For both time periods, this length scale is set to twice the grid scale,  $L_h = 36$  km. The emission scaling factors are aggregated in each hour, which coincides with the emission file reading interval for both source types. The correlation scale is set to  $L_t = 4$  h, following Saide et al. (2015). In addition to spreading error information across adjacent grid cells, the correlation scales reduce the effective number of CVs. Through sensitivity tests where we considered the smoothness of the posterior and the stationary posterior cost function value, and after consulting published values for regional emission uncertainties (see Sec. 1) in different global settings, we use a [relative](#) grid-scale BB uncertainty of  $\times 3.8$ . The BB uncertainty might also be approximated from the ratio of prior domain-wide total emissions between FINNv1.0 and QFED, which is given in Table 5 as  $\times 3.5$ . If the median emission strength lies in the middle of QFED and FINNv1.0, then the prior domain-wide relative uncertainty is  $\times \sqrt{3.5} = \times 1.8$ . The uncertainty would then need to be inflated further to account for spatial and temporal disaggregation and the possibility that grid-scale sources from the two inventories do not bound the true value [\(see Sec. 3.3\)](#). The prior anthropogenic grid-scale [relative](#) uncertainty is set to  $\times 2$ , which is within the reasonable bounds discussed in Sec. 1.

In addition to these standard settings, several sensitivity scenarios are used to gauge the sensitivity of the posteriors during two time periods to alternative inversion settings. The full set of scenarios are summarized in Table 1, and are as follows. FINNv1.0 is used as the default BB inventory in a scenario called FINN\_STD for both inversion periods. QFED\_STD uses the QFEDv2.4r8 BB inventory. Both FINN\_L18 and QFED\_L18 use  $L_h = 18$  km. FINN\_V1.5 utilizes the FINNv1.5 BB inventory. For the 23/24 June inversion, we show results for both QFED\_STD and FINN\_STD, the latter of which includes variations where either surface or aircraft observations are excluded. The number of aircraft observations is  $N_{\text{obs}} = 241$  on 22

June and  $N_{\text{obs}} = 302$  on 24 June. There were  $N_{\text{obs}} = 35$  active surface sites on 23 June, 13 of them within California. We use six outer iterations consisting of 10 inner iterations each. Given the number of inner iterations used, and the wall-time of the tangent linear plus the adjoint ( $\times 10$  longer than the nonlinear model), the cost of incremental 4D-Var is approximately  $\times 600$  more than that of a single forward simulation, which is much cheaper than using finite difference methods to approximate derivatives instead of the linearized models when  $n \sim 10^5$ .

### 3.2 Posterior model performance

~~The~~ For a linear model operator and Gaussian distributed errors, the cost function can be used to evaluate the consistency of the statistics in **B** and **R**. The  $\chi^2$  criteria states that the posterior cost function should be equal to  $\frac{1}{2}N_{\text{OBS}}$  (e.g., Tarantola, 2005). The convergence properties of the 22 and 23/24 June inversion scenarios are shown in the outer loop cost function progression in Fig. 3. All of the 22 June scenarios led to comparable cost function values at numerical convergence, as shown in Fig. 3. The gradient norms are also reduced by nearly two orders of magnitude in all cases. ~~The  $\chi^2$  criteria states that the posterior cost function should be equal to  $\frac{1}{2}N_{\text{OBS}}$ .~~ In all of the scenarios,  $J$  converges to approximately  $N_{\text{OBS}}$ , indicating that a portion of the model errors are not fully spanned by prior emission errors. For the 23/24 June inversion, QFED\_STD reaches a lower cost function value, and both scenarios achieve similar  $\chi^2$  values as the 22 June cases. Scrutinizing other sources of error (e.g., initial and boundary conditions for BC and meteorological variables, transport, BB plumerise, and model discretization) either independent from source strengths or simultaneously in the inversion framework should elicit further cost function reductions.

~~The~~ Considering the top subplot in Fig. 4, the non-emission sources of error ~~for on~~ 22 June are evident ~~in the time series in Fig. 4.~~ ~~The~~ when the prior and posterior predictions are on top of each other, and remain on the edges of the low probability uncertainty region. For example, the observations before 08:00 LT after takeoff from Edwards are likely sensitive to the Pacific inflow, but not early morning emissions. Since these locations have relatively small uncertainties, the posterior cost function will never be reduced there.

Figure 4 also shows that during the inversion period the posterior is within the combined model/observation uncertainty (see Sec. 2.3.3) much more often than the prior. ~~The only time during the inversion when the forecast degrades is for an observed peak at 22 June, 08:00. Model uncertainty is higher in locations where the prior concentration is higher, due to variability in the configuration ensemble boundary layer heights (Guerrette and Henze, 2015). This high prior uncertainty in **R** allows the stronger constraint at 08:30 to dominate the morning anthropogenic emissions, since this flight portion was confined to Los Angeles.~~ In the afternoon, when the DC-8 passed over the wildfires, an increase in posterior emissions captures several of the observed BC peaks. The posterior is able to match the high-resolution variability of the observations at 13:30 LT, which may support the validity of the temporal averaging scheme. ~~The only time during the inversion when the forecast degrades is for an observed peak at 22 June, 08:00 LT. The larger absolute observation uncertainty at that time relative to that at 08:30 LT enforces a weaker constraint in the inversion. Coupled with the assumed relative emission error correlation length scale and the close proximity of these two measurements, that stronger constraint at 08:30 LT dominates the morning anthropogenic emission analysis increment.~~

The  $R^2$  coefficients and slopes for linear fits between the prior and posterior and both aircraft and surface observations are summarized in Tables 2 and 3. Those results include cross-validation data on non-inversion days, which is discussed in Sec. 3.5. For both inversion periods, there are considerable model performance improvements for observations that are used in the inversion. FINN\_STD improves  $R^2$  from 0.11 to 0.82 and slope from 0.26 to 0.8 on 22 June. QFED\_STD improves  $R^2$  from 0.03 to 0.73 and slope from 0.34 to 0.71. Similar improvements occur for 23 June surface observations during the 23/24 June inversion. The posterior match to 24 June aircraft observations is improved, but not nearly as much as the other two data sets. The 22 June inversion results are also shown in Fig. 5, where the progression of the fit parameters is shown for the multiple scenarios. While all scenarios show similar improvements, the FINN\_STD and QFED\_STD results indicate the posteriors are still underpredicting many low and high concentrations. ~~Overprediction seems to be less of a problem.~~ A similar phenomenon occurs for the 24 June observations in Fig. 6 in the inversion that uses both surface and aircraft observations. On both 22 and 24 June, the remaining low bias is either due to large prior observation and model error (diagonal of  $\mathbf{R}$ ) or due to the prior errors not being sensitive to emission increments.

For the appreciable measured BC concentrations ( $> 0.25 \mu\text{g m}^{-3}$ ), that are likely caused by a source within the model domain and simulation period, the lack of a source-receptor relationship is likely caused by low resolution. Changing a point source to a grid-scale area source changes its effective location. Temporal averaging of the observations will not necessarily solve that problem since perfectly modeled transport could still send a mis-located source in an entirely different direction than the truthfully located source. This effect is evident for valley fires (Strand et al., 2012), since placing the sources in the basin or spreading them throughout the basin and the peaks will result in different “downwind” concentrations. Downwind might be a very different direction if the convective scale winds contribute more information than the mesoscale winds to the true source-receptor relationship. Since the emissions are smoothed in the model and not in reality, the mis-location is more likely to cause under-prediction than over-prediction.

### 3.3 Posterior emissions

Figure 7 shows the prior and posterior BB emissions for FINN\_STD and QFED\_STD during both simulation periods. In that figure there are several outlined emission areas (EAs); each EA was chosen to identify regions where a subset of the grid-scale analysis increment ( $\delta x_{\text{EAX}} \subset \delta x$ ) from both prior inventories is of similar sign. The coordinates of the EAs are listed in Table 4. The two inversions do not reach identical total posterior BC emissions, but they do converge in certain aspects. Table 5 gives the emission subtotals for the EAs. During both inversions, each EA has emission increments of the same sign for both scenarios. Therefore, while domain-wide sources seem to be bounded by the two priors (as evidenced by their convergence), the same might not be true within the individual EAs. EA3, which accounts for the smallest average posterior total, is the only region where the magnitude of the log-ratio between QFED and FINN is smaller in the posterior on 22 June. The ratio is reduced in EA2, but there the FINN posterior is  $\times 2$  larger than that for QFED. On 23/24 June, the two scenarios have less posterior spread in all of the EAs. Although Table 5 indicates large changes in source strengths across the EAs, Figure 8 reveals that a majority of the absolute emission increment (posterior minus prior) in both FINN\_STD and QFED\_STD arose in only a few grid cells,

often where the prior has the largest magnitude. The linear scaling factor pattern is similar between the two scenarios, with those for QFED\_STD shifted toward decreases due to the high prior bias.

The temporal distribution of prior and posterior BB emissions within the four EAs are shown in Fig. 9 across all inversion scenarios on 22 June. The FINNv1.5 prior is an extreme outlier on the local afternoon of 21 June for EA1, EA2, and EA4. The same is true all day on 22 June for EA2, where the posteriors from other scenarios adjust toward the FINNv1.5 prior. Meanwhile, in-at other times when FINNv1.5 appears to converge toward the posteriors found using the other two priors, the prior relative uncertainty of  $\times 3.8$  is too restrictive to allow full convergence, since the priors differ by  $\times 10$ . EA1 is characterized by decreases for all scenarios at all times. EA2, EA3, and EA4 exhibit early morning peaks between 03:00 and 06:00 LT that were not captured in the prior. In separate sensitivity tests, these peaks only appear when  $L_t > 1$  h, and become more prevalent as  $L_t$  is increased. Saide et al. (2015) attributed similar behavior in posterior estimates of the 2013 Rim Fire to persistent large scale burning. Zhang et al. (2012) found similar, less pronounced bimodal behavior for all of North America, which could be more noticeable in a regional inversion. Another possibility on 22 June 2008 is that the early morning burning is caused by the transient fire initiation event, which would explain the ramping of emissions for the QFED and FINNv1.5 posteriors in EA2. For both QFED and FINNv1.0, reducing the correlation length to  $L_h = 18$  km reduces the analysis increment in all EAs. This is especially apparent in EA4 for FINN\_L18, where the increment is negligible.

The differing diurnal patterns in EA2 across scenarios could be attributed to variation in plume heights, QFED regridding errors, and the regularization term of the cost function. The observations most sensitive to EA2 sources were captured within or very near fire plumes. Plume heights are calculated hourly in an online 1D vertical mixing scheme in WRF-Chem (Freitas et al., 2007, 2010; Grell et al., 2011), which depends strongly on burned areas. With FINN, the areas are provided for each fire independently, while for QFED the areas use a default value of  $0.25 \text{ km}^2$  per fire. In both cases, the maximum area burned per grid cell per day is  $2 \text{ km}^2$ . The regridding error discussed in Sec. 2.2 introduces fire locational errors, especially in EA2. A small error in vertical or horizontal mapping of a discrete point source on the model grid could hinder the optimization in distinguishing it from others. The uniform relative uncertainty in the prior inhibits consolidation of multiple posteriors when the prior spread is heterogeneous and sometimes very large. Quantifying the heterogeneity of uncertainty could contribute to posterior agreement between inversions using different priors, as well as to reducing the cost function.

The spread of local emissions provide some sense of that heterogeneity. Each EA covers a region approximately the size of a grid box in a global simulation with a chemical transport model. Due to the nature of variance aggregation, uncertainty grows as the grid scale gets smaller. In individual EAs, the spread between FINNv1.0 and QFED priors is  $\times 2$ - $\times 6$  for both hourly (Fig. 9) and daily (Table 5) strength on 22 June. If the median emission strength lies in the middle, then a proxy for prior EA relative uncertainty is  $\times \sqrt{2} - \times \sqrt{6} = \times 1.4 - \times 2.4$ . Since the two inventories use identical diurnal patterns, the hourly estimate is missing information about uncertainties in daily emission timing. Using the posterior spread in a similar way gives approximate EA uncertainties of  $\times \sqrt{3} - \times \sqrt{10} = \times 1.7 - \times 3.2$  on hourly scales and  $\times \sqrt{2} - \times \sqrt{7} = \times 1.4 - \times 2.6$  on daily scales. This posterior estimate accounts for contributions in the prior definitions, including regridding, plume rise, and diurnal patterns. These ranges provide much more detail estimates than simply taking the domain-wide ratio of total emissions for the campaign period. However, the spread is itself missing information about uncertainty that could be found through carrying

out similar inversions across an ensemble of model configurations and meteorological initial and boundary conditions (e.g., Lauvaux et al., 2016), or by comparing many more inventory priors (e.g., Zhang et al., 2012) (e.g., Zhang et al., 2014a) and posteriors. All this is to say that the BB inventories used in this study are not provided with analytical estimates of uncertainty, and a lack of information for deriving such values at hourly grid-scales is a topic for future research.

5 Figure 10 shows the total prior and posterior anthropogenic emissions and Fig. 11 displays the analysis increment and linear scaling factor for FINN\_STD on 22 June and separately on 23-24 June. The only difference in QFED\_STD, not shown here, is that anthropogenic scaling factors are shifted in the negative direction in the posterior, likely due to the higher bias in that BB prior. The increments found in a new set of EAs are presented in Table 6.

The 23 and 24 June observations provide much more detailed information about anthropogenic sources. The analysis incre-  
10 ment reveals potentially misrepresented city-level emissions in the NEI05 prior. Posterior BC near Barstow, Victorville/Hesperia, Fresno, Edwards Air Force Base, and El Centro/Calexico are increased, while sources near the three coastal cities are decreased. Since Barstow is a crossroads for the BNSF and the Union Pacific railroads, and since Fresno, Victorville/Hesperia, and El Centro/Calexico lie at switching locations for major rail lines, ~~it could be speculated~~ the inversion results may suggest that the prior is missing diesel rail sources of BC. ~~Another possibility is that~~ However, for locations where the prior magnitude of BB  
15 and anthropogenic emissions are of similar magnitude, their posteriors are subject to projection from one sector to another. It is more likely that the low bias fire emissions north of Fresno are responsible for the prior underpredictions of 23 June surface concentration measurements exceeding  $2 \mu\text{g m}^{-3}$  (see Fig. 5 of Guerrette and Henze, 2015). This is corroborated by the posterior BB emissions being scaled up near Fresno on 23 and 24 June, and by the much smaller model bias for IMPROVE on 22 June before the fires started.

20 There are also small negative increments near Los Angeles (EA6) and San Francisco (EA7) during both the 22 June and 23/24 June inversions, which are likely attributable to on-road mobile sources. These results are consistent with model bias in surface and aircraft observations on 20 June near both of those cities (Guerrette and Henze, 2015). McDonald et al. (2015) found a decreasing trend in ambient measurements of BC and in a fuel-based bottom-up inventory for both Los Angeles and San Francisco from 1990 to 2010 that might not be captured for the 2008 model year by the snapshot in NEI05. Using a similar  
25 fuel-based approach, Kim et al. (2016) derived 2010 CO emissions in the South Coast Air Basin surrounding Los Angeles that are  $\times \frac{1}{2}$  the magnitude of NEI05. On-road and other mobile sources make up 36% and 62% of that difference, respectively, and their bottom-up inventory matches more closely with NEI 2011. While not a perfect comparison to BC in 2008, the sign of error in NEI05 relative to the coastal posterior and that study is consistent. An inventory with sector-specific break downs of BC emissions, ~~and~~ additional inversions with more thorough speciated local observations, and higher resolution would all be  
30 required to investigate sector-specific anthropogenic pollution.

### 3.4 Error diagnostics

Analysis of posterior emissions uncertainties is useful for understanding the value of the posterior emissions themselves. The diagonal terms of  $\mathbf{A-P}^a$  are the posterior variances,  $\sigma_{x_a}$ , which are always smaller than prior variances. The variance reduction could instead be presented in  $\beta$  space, by utilizing Eq. 16. However,  $\sigma_{\beta^k,i}^2 < \sigma_{\beta^0,i}^2$  is not guaranteed when  $x_{a,i} > x_{b,i} = 0$ ,



because the posterior relative emission uncertainty depends on  $x_{a,i}$ . For this work, the reductions in variance are presented in CV space. The low-rank estimate of  $\mathbf{A}\mathbf{P}^a$  is only valid for linear perturbations away from  $x_a$ . The final outer loop estimate of  $\mathbf{A}\mathbf{P}^a$  is the most accurate, since it is linearized around the state preceding  $x_a$ . A quantitative measure of error reduction in the  $k_o^{\text{th}}$  outer loop in the  $i^{\text{th}}$  CV is

$$5 \quad \rho_{i,k_o} = 1 - \left( \frac{\mathbf{A}_{i,i} \mathbf{P}_{i,i}^a}{\mathbf{B}_{i,i} \mathbf{B}_{i,i}} \right)_{k_o} \in [0, 1). \quad (31)$$

Values of  $\rho_{i,k_o}$  closer to 1 reflect locations where the observations provide a stronger constraint than the prior. This estimate may not reflect the entire error reduction, since it does not capture potential reductions in previous outer loops. Without propagating updated estimates for  $\mathbf{B}$  to subsequent outer loops (e.g., Tshimanga et al., 2008), we also define  $\rho_{\text{agg}}$ , a qualitative metric that accounts for increases in curvature (decreases in error) in all outer loops:

$$10 \quad \rho_{i,\text{agg}} = 1 - \prod_{k_o=1}^k \left( \frac{\mathbf{A}_{i,i} \mathbf{P}_{i,i}^a}{\mathbf{B}_{i,i} \mathbf{B}_{i,i}} \right)_{k_o} \in [0, 1). \quad (32)$$

$\rho_{i,\text{agg}}$  reveals additional information about observation footprints not shown by  $\rho_{i,k_o=6}$ . The nonlinear nature of the problem means  $\rho_{i,\text{agg}}$  is not quantitative.

Both ( $\rho_{k_o=6}$ ) and  $\rho_{\text{agg}}$  are presented in Figs. 12 and 13 for the BB and anthropogenic members of  $x_a$ , respectively. 50 inner loop iterations were taken in the final outer loop to improve  $\rho$  estimates.  $\rho_{k_o=6}$  is  $< 45\%$  across all scenarios, except for  
 15 QFED\_STD BB sources near the IMPROVE sites on 23/24 June. If the inner loop were halted at 10 iterations, the error reduction estimates are reduced by up to  $\sim 10\%$  (i.e., 35% instead of 45%) in the darkest grid cells. ~~Further decreasing uncertainty would require observing the same phenomena more thoroughly, either for longer periods, with greater spatial coverage, or with more instruments.~~ The BB error reduction shown in Figure 12 has similar spatial distributions for FINN\_STD and QFED\_STD scenarios, but differs significantly between the two time periods due to the different spatial coverage of the observations. The  
 20 reductions in the north on 22 June are more disperse for QFED\_STD, which could be caused by the same regridding errors and plumerise differences that influence the posterior emissions. There is also more error reduction in the south for the QFED\_STD emissions. In general, the grid-scale uncertainty improvement is confined to sources close to the observations.

The most obvious application of  $\rho$  is to evaluate the footprint of a set of measurements. For example, the large relative BB emission increments in EA1-EA3 on 23/24 June indicate that distant observations can have a large impact on the posterior  
 25 emissions magnitudes. However,  $\rho_{i,k_o=6}$  in Fig. 12 indicates there is nearly zero uncertainty reduction for those emissions. Also, upon considering the last two columns of Table 6, one might conclude that there is a missing weekend (22 June) to weekday (23/24 June) variation in BC emissions within EA8-10. However, Fig. 13 shows that the 22 June observations only weakly reduce uncertainty in emissions.

In a more tangible application,  $\rho$  can be used to assess existing and future observing strategies in a similar way to how  
 30 Yang et al. (2014) used adjoint sensitivity information to plan future meteorological observing sites to improve forecasts of extreme dust events in the Korean peninsula. Fig. 13 presents anthropogenic  $\rho$  for different combinations of surface and aircraft



observations on 23/24 June. The surface observations primarily resolve sources near Fresno, and to a lesser extent near Los Angeles. Since the purpose of the IMPROVE network is to measure background concentrations, it is mostly successful on 23 June in not being influenced by anthropogenic sources of BC from the major cities. If the goal were to measure anthropogenic sources, inflows, or domain-wide concentrations on daily time scales, then  $\rho$  would suggest using a different surface network distribution. Such a conclusion does not conflict with the success of using IMPROVE observations to provide top-down constraints on both BB and anthropogenic emissions on monthly time scales (e.g., Mao et al., 2015). That strategy is consistent with what is generally known: further decreasing uncertainty requires observing the same phenomena more thoroughly. For hourly to daily time scales, more observations are needed close to and downwind of chemical sources, and at high spatial and temporal resolution (e.g., from repeated aircraft overpasses, extra aircraft, hourly-average surface sites, or satellites).

Another piece of information useful for comparing observing configurations and inversion scenarios is the trace of the resolution matrix, or degrees of freedom for signal, i.e.,

$$\text{DOF} = \text{Tr} \left[ \mathbf{I}_n - \mathbf{A} \mathbf{P}^a \mathbf{B}^{-1} \right], \quad (33)$$

which is equal to the number of modes of variability in the emissions that are resolved by the observations (Wahba, 1985; Purser and Huang, 1993; Rodgers, 1996). Substituting the approximation for  $\mathbf{A} \mathbf{P}^a$  from Eq. 29,

$$\begin{aligned} \text{DOF} &\approx n - \text{Tr} \left[ \left( \mathbf{B} + \mathbf{U} \left( \sum_{k_i=1}^l (\lambda_{k_i}^{-1} - 1) \hat{\mathbf{v}}_{k_i} \hat{\mathbf{v}}_{k_i}^{\top} \right) \mathbf{U}^{\top} \right) \mathbf{B}^{-1} \right] \\ &\approx - \text{Tr} \left[ \mathbf{U} \left( \sum_{k_i=1}^l (\lambda_{k_i}^{-1} - 1) \hat{\mathbf{v}}_{k_i} \hat{\mathbf{v}}_{k_i}^{\top} \right) \mathbf{U}^{\top} \mathbf{B}^{-1} \right]. \end{aligned} \quad (34)$$

Since  $\mathbf{U}$  is square,  $\mathbf{U}^{\top} \mathbf{B}^{-1} \mathbf{U} = \mathbf{I}_n$ , and  $\text{Tr} [\hat{\mathbf{v}}_{k_i} \hat{\mathbf{v}}_{k_i}^{\top}] = \hat{\mathbf{v}}_{k_i}^{\top} \hat{\mathbf{v}}_{k_i} = 1$ , the expression simplifies as

$$\begin{aligned} \text{DOF} &= - \text{Tr} \left[ \left( \sum_{k_i=1}^l (\lambda_{k_i}^{-1} - 1) \hat{\mathbf{v}}_{k_i} \hat{\mathbf{v}}_{k_i}^{\top} \right) \mathbf{U}^{\top} \mathbf{B}^{-1} \mathbf{U} \right] \\ &\approx \sum_{k_i=1}^l (1 - \lambda_{k_i}^{-1}) \text{Tr} [\hat{\mathbf{v}}_{k_i} \hat{\mathbf{v}}_{k_i}^{\top}] \\ &\approx \sum_{k_i=1}^l (1 - \lambda_{k_i}^{-1}). \end{aligned} \quad (35)$$

Therefore, the only information needed to compute DOF are the eigenvalues of  $\mathbf{T}_l$ . Each inner loop,  $k_i$ , has the potential for constraining one additional mode of variability in the emission scaling factors. For all of our inversion scenarios, the leading eigenvalue is on the order of  $10^2 - 10^3$ , which is equal to the condition number of the full-rank Hessian. As the Lanczos optimization proceeds, each subsequent  $\lambda_{k_i}$  is smaller, asymptotically approaching unity, and each eigenmode provides less information than the one preceding it about scaling factor variability.

Figure 14 gives three estimates of DOF at each level of truncation in the final outer loop, that is if higher degrees of eigenvalues were ignored. In that figure, we plot eigenvalue spectra of the FINN\_STD and QFED\_STD scenarios on 22 June.

Similar to  $\rho$ , we use a 50 iteration linear optimization to improve the bounds on DOF. The  $k_i = l$  estimate of the eigenvalue spectrum at each iteration is represented by a single colored line. Each member of the eigenvalue spectrum, represented by vertical grid lines in Fig. 14, converges toward an upper bound as more iterations are taken. Initial guesses for the least dominant eigenvalues are less than 1 for  $k_i \geq 8$  for FINN\_STD, but they exceed 1 after an additional iteration, consistent with the properties of the Lanczos sequence. The first DOF in parentheses adheres to the philosophy that only converged eigenvalues should be used to estimate DOF; it excludes  $\lambda_{k_i}, \dots, \lambda_l$  such that  $\lambda_{k_i}$  is more than 5% changed from the previous estimate. The second DOF in parentheses uses all of the current estimates of the eigenvalues available in iteration  $l$ . This is still a conservative estimate of DOF, because the true eigenvalues of the full-rank  $\mathbf{T}_n$  are always larger than their current numerical estimate. After enough iterations, the numerical growth in DOF is very small, and further computation is not warranted. As the eigenvalue spectra in Figure 14 and the cost function reduction in Figure 3 show, this is long after the cost function is converged enough for practical purposes. The posterior CVs, which are the primary result from inverse modeling, do not change significantly in the final outer loop. Finally, the best estimates of DOF in red brackets are evaluated at different truncations using the most-converged values of the eigenvalues found in the 22<sup>nd</sup> iteration.

Similar to  $\rho$ , the quantitative application of DOF is limited to the final outer loop, when  $\delta \mathbf{x}^n$  is small enough that  $(\mathcal{H}_{\delta v})^{-1}|_{x^{n-1}} \approx (\mathcal{H}_{\delta v})^{-1}|_{x^n}$ . Absent the need to estimate the posterior Hessian, the outer loop could be ended an iteration earlier. In the inner loop, truncated estimates of  $\mathcal{H}^{-1}$  and its eigenvalue spectrum at earlier iterations will provide conservative values for both DOF and  $\rho$ . The actual DOF is higher than any value shown in Figs. 14 (22 June) and 15 (23/24 June). Therefore, the 22 June observations constrain  $>14$  modes of hourly grid-scale variability through 4D-Var in both the FINN\_STD and QFED\_STD scenarios. Just like for  $\rho$ , the optimization constrains additional modes in the earlier outer loop iterations, but that quantification is not straightforward since DOF is defined for linear behavior. If all outer loops were similar, then the total DOF for the entire nonlinear optimization is on the order of 30 to 40.

As shown in Fig. 15, the DOF on 23 and 24 June after 50 iterations are 10, 17, and 23 for the SURF, ACFT, and FINN\_STD(23/24) scenarios, respectively. The relative magnitudes show that using combined surface and aircraft observations provides an additional value over using either independently, although the two platforms might have some redundancy. This conclusion is consistent with the maps of BB and anthropogenic  $\rho$  in Fig. 13, where the footprints of SURF and ACFT have slight overlap near Los Angeles, but are otherwise independent. Additionally, the higher DOF of ACFT is consistent with its more widespread and larger magnitude  $\rho$  values. The slower eigenvalue convergence when both observing types are utilized means that additional inner iterations could yield higher estimates for DOF in that case. What is even more clear, and intuitive, is that  $\rho$  and DOF estimates require more iterations as the number of constrained CVs increases, which is directly dependent on the number of observations. ~~What might be of particular interest to future measurement planning is that daily average surface data can provide a useful constraint when captured near sources on the same day as the emission event, which is supported by the~~ The sparse  $\rho$  map for SURF in Fig. 13, and the large spike near Fresno illustrate that while near-source surface measurements can be a powerful constraint, measurements of background concentrations provide relatively little constraints to characterize CA anthropogenic emissions on 1-day time scales.

### 3.5 Cross Validation

As an additional evaluation of the robustness of the emission scaling factors, we apply them in cross validation tests. In two separate evaluations, the 22 June scaling factors are applied to 23-26 June emissions, and the 23/24 scaling factors are applied to 25-26 June emissions. ~~Even before carrying out such a test, the~~ The heterogeneous adjoint sensitivity signs and magnitudes for each source sector we found on each day of the campaign (Guerrette and Henze, 2015) are an indication that corrective scaling factors in each day will be unique. In that work, we found that the 24 June observations were most sensitive to Southern California anthropogenic sources on 24 June and to Northern and Southern California coastal sources of both sectors on 23 June. The 26 June observations were most sensitive to Northern California fires, and the adjoint sensitivities were of opposite sign than on 23 and 24 June.

As shown in Fig. 4, the cross validated 22 June scaling factors rarely generate improvements to model performance, when compared to 24 and 26 June aircraft observations. On 24 June, some of the high bias predictions are corrected, or even over-compensated, but the low bias prior locations are unaffected. Table 2 shows the  $R^2$  and slope of the linear trend lines. The scatter of the fit for QFED\_STD on 24 June and the slope for FINN\_STD on 26 June are slightly improved, but all other metrics degrade. The increase in slope for FINN\_STD comes as a result of better fit to very large concentrations above the PBL associated with fire sources on multiple previous days. The posterior scaling factors generated from the 23/24 June inversion degrade the forecast of aircraft measurements on 26 June. Since the posterior primarily serves to reduce coastal anthropogenic and BB emissions, it is not surprising that it does not improve a low bias prior two days later.

Table 3 includes cross-validated surface measurements on 23 June and 26 June. There is very little change to the modeled surface concentrations as a result of posterior scaling factors ~~in any~~ derived from inversions that only use aircraft observations. Assimilating surface observations on 23 June (Monday) does improve model comparisons to surface observations on 26 June (Thursday). Those small improvements imply that errors are weakly correlated between weekdays. Although it is beyond the information content provided by the observations used in this work, future studies could compare the efficacy of using weak multiday correlation in **B** and the hard constraint of 24 h periodic scaling factors used herein.

~~Given the differing flight tracks on multiple days, the cross-validation results demonstrate the need to repeat observations of similar phenomena. Such a strategy could help eliminate non-emission related sources of uncertainty, and further characterize temporal heterogeneity of inventory errors.~~ Aircraft and surface observations do not appear to be useful for cross-validation of each other over the short timescales and limited set of flights considered here. At least for this study period, when they are not collocated, each provides some unique information to the inversion. ~~Cross-validation might be more successful when using measurements collected over a broader range of prior error behaviors or by considering a less complex problem than California statewide BB emissions.~~

## 4 Conclusions and future work

We have presented the implementation and an application of incremental chemical 4D-Var using an atmospheric chemistry model with online meteorology in WRFDA-Chem. This work expands on our previous efforts to develop the ADM and TLM

in WRFPLUS-Chem (Guerrette and Henze, 2015). This new inversion tool takes advantage of previous developments of meteorological data assimilation in WRFDA (Barker et al., 2005; Huang et al., 2009). That same framework is applied to ~~lognormally~~ log-normally distributed emission scaling factors through an exponential transform. We utilize the square root preconditioner for a CVT using horizontal and temporal scaling factor correlations. The Lanczos linear optimization algorithm in the inner loop allows for estimation of posterior error and DOF for objectively evaluating observing systems. Outer loop convergence is improved with a heuristic DGN multiplier, which allows the incremental ~~4D-Var~~ framework to handle the nonlinearity of the ~~lognormal~~ log-normal cost function. While the optimizations herein focus exclusively on emissions, which are known to be important drivers of model uncertainty in BC estimates (e.g., Fu et al., 2012; Zhang et al., 2014a), other factors such as meteorology, plume rise and deposition mechanisms may also affect the model's predictions of BC concentrations.

When applied to the ARCTAS-CARB campaign period, it is not clear which prior emissions perform better. If assessment by initial cost function value alone were meaningful, FINNv1.0 performs best. However, that could be due to FINNv1.0 being biased low combined with the assumption of Gaussian distributed model-observation errors. Positive residuals are weighted higher than negative ones, even when relative errors are equal. There could be some improvement to the posterior emissions by implementing the incremental log-normal ~~cost function framework derived by Fletcher and Jones (2014)~~ methods of Fletcher and Jones (2014) or Song et al. (2016). If the purpose of the inventory is to provide air quality warnings to the major California cities, then FINNv1.0, FINNv1.5, and QFEDv2.4r8 all have some built-in high bias that will err on the side of caution. Their inability to reproduce high concentrations near sources either points to a deficiency in the inventories, vertical mixing processes, or the temporal observation averaging procedure followed herein, diagnosis of which would require measurements of plume injection heights and widths. The relative magnitudes of grid-scale fire and anthropogenic emissions make it difficult to simultaneously constrain them without additional information. More work should be done to improve both bottom-up and top-down estimates of anthropogenic emissions outside of fire events. We also agree with Mao et al. (2015), who recommended multi-species inversions (e.g., BC and CO) to discern specific source sectors.

Through the setup and application of the 4D-Var system, we gained valuable knowledge to guide future modeling and measurement efforts. We found two errors in the diurnal distribution of BB emissions and identified a scaling necessary to apply QFED to the western U.S. Additionally, the highly ~~heterogenous~~ heterogeneous posterior scaling factors during ARCTAS-CARB raise questions that the limited BB observations during that time period do not answer. (1) Are BB emission errors always heterogeneous, or only during a transient initiation stage like that observed in June 2008? If heterogeneity is consistent outside initiation events, then inversions should apply weaker inter-day correlation than the hard constraint used herein or have independent scaling factors for each day. (2) Are the temporally bimodal posterior emissions realistic, or are they an artifact of the correlation timescale used? (3) Are the BB plume heights reasonable, and should they follow a diurnal pattern? The current 1D plume rise mechanism in WRF-Chem depends strongly on specified burned areas, which are diurnally invariant and highly uncertain (e.g., Boschetti et al., 2004). The last two questions indicate there is value in continuous night (between 20:00 and 06:00 LT) and day measurements of the same fire region. Since models poorly predict shallow boundary layers, the use of night time observations in 4D-Var would require characterization and subsequent model tuning of those vertical mixing processes. Furthermore, if it is accepted that high-resolution models are required to accurately predict degraded air quality events, then

high spatial and/or temporal resolution concentration measurements from research campaigns or geostationary satellites are necessary to provide the sufficient constraints on inventory errors. The error reduction estimation method provided herein will be useful for planning these future missions.

Future applications of the WRFDA-Chem system developed here may consider improvements such as the following. One possible way to reduce model uncertainty would be to extend the multi-incremental 4D-Var available in WRFDA (Zhang et al., 2014b) to the new scaling factor CVs. Multi-incremental chemical 4D-Var would use a high-resolution model forecast to generate trajectory checkpoint files (see Guerrette and Henze (2015)), and could take advantage of improvements to chemical transport at higher resolution realized by using online meteorology demonstrated by Grell et al. (2004) and Grell and Baklanov (2011). In addition, FDDA nudging has been shown to improve wind fields and was used successfully in an LPDM emission inversion (Lauvaux et al., 2016). Even after exhausting methods to improve the posterior, the error contributions from hard-coded descriptions of meteorology can be bounded using ensemble and sensitivity tests (e.g., Angevine et al., 2014; Lauvaux et al., 2016).

## Appendix A: Relating DA and optimization formulations

The linear optimization in the inner loop solves a system

$$\begin{aligned} \min_{\hat{\mathbf{x}}} F(\hat{\mathbf{x}}) &= \frac{1}{2} \hat{\mathbf{x}}^\top \mathbf{A}' \hat{\mathbf{x}} - \hat{\mathbf{x}}^\top \mathbf{b} + c \\ \mathbf{A}' \hat{\mathbf{x}} &= \mathbf{b}. \end{aligned} \tag{A1}$$

In our case,  $\hat{\mathbf{x}} \equiv \delta \mathbf{v}^k$ . The equivalence of Eq. 7 and Eq. A1 is apparent in Tshimanga et al. (2008), who provide a notational translation between publications on DA and those on minimization algorithms and preconditioners. We repeat their translation to account for the differences in formulation of Eq. 7 and Eq. 5 in Tshimanga et al. (2008).

The process starts by considering Lawless et al. (2005) and Gratton et al. (2007), who show that incremental 4D-Var is equivalent to a truncated Gauss-Newton (TGN) optimization algorithm. The incremental 4D-Var cost function is condensed to:

$$\min_{\delta \mathbf{v}} J(\delta \mathbf{v}) = \frac{1}{2} \mathbf{f}(\delta \mathbf{v})^\top \mathbf{f}(\delta \mathbf{v}), \tag{A2}$$

where

$$\mathbf{f}(\delta \mathbf{v}^k) \equiv \begin{pmatrix} \delta \mathbf{v}^k - \mathbf{d}^{b,k-1} \\ \mathbf{R}^{-\frac{1}{2}} (\mathbf{G}^{k-1} \mathbf{U} \delta \mathbf{v}^k - \mathbf{d}^{o,k-1}) \end{pmatrix}. \tag{A3}$$

This definition of  $\mathbf{f}$  is what enables incremental 4D-Var to be characterized as TGN. The remainder of the derivation amounts to substitutions. GN approximates Newton's method in each quadratic minimization problem,  $k$ , to solve for the increment  $\delta \mathbf{v}^k$  in the linearized system

$$\mathcal{H}_{\delta \mathbf{v}} \delta \mathbf{v}^k = -\nabla J. \tag{A4}$$

This form is equivalent to multiplying Eq. 10 by the Hessian on both sides. In our case, the right-hand side is  $\mathbf{b} \equiv -\nabla J = -\mathbf{F}^{k-1\top} \mathbf{f}(\delta \mathbf{v}^{k-1})$ , where

$$\mathbf{f}(\delta \mathbf{v}^{k-1}) \equiv - \begin{pmatrix} \mathbf{d}^{b,k-1} \\ \mathbf{R}^{-\frac{1}{2}} \mathbf{d}^{o,k-1} \end{pmatrix}, \quad (\text{A5})$$

and

$$5 \quad \mathbf{F}^{k-1} \equiv \nabla_{\delta \mathbf{v}^{k-1}} \mathbf{f}|_{\delta \mathbf{v}^{k-1}} = \begin{pmatrix} \mathbf{I}_n \\ \mathbf{R}^{-\frac{1}{2}} \mathbf{G}^{k-1} \mathbf{U} \end{pmatrix}. \quad (\text{A6})$$

$\mathbf{f}(\delta \mathbf{v}^{k-1})$  and its Jacobian are fixed for each outer loop by the  $k-1$  trajectory. Completing the GN algorithm, the Hessian ( $\mathcal{H}_{\delta \mathbf{v}}$ ) is approximated by  $\mathbf{A}' \equiv \mathbf{F}^{k-1\top} \mathbf{F}^{k-1}$ , after ignoring mixed partial derivatives of  $\mathbf{f}$ . The Hessian of Eq. A2 matches that of Eq. 7, namely

$$\mathcal{H}_{\delta \mathbf{v}} = \mathbf{I}_n + \mathbf{U}^\top \mathbf{G}^{k-1\top} \mathbf{R}^{-1} \mathbf{G}^{k-1} \mathbf{U}. \quad (\text{A7})$$

10 After substitutions, Eq. A4 becomes

$$\mathbf{F}^{k-1\top} \mathbf{F}^{k-1} \delta \mathbf{v}^k = -\mathbf{F}^{k-1\top} \mathbf{f}(\delta \mathbf{v}^{k-1}), \quad (\text{A8})$$

which expands to

$$\left( \mathbf{I}_n + \mathbf{U}^\top \mathbf{G}^{k-1\top} \mathbf{R}^{-1} \mathbf{G}^{k-1} \mathbf{U} \right) \delta \mathbf{v}^k = \mathbf{d}^{b,k-1} + \mathbf{U}^\top \mathbf{G}^{k-1\top} \mathbf{R}^{-1} \mathbf{d}^{o,k-1}. \quad (\text{A9})$$

Solving for  $\delta \mathbf{v}^k$  gives the same update formula that would result from setting Eq. 9 equal to zero,

$$15 \quad \delta \mathbf{v}^k = \left( \mathbf{I}_n + \mathbf{U}^\top \mathbf{G}^{k-1\top} \mathbf{R}^{-1} \mathbf{G}^{k-1} \mathbf{U} \right)^{-1} \left( \mathbf{d}^{b,k-1} + \mathbf{U}^\top \mathbf{G}^{k-1\top} \mathbf{R}^{-1} \mathbf{d}^{o,k-1} \right). \quad (\text{A10})$$

Thus, by defining  $\mathbf{f}$  appropriately, the equivalence between GN and incremental 4D-Var is verified.

## Appendix B: Derivation of the truncated inverse Hessian

After  $l$  inner iterations, the Lanczos vectors form an orthogonal matrix,  $\mathbf{Q}_l = [\hat{\mathbf{q}}_1, \dots, \hat{\mathbf{q}}_l]$ , which satisfies

$$\mathcal{H}_{\delta \mathbf{v}} \mathbf{Q}_l = \mathbf{Q}_l \mathbf{T}_l. \quad (\text{B1})$$

20 The extremal eigenvalues of  $\mathbf{T}_l$  are good approximations to  $\mathcal{H}_{\delta \mathbf{v}}$ 's extremal eigenvalues (Golub and Van Loan, 1996).  $\mathbf{T}_l$  can be decomposed as

$$\mathbf{T}_l = \mathbf{W}_l \mathbf{\Lambda}_l \mathbf{W}_l^{-1}. \quad (\text{B2})$$

If we were to carry out the minimization for  $n$  steps, we would find all the Lanczos vectors, and would be able to construct the full  $\mathbf{T}$  and  $\mathbf{Q}$  matrices. In that case, the orthogonal Lanczos vectors admit  $\mathbf{Q}\mathbf{Q}^\top = \mathbf{I}$ . When combined with Eq. B1,

$$\mathcal{H}_{\delta\mathbf{v}} = \mathbf{Q}\mathbf{W}\mathbf{\Lambda}\mathbf{W}^{-1}\mathbf{Q}^\top \quad (\text{B3})$$

Because the eigenvectors are orthonormal,

$$5 \quad \mathcal{H}_{\delta\mathbf{v}} = (\mathbf{Q}\mathbf{W})\mathbf{\Lambda}(\mathbf{Q}\mathbf{W})^\top. \quad (\text{B4})$$

Thus, the eigenvectors of  $\mathcal{H}_{\delta\mathbf{v}}$  are approximately equal to the normalized eigenvectors of  $\mathbf{T}$ , premultiplied by the matrix of Lanczos vectors, i.e.,

$$\mathcal{H}_{\delta\mathbf{v}} = \hat{\mathbf{v}}\mathbf{\Lambda}\hat{\mathbf{v}}^\top, \quad (\text{B5})$$

where the  $k_i^{\text{th}}$  eigenvector of  $\mathcal{H}_{\delta\mathbf{v}}$  is

$$10 \quad \hat{\mathbf{v}}_{k_i} = \mathbf{Q}\hat{\mathbf{w}}_{k_i}. \quad (\text{B6})$$

The Hessian is constructed by

$$\mathcal{H}_{\delta\mathbf{v}} = \hat{\mathbf{v}}\mathbf{\Lambda}\hat{\mathbf{v}}^\top = \sum_{k_i=1}^n \lambda_{k_i} \hat{\mathbf{v}}_{k_i} \hat{\mathbf{v}}_{k_i}^\top. \quad (\text{B7})$$

Since the Hessian and its inverse have identical eigenvectors and reciprocal eigenvalues, the inverse is

$$[\mathcal{H}_{\delta\mathbf{v}}]^{-1} = \sum_{k_i=1}^n \lambda_{k_i}^{-1} \hat{\mathbf{v}}_{k_i} \hat{\mathbf{v}}_{k_i}^\top. \quad (\text{B8})$$

15 Although this expression is usable, computational resource limitations require  $l \ll n$ . Truncating the sum yields a low rank estimate for the inverse, and for the posterior error which it estimates.

A more robust estimate of the posterior error is a low-rank update to the full-rank prior covariance,  $\mathbf{B}$ . To pursue that goal, first we return to the linear algebra formula, then add and subtract the identity matrix to get

$$\begin{aligned} \mathcal{H}_{\delta\mathbf{v}} &= \mathbf{I} + \hat{\mathbf{v}}\mathbf{\Lambda}\hat{\mathbf{v}}^\top - \mathbf{I} \\ &= \mathbf{I} + \hat{\mathbf{v}}\mathbf{\Lambda}\hat{\mathbf{v}}^\top - \hat{\mathbf{v}}\mathbf{I}\hat{\mathbf{v}}^\top \\ &= \mathbf{I} + \sum_{k_i=1}^n (\lambda_{k_i} - 1) \hat{\mathbf{v}}_{k_i} \hat{\mathbf{v}}_{k_i}^\top \end{aligned} \quad (\text{B9})$$

20 Now we repeat the truncation,

$$\mathcal{H}_{\delta\mathbf{v}} \approx \mathbf{I} + \sum_{k_i=1}^l (\lambda_{k_i} - 1) \hat{\mathbf{v}}_{k_i} \hat{\mathbf{v}}_{k_i}^\top, \quad (\text{B10})$$

where  $\hat{\boldsymbol{v}}_{k_i}$  is constructed from the partial set of Lanczos vectors as

$$\hat{\boldsymbol{v}}_{k_i} = \mathbf{Q}_l \hat{\boldsymbol{w}}_{lk_i}. \quad (\text{B11})$$

Next we apply the Sherman-Morrison formula to recursively build the inverse for each term in the sum. Throughout, we will take advantage of the following two relationships for orthogonal vectors

$$\hat{\boldsymbol{v}}_j^\top \hat{\boldsymbol{v}}_j = 1$$

and

$$5 \quad \hat{\boldsymbol{v}}_j^\top \hat{\boldsymbol{v}}_i = 0; \quad j \neq i.$$

Starting with the first term,

$$\begin{aligned} \mathbf{N}_1^{-1} &= [\mathbf{I} + (\lambda_1 - 1) \hat{\boldsymbol{v}}_1 \hat{\boldsymbol{v}}_1^\top]^{-1} \\ &= \mathbf{I}^{-1} - \frac{\mathbf{I}^{-1} (\lambda_1 - 1) \hat{\boldsymbol{v}}_1 \hat{\boldsymbol{v}}_1^\top \mathbf{I}^{-1}}{1 + (\lambda_1 - 1) \hat{\boldsymbol{v}}_1^\top \mathbf{I}^{-1} \hat{\boldsymbol{v}}_1} \\ &= \mathbf{I} - \frac{(\lambda_1 - 1) \hat{\boldsymbol{v}}_1 \hat{\boldsymbol{v}}_1^\top}{\lambda_1} \\ &= \mathbf{I} + (\lambda_1^{-1} - 1) \hat{\boldsymbol{v}}_1 \hat{\boldsymbol{v}}_1^\top. \end{aligned}$$

This result fits our desired proof. Now for the second term,

$$\begin{aligned} \mathbf{N}_2^{-1} &= \{\mathbf{N}_1 + (\lambda_2 - 1) \hat{\boldsymbol{v}}_2 \hat{\boldsymbol{v}}_2^\top\}^{-1} \\ &= \mathbf{N}_1^{-1} - \frac{\mathbf{N}_1^{-1} (\lambda_2 - 1) \hat{\boldsymbol{v}}_2 \hat{\boldsymbol{v}}_2^\top \mathbf{N}_1^{-1}}{1 + (\lambda_2 - 1) \hat{\boldsymbol{v}}_2^\top \mathbf{N}_1^{-1} \hat{\boldsymbol{v}}_2} \\ &= \mathbf{I} + (\lambda_1^{-1} - 1) \hat{\boldsymbol{v}}_1 \hat{\boldsymbol{v}}_1^\top - \\ &\quad \frac{[\mathbf{I} + (\lambda_1^{-1} - 1) \hat{\boldsymbol{v}}_1 \hat{\boldsymbol{v}}_1^\top] (\lambda_2 - 1) \hat{\boldsymbol{v}}_2 \hat{\boldsymbol{v}}_2^\top [\mathbf{I} + (\lambda_1^{-1} - 1) \hat{\boldsymbol{v}}_1 \hat{\boldsymbol{v}}_1^\top]}{1 + (\lambda_2 - 1) \hat{\boldsymbol{v}}_2^\top [\mathbf{I} + (\lambda_1^{-1} - 1) \hat{\boldsymbol{v}}_1 \hat{\boldsymbol{v}}_1^\top] \hat{\boldsymbol{v}}_2} \\ &= \mathbf{I} + (\lambda_1^{-1} - 1) \hat{\boldsymbol{v}}_1 \hat{\boldsymbol{v}}_1^\top + (\lambda_2^{-1} - 1) \hat{\boldsymbol{v}}_2 \hat{\boldsymbol{v}}_2^\top. \end{aligned}$$

- 10 The dot products of orthogonal vectors cancels all terms in the numerator and denominator except the ones multiplied by the identity matrix. The same simplification applies to each additional sum, where the full sum can be expressed as

$$\begin{aligned} \mathbf{N}_l^{-1} &= \mathbf{I} + (\lambda_1^{-1} - 1) \hat{\boldsymbol{v}}_1 \hat{\boldsymbol{v}}_1^\top - \\ &\quad \sum_{k_i=2}^l \frac{[\mathbf{I} + \sum_{r=1}^{k_i-1} (\lambda_r^{-1} - 1) \hat{\boldsymbol{v}}_r \hat{\boldsymbol{v}}_r^\top] (\lambda_{k_i} - 1) \hat{\boldsymbol{v}}_{k_i} \hat{\boldsymbol{v}}_{k_i}^\top [\mathbf{I} + \sum_{r=1}^{k_i-1} (\lambda_r^{-1} - 1) \hat{\boldsymbol{v}}_r \hat{\boldsymbol{v}}_r^\top]}{1 + (\lambda_{k_i} - 1) \hat{\boldsymbol{v}}_{k_i}^\top [\mathbf{I} + \sum_{r=1}^{k_i-1} (\lambda_r^{-1} - 1) \hat{\boldsymbol{v}}_r \hat{\boldsymbol{v}}_r^\top] \hat{\boldsymbol{v}}_{k_i}} \end{aligned}$$

Here, again, all of the terms where  $r \neq k_i$  cancel. What remains is similar to Eq. B8, but slightly modified.

$$[\mathcal{H}_{\delta \mathbf{v}}]^{-1} \approx \mathbf{I} + \sum_{k_i=1}^l (\lambda_{k_i}^{-1} - 1) \hat{\boldsymbol{v}}_{k_i} \hat{\boldsymbol{v}}_{k_i}^\top. \quad (\text{B12})$$



After a left-side multiplication by  $\mathbf{U}$  and a right-side multiplication by  $\mathbf{U}^\top$ , we achieve the desired low rank update to  $\mathbf{B}$  found in Eq. 29.

*Author contributions.* J. J. Guerrette developed the software and ran simulations following the guidance of the PI, D. K. Henze. Both authors contributed to writing and analysis.

5 *Acknowledgements.* [Thank you to two anonymous referees for their constructive and helpful comments that strengthened this work.](#) This research has been supported by a grant from the U.S. Environmental Protection Agency’s Science to Achieve Results (STAR) program. Although the research described in the article has been funded wholly or in part by the U.S. Environmental Protection Agency’s STAR program through grant R835037, it has not been subjected to any EPA review and therefore does not necessarily reflect the views of the Agency, and no official endorsement should be inferred. In addition, this paper is a result of research funded by the National Oceanic  
10 and Atmospheric Administration’s Earth System Research Laboratory as part of the Fire Influence on Regional and Global Environments Experiment (FIREX) through the grant NOAA NA16OAR4310113. We are thankful for the ARCTAS mission, which was supported by NASA. We thank Y. Kondo for making the SP2 observations available through the NASA LaRC Airborne Science Data for Atmospheric Composition database. We acknowledge the use of FIRMS data from the Land Atmosphere Near-real time Capability for EOS (LANCE) system operated by the NASA/GSFC/Earth Science Data and Information System (ESDIS) with funding provided by NASA/HQ.

## References

- Andela, N., Kaiser, J. W., van der Werf, G. R., and Wooster, M. J.: New fire diurnal cycle characterizations to improve fire radiative energy assessments made from MODIS observations, *Atmospheric Chemistry and Physics*, 15, 8831–8846, doi:10.5194/acp-15-8831-2015, <http://www.atmos-chem-phys.net/15/8831/2015/>, 2015.
- 5 Angevine, W. M., Eddington, L., Durkee, K., Fairall, C., Bianco, L., and Brioude, J.: Meteorological Model Evaluation for CalNex 2010, *Monthly Weather Review*, 140, 3885–3906, doi:10.1175/MWR-D-12-00042.1, <http://journals.ametsoc.org/doi/abs/10.1175/MWR-D-12-00042.1>, 2012.
- Angevine, W. M., Brioude, J., McKeen, S., and Holloway, J. S.: Uncertainty in Lagrangian pollutant transport simulations due to meteorological uncertainty from a mesoscale WRF ensemble, *Geoscientific Model Development*, 7, 2817–2829, doi:10.5194/gmd-7-2817-2014, <http://www.geosci-model-dev.net/7/2817/2014/>, 2014.
- 10 Barker, D., Lee, M.-S., Guo, Y.-R., Huang, W., Huang, H., and Rizvi, Q.: WRF-Var - A unified 3/4D-Var variational data assimilation system for WRF, in: Sixth WRF/15th MM5 Users' Workshop, p. 17, Boulder, CO, NCAR, <http://www2.mmm.ucar.edu/wrf/users/workshops/WS2005/presentations/session10/1-Barker.pdf>, 2005.
- Barker, D. M., Huang, W., Guo, Y.-R., Bourgeois, A. J., and Xiao, Q. N.: A three-dimensional variational data assimilation system for MM5: Implementation and initial results, *Monthly Weather Review*, 132, 897–914, [http://journals.ametsoc.org/doi/abs/10.1175/1520-0493\(2004\)132%3C0897:ATVDAS%3E2.0.CO;2](http://journals.ametsoc.org/doi/abs/10.1175/1520-0493(2004)132%3C0897:ATVDAS%3E2.0.CO;2), 2004.
- 15 Bergamaschi, P., Frankenberg, C., Meirink, J. F., Krol, M., Villani, M. G., Houweling, S., Dentener, F., Dlugokencky, E. J., Miller, J. B., Gatti, L. V., Engel, A., and Levin, I.: Inverse modeling of global and regional CH<sub>4</sub> emissions using SCIAMACHY satellite retrievals, *Journal of Geophysical Research*, 114, 1–28, doi:10.1029/2009JD012287, <http://doi.wiley.com/10.1029/2009JD012287>, 2009.
- 20 Bond, T. C., Doherty, S. J., Fahey, D. W., Forster, P. M., Berntsen, T., DeAngelo, B. J., Flanner, M. G., Ghan, S., Kärcher, B., Koch, D., Kinne, S., Kondo, Y., Quinn, P. K., Sarofim, M. C., Schultz, M. G., Schulz, M., Venkataraman, C., Zhang, H., Zhang, S., Bellouin, N., Guttikunda, S. K., Hopke, P. K., Jacobson, M. Z., Kaiser, J. W., Klimont, Z., Lohmann, U., Schwarz, J. P., Shindell, D., Storelvmo, T., Warren, S. G., and Zender, C. S.: Bounding the role of black carbon in the climate system: A scientific assessment: BLACK CARBON IN THE CLIMATE SYSTEM, *Journal of Geophysical Research: Atmospheres*, 118, 5380–5552, doi:10.1002/jgrd.50171, <http://doi.wiley.com/10.1002/jgrd.50171>, 2013.
- 25 Boschetti, L., Eva, H. D., Brivio, P. A., and Grégoire, J. M.: Lessons to be learned from the comparison of three satellite-derived biomass burning products, *Geophysical Research Letters*, 31, n/a–n/a, doi:10.1029/2004GL021229, <http://dx.doi.org/10.1029/2004GL021229>, 2004.
- Brioude, J., Angevine, W. M., Ahmadov, R., Kim, S.-W., Evan, S., McKeen, S. A., Hsie, E.-Y., Frost, G. J., Neuman, J. A., and Pollack, I. B.: Top-down estimate of surface flux in the Los Angeles Basin using a mesoscale inverse modeling technique: assessing anthropogenic emissions of CO, NO<sub>x</sub> and CO<sub>2</sub> and their impacts, *Atmospheric Chemistry and Physics Discussions*, 12, 31439–31481, <http://www.atmos-chem-phys-discuss.net/12/31439/2012/>, 2012.
- 30 Chen, Y. and Oliver, D. S.: Levenberg–Marquardt forms of the iterative ensemble smoother for efficient history matching and uncertainty quantification, *Computational Geosciences*, 17, 689–703, doi:10.1007/s10596-013-9351-5, <http://link.springer.com/10.1007/s10596-013-9351-5>, 2013.
- 35 Courtier, P., Thépaut, J.-N., and Hollingsworth, A.: A strategy for operational implementation of 4D-Var, using an incremental approach, *Quarterly Journal of the Royal Meteorological Society*, 120, 1367–1387, doi:10.1002/qj.49712051912, <http://dx.doi.org/10.1002/qj.49712051912>, 1994.

- Cui, Y. Y., Brioude, J., McKeen, S. A., Angevine, W. M., Kim, S.-W., Frost, G. J., Ahmadov, R., Peischl, J., Bousserez, N., Liu, Z., Ryerson, T. B., Wofsy, S. C., Santoni, G. W., Kort, E. A., Fischer, M. L., and Trainer, M.: Top-down estimate of methane emissions in California using a mesoscale inverse modeling technique: The South Coast Air Basin: Inverse Estimate of Methane Emissions, *Journal of Geophysical Research: Atmospheres*, 120, 6698–6711, doi:10.1002/2014JD023002, <http://doi.wiley.com/10.1002/2014JD023002>, 2015.
- 5 Darnenov, A. S. and da Silva, A.: The Quick Fire Emissions Dataset (QFED)—Documentation of versions 2.1, 2.2, and 2.4, Tech. Rep. NASA TM-2013-104606/Vol 32, NASA, <http://gmao.gsfc.nasa.gov/pubs/tm/>, 2013.
- Elbern, H., Strunk, A., Schmidt, H., and Talagrand, O.: Emission rate and chemical state estimation by 4-dimensional variational inversion, *Atmospheric Chemistry and Physics*, 7, 3749–3769, <http://www.atmos-chem-phys.net/7/3749/>, 2007.
- Fisher, M. and Courtier, P.: Estimating the covariance matrices of analysis and forecast error in variational data assimilation, Tech. Rep. Technical Memorandum 220, European Centre for Medium-Range Weather Forecasts, 1995.
- 10 Fletcher, S. J. and Jones, A. S.: Multiplicative and Additive Incremental Variational Data Assimilation for Mixed Lognormal–Gaussian Errors, *Monthly Weather Review*, 142, 2521–2544, doi:10.1175/MWR-D-13-00136.1, <http://journals.ametsoc.org/doi/abs/10.1175/MWR-D-13-00136.1>, 2014.
- Fletcher, S. J. and Zupanski, M.: Implications and impacts of transforming lognormal variables into normal variables in VAR, *Meteorologische Zeitschrift*, 16, 755–765, <http://www.ingentaconnect.com/content/schweiz/mz/2007/00000016/00000006/art00016>, 2007.
- 15 Freitas, S. R., Longo, K. M., Chatfield, R., Latham, D., Silva Dias, M. A. F., Andreae, M. O., Prins, E., Santos, J. C., Gielow, R., and Carvalho Jr, J. A.: Including the sub-grid scale plume rise of vegetation fires in low resolution atmospheric transport models, *Atmospheric Chemistry and Physics*, 7, 3385–3398, <http://www.atmos-chem-phys.net/7/3385/2007/acp-7-3385-2007.html>, 2007.
- Freitas, S. R., Longo, K. M., Trentmann, J., and Latham, D.: Technical Note: Sensitivity of 1-D smoke plume rise models to the inclusion of environmental wind drag, *Atmospheric Chemistry and Physics*, 10, 585–594, <http://www.atmos-chem-phys.net/10/585/2010/acp-10-585-2010.pdf>, 2010.
- 20 Fu, J. S., Hsu, N. C., Gao, Y., Huang, K., Li, C., Lin, N.-H., and Tsay, S.-C.: Evaluating the influences of biomass burning during 2006 BASE-ASIA: a regional chemical transport modeling, *Atmospheric Chemistry and Physics*, 12, 3837–3855, doi:10.5194/acp-12-3837-2012, <http://www.atmos-chem-phys.net/12/3837/2012/>, 2012.
- 25 Golub, G. and Van Loan, C.: *Matrix Computations*, Johns Hopkins Studies in the Mathematical Sciences, Johns Hopkins University Press, 1996.
- Gratton, S., Lawless, A. S., and Nichols, N. K.: Approximate Gauss–Newton Methods for Nonlinear Least Squares Problems, *SIAM Journal on Optimization*, 18, 106–132, doi:10.1137/050624935, <http://epubs.siam.org/doi/abs/10.1137/050624935>, 2007.
- Gratton, S., Gürol, S., and Toint, P. L.: Preconditioning and globalizing conjugate gradients in dual space for quadratically penalized nonlinear-least squares problems, *Computational Optimization and Applications*, 54, 1–25, doi:10.1007/s10589-012-9478-7, <http://link.springer.com/10.1007/s10589-012-9478-7>, 2013.
- 30 Grell, G. and Baklanov, A.: Integrated modeling for forecasting weather and air quality: A call for fully coupled approaches, *Atmospheric Environment*, 45, 6845 – 6851, doi:<http://dx.doi.org/10.1016/j.atmosenv.2011.01.017>, <http://www.sciencedirect.com/science/article/pii/S1352231011000240>, modeling of Air Quality Impacts, Forecasting and Interactions with Climate., 2011.
- 35 Grell, G., Freitas, S. R., Stuefer, M., and Fast, J.: Inclusion of biomass burning in WRF-Chem: impact of wildfires on weather forecasts, *Atmospheric Chemistry and Physics*, 11, 5289–5303, doi:10.5194/acp-11-5289-2011, <http://www.atmos-chem-phys.net/11/5289/2011/>, 2011.

- Grell, G. A., Knoche, R., Peckham, S. E., and McKeen, S. A.: Online versus offline air quality modeling on cloud-resolving scales, *Geophysical Research Letters*, 31, 1–4, doi:10.1029/2004GL020175, <http://dx.doi.org/10.1029/2004GL020175>, 2004.
- Grell, G. A., Peckham, S. E., Schmitz, R., McKeen, S. A., Frost, G., Skamarock, W. C., and Eder, B.: Fully coupled “online” chemistry within the WRF model, *Atmospheric Environment*, 39, 6957–6975, <http://www.sciencedirect.com/science/article/pii/S1352231005003560>, 5 2005.
- Grieshop, A. P., Lipsky, E. M., Pekney, N. J., Takahama, S., and Robinson, A. L.: Fine particle emission factors from vehicles in a highway tunnel: Effects of fleet composition and season, *Atmospheric Environment*, 40, Supplement 2, 287 – 298, doi:<http://dx.doi.org/10.1016/j.atmosenv.2006.03.064>, <http://www.sciencedirect.com/science/article/pii/S1352231006005796>, 2006.
- Guerrette, J. J. and Henze, D. K.: Development and application of the WRFPLUS-Chem online chemistry adjoint and WRFDA-Chem assimilation system, *Geoscientific Model Development*, 8, 1857–1876, doi:10.5194/gmd-8-1857-2015, <http://www.geosci-model-dev.net/8/1857/2015/>, 2015.
- Halliwell, L. J.: The Lognormal Random Multivariate, in: *Casualty Actuarial Society E-Forum*, Spring 2015, p. 5, Arlington, Virginia, <http://www.casact.org/pubs/forum/15spforum/Halliwell.pdf>, 2015.
- Henze, D. K., Seinfeld, J. H., and Shindell, D. T.: Inverse modeling and mapping US air quality influences of inorganic PM<sub>2.5</sub> precursor emissions using the adjoint of GEOS-Chem, *Atmospheric Chemistry and Physics*, 9, 5877–5903, doi:10.5194/acp-9-5877-2009, <http://www.atmos-chem-phys.net/9/5877/2009/>, 2009.
- Huang, X.-Y., Xiao, Q., Barker, D. M., Zhang, X., Michalakes, J., Huang, W., Henderson, T., Bray, J., Chen, Y., Ma, Z., Dudhia, J., Guo, Y., Zhang, X., Won, D.-J., Lin, H.-C., and Kuo, Y.-H.: Four-Dimensional Variational Data Assimilation for WRF: Formulation and Preliminary Results, *Mon. Wea. Rev.*, 137, 299–314, doi:10.1175/2008MWR2577.1, <http://dx.doi.org/10.1175/2008MWR2577.1>, 2009.
- 20 Ichoku, C., Kahn, R., and Chin, M.: Satellite contributions to the quantitative characterization of biomass burning for climate modeling, *Atmospheric Research*, 111, 1 – 28, doi:<http://dx.doi.org/10.1016/j.atmosres.2012.03.007>, <http://www.sciencedirect.com/science/article/pii/S0169809512000750>, 2012.
- Jacob, D. J., Crawford, J. H., Maring, H., Clarke, A. D., Dibb, J. E., Emmons, L. K., Ferrare, R. A., Hostetler, C. A., Russell, P. B., Singh, H. B., Thompson, A. M., Shaw, G. E., McCauley, E., Pederson, J. R., and Fisher, J. A.: The Arctic Research of the Composition of the Troposphere from Aircraft and Satellites (ARCTAS) mission: design, execution, and first results, *Atmospheric Chemistry and Physics*, 10, 5191–5212, doi:10.5194/acp-10-5191-2010, <http://www.atmos-chem-phys.net/10/5191/2010/>, 2010.
- Janssen, N. A., Gerlofs-Nijland, M. E., Lanki, T., Salonen, R. O., Cassee, F., Hoek, G., Fischer, P., Brunekreef, B., and Krzyzanowski, M.: Health effects of black carbon, World Health Organization, Regional Office for Europe, Copenhagen, [http://www.euro.who.int/\\_\\_data/assets/pdf\\_file/0004/162535/e96541.pdf](http://www.euro.who.int/__data/assets/pdf_file/0004/162535/e96541.pdf), oCLC: 930804705, 2012.
- 30 Jiang, Z., Jones, D. B. A., Worden, H. M., and Henze, D. K.: Sensitivity of top-down CO source estimates to the modeled vertical structure in atmospheric CO, *Atmospheric Chemistry and Physics*, 15, 1521–1537, doi:10.5194/acp-15-1521-2015, <http://www.atmos-chem-phys.net/15/1521/2015/>, 2015.
- Jolly, W. M., Cochrane, M. A., Freeborn, P. H., Holden, Z. A., Brown, T. J., Williamson, G. J., and Bowman, D. M. J. S.: Climate-induced variations in global wildfire danger from 1979 to 2013, *Nat Commun*, 6, <http://dx.doi.org/10.1038/ncomms8537>, 2015.
- 35 Kaiser, J. W., Heil, A., Andreae, M. O., Benedetti, A., Chubarova, N., Jones, L., Morcrette, J.-J., Razinger, M., Schultz, M. G., Suttie, M., and van der Werf, G. R.: Biomass burning emissions estimated with a global fire assimilation system based on observed fire radiative power, *Biogeosciences*, 9, 527–554, doi:10.5194/bg-9-527-2012, <http://www.biogeosciences.net/9/527/2012/>, 2012.
- Kelley, C.: *Iterative Methods for Optimization*, *Frontiers in Applied Mathematics*, Society for Industrial and Applied Mathematics, 1999.

- Kim, S.-W., McDonald, B. C., Baidar, S., Brown, S. S., Dube, B., Ferrare, R. A., Frost, G. J., Harley, R. A., Holloway, J. S., Lee, H.-J., McKeen, S. A., Neuman, J. A., Nowak, J. B., Oetjen, H., Ortega, I., Pollack, I. B., Roberts, J. M., Ryerson, T. B., Scarino, A. J., Senff, C. J., Thalman, R., Trainer, M., Volkamer, R., Wagner, N., Washenfelder, R. A., Waxman, E., and Young, C. J.: Modeling the weekly cycle of NO<sub>x</sub> and CO emissions and their impacts on O<sub>3</sub> in the Los Angeles-South Coast Air Basin during the CalNex 2010 field campaign: Modeling Weekly Cycle of the LA Air Quality in 2010, *Journal of Geophysical Research: Atmospheres*, 121, 1340–1360, doi:10.1002/2015JD024292, <http://doi.wiley.com/10.1002/2015JD024292>, 2016.
- Lauvaux, T., Miles, N. L., Deng, A., Richardson, S. J., Cambaliza, M. O., Davis, K. J., Gaudet, B., Gurney, K. R., Huang, J., O’Keefe, D., Song, Y., Karion, A., Oda, T., Patarasuk, R., Razlivanov, I., Sarmiento, D., Shepson, P., Sweeney, C., Turnbull, J., and Wu, K.: High-resolution atmospheric inversion of urban CO<sub>2</sub> emissions during the dormant season of the Indianapolis Flux Experiment (INFLUX), *Journal of Geophysical Research: Atmospheres*, pp. n/a–n/a, doi:10.1002/2015JD024473, <http://dx.doi.org/10.1002/2015JD024473>, 2016.
- Lawless, A. S., Gratton, S., and Nichols, N. K.: Approximate iterative methods for variational data assimilation, *International Journal for Numerical Methods in Fluids*, 47, 1129–1135, doi:10.1002/flid.851, <http://dx.doi.org/10.1002/flid.851>, 2005.
- Lorenc, A. C.: Optimal nonlinear objective analysis, *Quarterly Journal of the Royal Meteorological Society*, 114, 205–240, doi:10.1002/qj.49711447911, <http://dx.doi.org/10.1002/qj.49711447911>, 1988.
- Malm, W. C., Sisler, J. F., Huffman, D., Eldred, R. A., and Cahill, T. A.: Spatial and seasonal trends in particle concentration and optical extinction in the United States, *Journal of Geophysical Research: Atmospheres*, 99, 1347–1370, doi:10.1029/93JD02916, <http://dx.doi.org/10.1029/93JD02916>, 1994.
- Mandel, J., Bergou, E., Gürol, S., Gratton, S., and Kasanický, I.: Hybrid Levenberg–Marquardt and weak-constraint ensemble Kalman smoother method, *Nonlinear Processes in Geophysics*, 23, 59–73, doi:10.5194/npg-23-59-2016, <http://www.nonlin-processes-geophys.net/23/59/2016/>, 2016.
- Mao, Y. H., Li, Q. B., Zhang, L., Chen, Y., Randerson, J. T., Chen, D., and Liou, K. N.: Biomass burning contribution to black carbon in the Western United States Mountain Ranges, *Atmospheric Chemistry and Physics*, 11, 11 253–11 266, doi:10.5194/acp-11-11253-2011, <http://www.atmos-chem-phys.net/11/11253/2011/>, 2011.
- Mao, Y. H., Li, Q. B., Henze, D. K., Jiang, Z., Jones, D. B. A., Kopacz, M., He, C., Qi, L., Gao, M., Hao, W.-M., and Liou, K.-N.: Estimates of black carbon emissions in the western United States using the GEOS-Chem adjoint model, *Atmospheric Chemistry and Physics*, 15, 7685–7702, doi:10.5194/acp-15-7685-2015, <http://www.atmos-chem-phys.net/15/7685/2015/>, 2015.
- McDonald, B. C., Goldstein, A. H., and Harley, R. A.: Long-Term Trends in California Mobile Source Emissions and Ambient Concentrations of Black Carbon and Organic Aerosol, *Environmental Science & Technology*, 49, 5178–5188, doi:10.1021/es505912b, <http://pubs.acs.org/doi/abs/10.1021/es505912b>, 2015.
- Meirink, J. F., Bergamaschi, P., and Krol, M. C.: Four-dimensional variational data assimilation for inverse modelling of atmospheric methane emissions: method and comparison with synthesis inversion, *Atmospheric chemistry and physics*, 8, 6341–6353, <http://www.atmos-chem-phys.net/8/6341/>, 2008.
- Müller, J.-F. and Stavrou, T.: Inversion of CO and NO<sub>x</sub> emissions using the adjoint of the IMAGES model, *Atmospheric Chemistry and Physics*, 5, 1157–1186, <http://www.atmos-chem-phys.net/5/1157/2005/acp-5-1157-2005.html>, 2005.
- Peischl, J., Ryerson, T. B., Brioude, J., Aikin, K. C., Andrews, A. E., Atlas, E., Blake, D., Daube, B. C., de Gouw, J. A., Dlugokencky, E., Frost, G. J., Gentner, D. R., Gilman, J. B., Goldstein, A. H., Harley, R. A., Holloway, J. S., Kofler, J., Kuster, W. C., Lang, P. M., Novelli, P. C., Santoni, G. W., Trainer, M., Wofsy, S. C., and Parrish, D. D.: Quantifying sources of methane using light alkanes in the Los Angeles

- basin, California, *Journal of Geophysical Research: Atmospheres*, 118, 4974–4990, doi:10.1002/jgrd.50413, <http://dx.doi.org/10.1002/jgrd.50413>, 2013.
- Pleim, J. E.: A Simple, Efficient Solution of Flux–Profile Relationships in the Atmospheric Surface Layer, *Journal of Applied Meteorology and Climatology*, 45, 341–347, doi:10.1175/JAM2339.1, <http://dx.doi.org/10.1175/JAM2339.1>, 2006.
- 5 Pleim, J. E.: A Combined Local and Nonlocal Closure Model for the Atmospheric Boundary Layer. Part II: Application and Evaluation in a Mesoscale Meteorological Model, *Journal of Applied Meteorology and Climatology*, 46, 1396–1409, doi:10.1175/JAM2534.1, <http://journals.ametsoc.org/doi/abs/10.1175/JAM2534.1>, 2007a.
- Pleim, J. E.: A Combined Local and Nonlocal Closure Model for the Atmospheric Boundary Layer. Part I: Model Description and Testing, *Journal of Applied Meteorology and Climatology*, 46, 1383–1395, doi:10.1175/JAM2539.1, <http://journals.ametsoc.org/doi/abs/10.1175/JAM2539.1>, 2007b.
- 10 Pleim, J. E. and Gilliam, R.: An Indirect Data Assimilation Scheme for Deep Soil Temperature in the Pleim–Xiu Land Surface Model, *Journal of Applied Meteorology and Climatology*, 48, 1362–1376, doi:10.1175/2009JAMC2053.1, <http://journals.ametsoc.org/doi/abs/10.1175/2009JAMC2053.1>, 2009.
- Pleim, J. E. and Xiu, A.: Development of a land surface model. Part II: Data assimilation, *Journal of Applied Meteorology*, 42, 1811–1822, [http://journals.ametsoc.org/doi/full/10.1175/1520-0450\(2003\)042%3C1811:DOALSM%3E2.0.CO%3B2](http://journals.ametsoc.org/doi/full/10.1175/1520-0450(2003)042%3C1811:DOALSM%3E2.0.CO%3B2), 2003.
- 15 Purser, R. J. and Huang, H.-L.: Estimating Effective Data Density in a Satellite Retrieval or an Objective Analysis, *Journal of Applied Meteorology*, 32, 1092–1107, doi:10.1175/1520-0450(1993)032<1092:EEDDIA>2.0.CO;2, 1993.
- Reff, A., Bhawe, P. V., Simon, H., Pace, T. G., Pouliot, G. A., Mobley, J. D., and Houyoux, M.: Emissions Inventory of PM<sub>2.5</sub> Trace Elements across the United States, *Environmental Science & Technology*, 43, 5790–5796, doi:10.1021/es802930x, <http://pubs.acs.org/doi/abs/10.1021/es802930x>, 2009.
- 20 Reid, J. S., Hyer, E. J., Prins, E. M., Westphal, D. L., Zhang, J., Wang, J., Christopher, S. A., Curtis, C. A., Schmidt, C. C., Eleuterio, D. P., Richardson, K. A., and Hoffman, J. P.: Global Monitoring and Forecasting of Biomass-Burning Smoke: Description of and Lessons From the Fire Locating and Modeling of Burning Emissions (FLAMBE) Program, *IEEE Journal of Selected Topics in Applied Earth Observations and Remote Sensing*, 2, 144–162, doi:10.1109/JSTARS.2009.2027443, <http://ieeexplore.ieee.org/lpdocs/epic03/wrapper.htm?arnumber=5208306>, 2009.
- 25 Rodgers, C. D.: Information content and optimization of high-spectral-resolution measurements, in: *Proc. SPIE*, vol. 2830, pp. 136–147, doi:10.1117/12.256110, 1996.
- Sahu, L. K., Kondo, Y., Moteki, N., Takegawa, N., Zhao, Y., Cubison, M. J., Jimenez, J. L., Vay, S., Diskin, G. S., Wisthaler, A., Mikoviny, T., Huey, L. G., Weinheimer, A. J., and Knapp, D. J.: Emission characteristics of black carbon in anthropogenic and biomass burning plumes over California during ARCTAS-CARB 2008, *Journal of Geophysical Research*, 117, 1–20, doi:10.1029/2011JD017401, <http://doi.wiley.com/10.1029/2011JD017401>, 2012.
- 30 Saide, P. E., Peterson, D. A., da Silva, A., Anderson, B., Ziemba, L. D., Diskin, G., Sachse, G., Hair, J., Butler, C., Fenn, M., Jimenez, J. L., Campuzano-Jost, P., Perring, A. E., Schwarz, J. P., Markovic, M. Z., Russell, P., Redemann, J., Shinozuka, Y., Streets, D. G., Yan, F., Dibb, J., Yokelson, R., Toon, O. B., Hyer, E., and Carmichael, G. R.: Revealing important nocturnal and day-to-day variations in fire smoke emissions through a multiplatform inversion, *Geophysical Research Letters*, 42, 3609–3618, doi:10.1002/2015GL063737, <http://dx.doi.org/10.1002/2015GL063737>, 2015.
- 35 Song, H., Edwards, C. A., Moore, A. M., and Fiechter, J.: Data assimilation in a coupled physical–biogeochemical model of the California Current System using an incremental lognormal 4-dimensional variational approach: Part 1—Model formulation and biological data as-

- simulation twin experiments, *Ocean Modelling*, 106, 131–145, doi:10.1016/j.ocemod.2016.04.001, <http://linkinghub.elsevier.com/retrieve/pii/S1463500316300063>, 2016.
- Spracklen, D. V., Mickley, L. J., Logan, J. A., Hudman, R. C., Yevich, R., Flannigan, M. D., and Westerling, A. L.: Impacts of climate change from 2000 to 2050 on wildfire activity and carbonaceous aerosol concentrations in the western United States, *Journal of Geophysical Research*, 114, doi:10.1029/2008JD010966, <http://doi.wiley.com/10.1029/2008JD010966>, 2009.
- 5 Strand, T. M., Larkin, N., Craig, K. J., Raffuse, S., Sullivan, D., Solomon, R., Rorig, M., Wheeler, N., and Pryden, D.: Analyses of BlueSky Gateway PM2.5 predictions during the 2007 southern and 2008 northern California fires: PM2.5 PREDICTIONS DURING LARGE WILDFIRES, *Journal of Geophysical Research: Atmospheres*, 117, n/a–n/a, doi:10.1029/2012JD017627, <http://doi.wiley.com/10.1029/2012JD017627>, 2012.
- 10 Streets, D. G., Bond, T. C., Carmichael, G. R., Fernandes, S. D., Fu, Q., He, D., Klimont, Z., Nelson, S. M., Tsai, N. Y., Wang, M. Q., Woo, J.-H., and Yarber, K. F.: An inventory of gaseous and primary aerosol emissions in Asia in the year 2000, *Journal of Geophysical Research: Atmospheres*, 108, GTE30/1–GTE30/23, doi:10.1029/2002JD003093, <http://dx.doi.org/10.1029/2002JD003093>, 2003.
- Tarantola, A.: *Inverse Problem Theory and Methods for Model Parameter Estimation*, Other Titles in Applied Mathematics, Society for Industrial and Applied Mathematics, <http://dx.doi.org/10.1137/1.9780898717921>, DOI: 10.1137/1.9780898717921 DOI: 10.1137/1.9780898717921, 2005.
- 15 Thacker, W. C.: The role of the Hessian matrix in fitting models to measurements, *Journal of Geophysical Research: Oceans*, 94, 6177–6196, doi:10.1029/JC094iC05p06177, <http://dx.doi.org/10.1029/JC094iC05p06177>, 1989.
- Tshimanga, J., Gratton, S., Weaver, A. T., and Sartenaer, A.: Limited-memory preconditioners, with application to incremental four-dimensional variational data assimilation, *Quarterly Journal of the Royal Meteorological Society*, 134, 751–769, doi:10.1002/qj.228, <http://doi.wiley.com/10.1002/qj.228>, 2008.
- 20 van der Werf, G. R., Randerson, J. T., Giglio, L., Collatz, G. J., Mu, M., Kasibhatla, P. S., Morton, D. C., DeFries, R. S., Jin, Y., and van Leeuwen, T. T.: Global fire emissions and the contribution of deforestation, savanna, forest, agricultural, and peat fires (1997-2009), *Atmospheric Chemistry and Physics*, 10, 11 707–11 735, doi:10.5194/acp-10-11707-2010, <http://www.atmos-chem-phys.net/10/11707/2010/>, 2010.
- 25 Wahba, G.: Design Criteria and Eigensequence Plots for Satellite-Computed Tomography, *Journal of Atmospheric and Oceanic Technology*, 2, 125–132, doi:10.1175/1520-0426(1985)002<0125:DCAEPF>2.0.CO;2, [http://dx.doi.org/10.1175/1520-0426\(1985\)002<0125:DCAEPF>2.0.CO;2](http://dx.doi.org/10.1175/1520-0426(1985)002<0125:DCAEPF>2.0.CO;2), 1985.
- Weaver, A. T., Deltel, C., Machu, E., Ricci, S., and Daget, N.: A multivariate balance operator for variational ocean data assimilation, *Quarterly Journal of the Royal Meteorological Society*, 131, 3605–3625, doi:10.1256/qj.05.119, <http://doi.wiley.com/10.1256/qj.05.119>, 2005.
- 30 Wecht, K. J., Jacob, D. J., Sulprizio, M. P., Santoni, G. W., Wofsy, S. C., Parker, R., Bösch, H., and Worden, J.: Spatially resolving methane emissions in California: constraints from the CalNex aircraft campaign and from present (GOSAT, TES) and future (TROPOMI, geostationary) satellite observations, *Atmospheric Chemistry and Physics*, 14, 8173–8184, doi:10.5194/acp-14-8173-2014, <http://www.atmos-chem-phys.net/14/8173/2014/>, 2014.
- 35 Wesely, M. L.: Parameterization of surface resistances to gaseous dry deposition in regional-scale numerical models, *Atmospheric Environment* (1967), 23, 1293 – 1304, doi:[http://dx.doi.org/10.1016/0004-6981\(89\)90153-4](http://dx.doi.org/10.1016/0004-6981(89)90153-4), <http://www.sciencedirect.com/science/article/pii/0004698189901534>, 1989.

- Wiedinmyer, C., Quayle, B., Geron, C., Belote, A., McKenzie, D., Zhang, X., O'Neill, S., and Wynne, K. K.: Estimating emissions from fires in North America for air quality modeling, *Atmospheric Environment*, 40, 3419–3432, doi:10.1016/j.atmosenv.2006.02.010, <http://linkinghub.elsevier.com/retrieve/pii/S1352231006002032>, 2006.
- Wiedinmyer, C., Akagi, S. K., Yokelson, R. J., Emmons, L. K., Al-Saadi, J. A., Orlando, J. J., and Soja, A. J.: The Fire INventory from NCAR (FINN): a high resolution global model to estimate the emissions from open burning, *Geoscientific Model Development*, 4, 625–641, doi:10.5194/gmd-4-625-2011, <http://www.geosci-model-dev.net/4/625/2011/>, 2011.
- WRAP: 2002 Fire Emission Inventory for the WRAP Region - Phase II, Tech. Rep. Project No. 178-6, Prepared by Air Sciences, Inc., <http://www.wrapair.org/forums/fejftasks/FEJFtask7PhaseII.html>, 2005.
- Wu, J., Winer, A. M., and Delfino, R. J.: Exposure assessment of particulate matter air pollution before, during, and after the 2003 Southern California wildfires, *Atmospheric Environment*, 40, 3333 – 3348, doi:<http://dx.doi.org/10.1016/j.atmosenv.2006.01.056>, <http://www.sciencedirect.com/science/article/pii/S135223100600197X>, 2006.
- Xiu, A. and Pleim, J. E.: Development of a land surface model. Part I: Application in a mesoscale meteorological model, *Journal of Applied Meteorology*, 40, 192–209, [http://journals.ametsoc.org/doi/abs/10.1175/1520-0450\(2001\)040%3C0192:DOALSM%3E2.0.CO%3B2](http://journals.ametsoc.org/doi/abs/10.1175/1520-0450(2001)040%3C0192:DOALSM%3E2.0.CO%3B2), 2001.
- 15 Yang, E.-G., Kim, H. M., Kim, J., and Kay, J. K.: Effect of Observation Network Design on Meteorological Forecasts of Asian Dust Events, *Monthly Weather Review*, 142, 4679–4695, doi:10.1175/MWR-D-14-00080.1, <http://journals.ametsoc.org/doi/abs/10.1175/MWR-D-14-00080.1>, 2014.
- Yelverton, T. L., Hays, M. D., Gullett, B. K., and Linak, W. P.: Black Carbon Measurements of Flame-Generated Soot as Determined by Optical, Thermal-Optical, Direct Absorption, and Laser Incandescence Methods, *Environmental Engineering Science*, 31, 209–215, doi:10.1089/ees.2014.0038, <http://online.liebertpub.com/doi/abs/10.1089/ees.2014.0038>, 2014.
- Zhang, F., Wang, J., Ichoku, C., Hyer, E. J., Yang, Z., Ge, C., Su, S., Zhang, X., Kondragunta, S., Kaiser, J. W., Wiedinmyer, C., and da Silva, A.: Sensitivity of mesoscale modeling of smoke direct radiative effect to the emission inventory: a case study in northern sub-Saharan African region, *Environmental Research Letters*, 9, 075 002, doi:10.1088/1748-9326/9/7/075002, <http://stacks.iop.org/1748-9326/9/i=7/a=075002?key=crossref.c3a057c1cb5936f978ecde79c6fa7281>, 2014a.
- 25 Zhang, X., Kondragunta, S., Ram, J., Schmidt, C., and Huang, H.-C.: Near-real-time global biomass burning emissions product from geostationary satellite constellation: GLOBAL BIOMASS BURNING EMISSIONS, *Journal of Geophysical Research: Atmospheres*, 117, n/a–n/a, doi:10.1029/2012JD017459, <http://doi.wiley.com/10.1029/2012JD017459>, 2012.
- Zhang, X., Huang, X.-Y., and Pan, N.: Development of the Upgraded Tangent Linear and Adjoint of the Weather Research and Forecasting (WRF) Model, *J. Atmos. Oceanic Technol.*, 30, 1180–1188, doi:10.1175/JTECH-D-12-00213.1, <http://dx.doi.org/10.1175/JTECH-D-12-00213.1>, 2013.
- 30 Zhang, X., Huang, X.-Y., Liu, J., Poterjoy, J., Weng, Y., Zhang, F., and Wang, H.: Development of an Efficient Regional Four-Dimensional Variational Data Assimilation System for WRF, *Journal of Atmospheric and Oceanic Technology*, 31, 2777–2794, doi:10.1175/JTECH-D-13-00076.1, <http://journals.ametsoc.org/doi/abs/10.1175/JTECH-D-13-00076.1>, 2014b.



**Table 1.** Emission inversion scenarios.

	Scenario	BB Inventory	$L_h$	Obs. Used (day)
22 June	FINN_STD	FINNv1.0	36 km	ARCTAS-CARB (22)
	FINN_L18	FINNv1.0	18 km	ARCTAS-CARB (22)
	QFED_STD	QFEDv2.4r8	36 km	ARCTAS-CARB (22)
	QFED_L18	QFEDv2.4r8	18 km	ARCTAS-CARB (22)
	FINN_V1.5	FINNv1.5	36 km	ARCTAS-CARB (22)
23/24 June	FINN_STD	FINNv1.0	36 km	IMPROVE (23) & ARCTAS-CARB (24)
	QFED_STD	QFEDv2.4r8	36 km	IMPROVE (23) & ARCTAS-CARB (24)
	ACFT	FINNv1.0	36 km	ARCTAS-CARB (24)
	SURF	FINNv1.0	36 km	IMPROVE (23)

**Table 2.** Aircraft observation linear regression characteristics for the prior (background, b) and posterior (analysis, a).

Obs. Date → Inversion Scenario ↓		22 June, $N_{\text{obs}} = 241$				24 June, $N_{\text{obs}} = 301$				26 June, $N_{\text{obs}} = 117$			
		$R^2$		slope		$R^2$		slope		$R^2$		slope	
		b	a	b	a	b	a	b	a	b	a	b	a
22 June	FINN_STD	0.11	<b>0.82</b>	0.26	<b>0.80</b>	0.18	0.15	0.38	0.25	0.56	0.52	0.15	<b>0.49</b>
	QFED_STD	0.03	<b>0.73</b>	0.34	<b>0.71</b>	0.15	0.23	0.43	0.37	0.59	0.53	0.39	0.43
23/24 June	FINN_STD	-	-	-	-	0.17	<b>0.52</b>	0.35	<b>0.56</b>	0.59	0.16	0.15	0.11
	QFED_STD	-	-	-	-	0.11	<b>0.52</b>	0.36	<b>0.55</b>	0.63	0.44	0.41	0.15
	ACFT	-	-	-	-	0.17	<b>0.53</b>	0.35	<b>0.57</b>	0.59	0.29	0.15	0.08
	SURF	-	-	-	-	0.17	0.17	0.35	0.40	0.59	0.13	0.15	0.17

**distinct improvement**; *distinct degradation*; cross validation

**Table 3.** Surface observation linear regression characteristics for the prior (background, b) and posterior (analysis, a).

Obs. Date → Inversion Scenario ↓		23 June, $N_{\text{obs}} = 35$				26 June, $N_{\text{obs}} = 36$			
		$R^2$		slope		$R^2$		slope	
		b	a	b	a	b	a	b	a
22 June	FINN_STD	0.06	0.04	0.26	0.21	0.03	0.05	0.10	0.13
	QFED_STD	0.16	0.14	0.44	0.41	0.10	0.11	0.20	0.21
23/24 June	FINN_STD	0.04	<b>0.75</b>	0.25	<b>1.04</b>	0.03	<b>0.28</b>	0.10	<b>0.28</b>
	QFED_STD	0.09	<b>0.74</b>	0.39	<b>1.01</b>	0.09	0.15	0.20	0.16
	ACFT	0.04	0.05	0.25	0.27	0.03	0.03	0.10	0.09
	SURF	0.04	<b>0.74</b>	0.25	<b>1.02</b>	0.03	<b>0.35</b>	0.10	<b>0.35</b>

**distinct improvement;** *distinct degradation*; cross validation

**Table 4.** Emission area coordinates. EA1-4 are used for BB totals and EA5-9 are used for anthropogenic totals.

	$\text{LON}_{\text{min}}$	$\text{LON}_{\text{max}}$	$\text{LAT}_{\text{min}}$	$\text{LAT}_{\text{max}}$
EA1	122.5°W	120.5°W	35.7°N	38.5°N
EA2	123.8°W	122.1°W	38.9°N	40.4°N
EA3	124.3°W	122.9°W	40.4°N	41.7°N
EA4	122.1°W	120.0°W	38.5°N	40.4°N
EA5	117.8°W	116.9°W	32.1°N	33.4°N
EA6	121.0°W	117.8°W	33.4°N	34.6°N
EA7	123.0°W	121.0°W	36.6°N	38.8°N
EA8	120.6°W	118.6°W	35.2°N	37.0°N
EA9	118.0°W	116.5°W	34.0°N	36.0°N
EA10	116.9°W	115.0°W	32.1°N	33.4°N

**Table 5.** Total BB emissions for EA's and domain-wide during 22 and 23/24 June inversions (averaged for 24 hour period). Absolute units are in Mg. Note, the differences ( $\Delta$ ) may not sum due to rounding.

		FINN_STD			QFED_STD			$\frac{\Sigma E_{\text{QFED}}}{\Sigma E_{\text{FINN}}}$	
		$\Sigma E_b$	$\Sigma E_a$	$\Delta$	$\Sigma E_b$	$\Sigma E_a$	$\Delta$	b	a
22 June	EA1	14	4	-10	82	26	-55	$\times 5.8$	$\times 6.4$
	EA2	6	30	+24	9	15	+6	$\times 1.5$	$\times 0.5$
	EA3	6	4	-2	29	7	-22	$\times 4.5$	$\times 1.6$
	EA4	18	22	+4	52	83	+31	$\times 2.8$	$\times 3.8$
	DOMAIN	59	83	+34	209	171	-38	$\times 3.5$	$\times 2.1$
23+24 June	EA1	20	5	-15	70	12	-58	$\times 3.5$	$\times 2.5$
	EA2	28	11	-16	96	29	-67	$\times 3.5$	$\times 2.6$
	EA3	17	12	-5	37	20	-17	$\times 2.2$	$\times 1.7$
	EA4	32	108	+77	107	107	0	$\times 3.4$	$\times 1.0$
	DOMAIN	138	249	+111	471	354	-117	$\times 3.4$	$\times 1.4$

**Table 6.** Total anthropogenic emissions for EA's and domain-wide during 22 and 23/24 June inversions (averaged for 24 hour period). The posterior for 23/24 June is from an inversion using both the IMPROVE and ARACTAS-CARB observations. Results shown are for the FINN\_STD scenario. Absolute units are in Mg. Note, the differences ( $\Delta$ ) may not sum due to rounding.

	22 June			23/24 June			$\frac{\Sigma E_{23+24 \text{ June}}}{\Sigma E_{22 \text{ June}}}$	
	$\Sigma E_b$	$\Sigma E_a$	$\Delta$	$\Sigma E_b$	$\Sigma E_a$	$\Delta$	b	a
EA5	5	5	0	7	3	-3	$\times 1.4$	$\times 0.7$
EA6	12	8	-4	17	9	-8	$\times 1.4$	$\times 1.2$
EA7	10	6	-5	16	8	-8	$\times 1.6$	$\times 1.5$
EA8	3	2	-1	5	25	+20	$\times 1.6$	$\times 9.9$
EA9	5	4	-1	6	11	+4	$\times 1.3$	$\times 2.7$
EA10	2	2	0	3	8	+5	$\times 1.4$	$\times 3.7$
DOMAIN	81	68	-13	114	123	+9	$\times 1.4$	$\times 1.8$

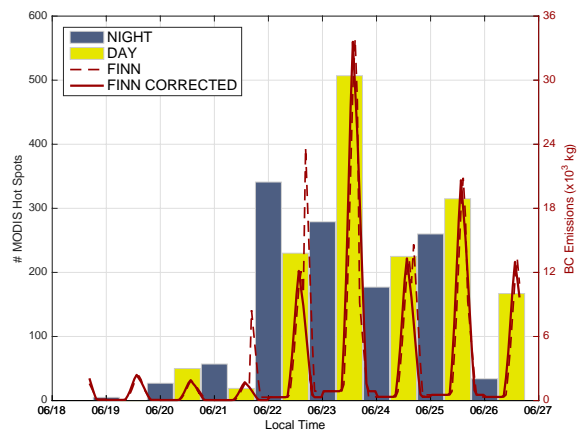


**Figure 1.** MODIS fire hot spot detections, excluding those with confidence less than or equal to 20% and double detections within 1.2 km of each other (left axis) and domain-wide FINNv1.0 BB emissions during the ARCTAS-CARB campaign, with and without fixes described in Sec. 2.2 (right axis).

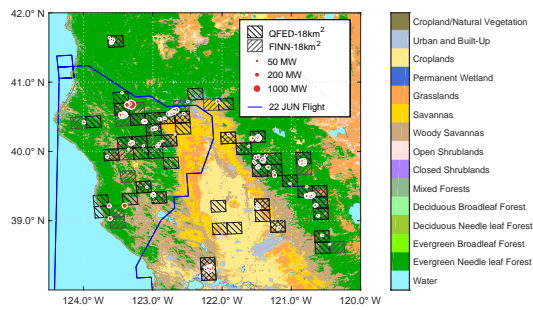


**Figure 2.** Land category types, MODIS fire hot spot detections on 21 and 22 June, 2008, sized by FRP, and 18 km × 18 km gridded FINNv1.0 and QFED emission locations.

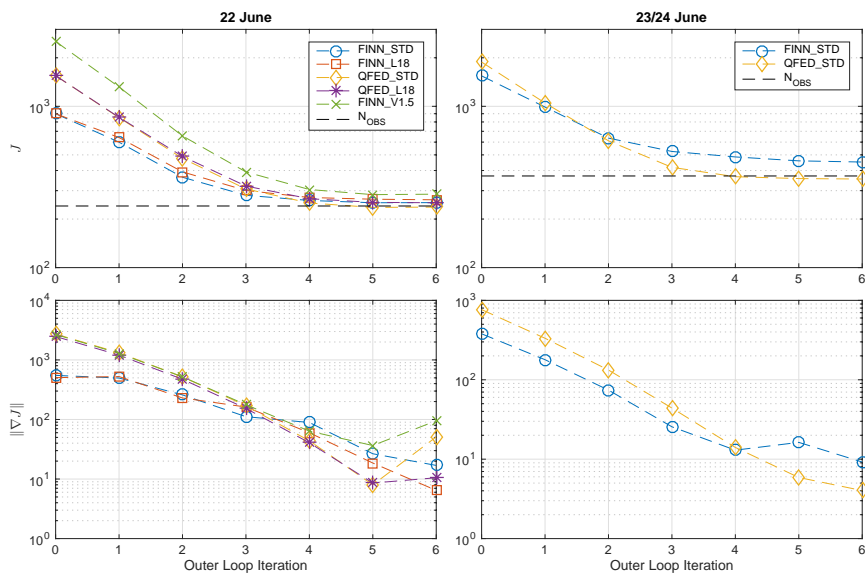


**Figure 3.** Outer loop cost function and gradient norm evaluations for the June 22 (left column) and 23/24 June (right column) inversions.

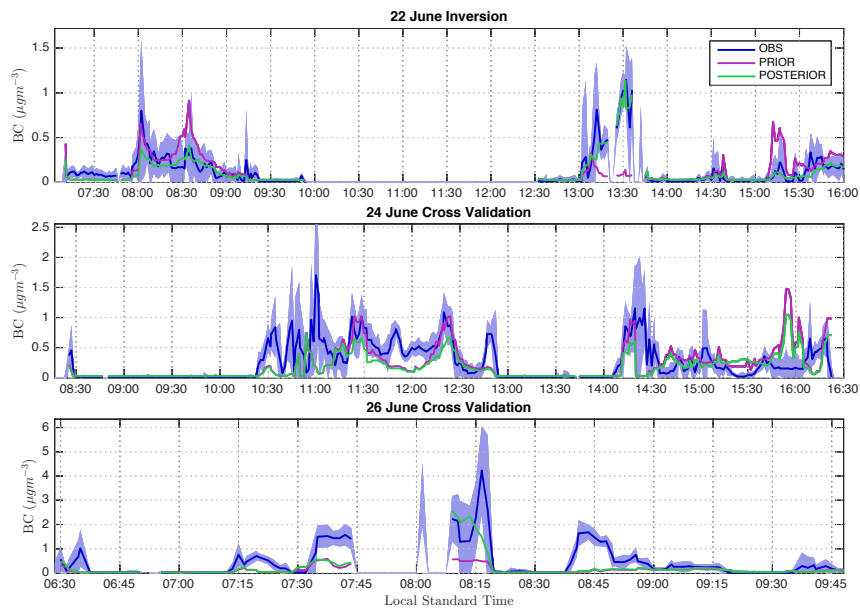


**Figure 4.** Temporal variation of observed, prior, and posterior BC concentrations during ARCTAS-CARB. The model values are obtained with the FINN\_STD inversion scenario. The shaded area encompasses 2 standard deviations around the observations, which includes both model and observation uncertainty.

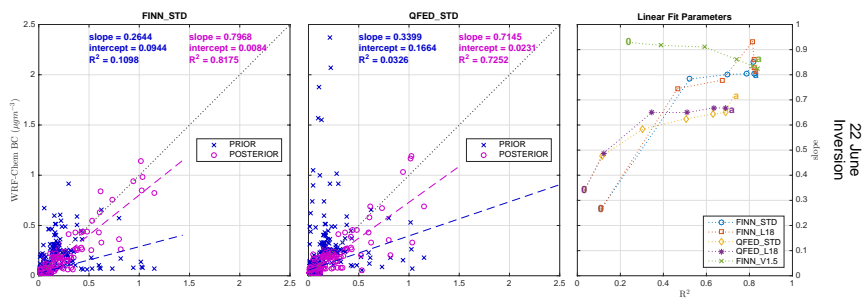
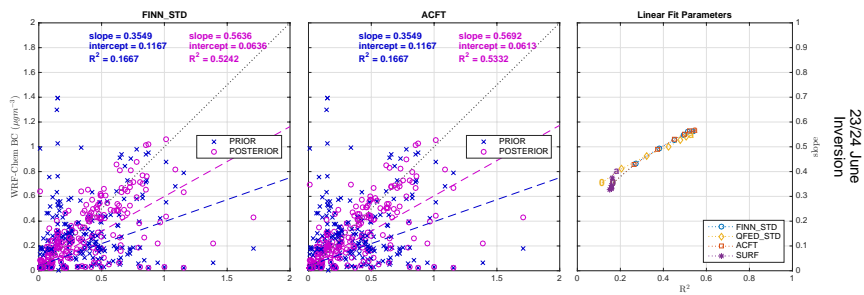


**Figure 5.** Prior and posterior model versus 22 June ARCTAS-CARB observations for the 22 June inversion. The left two plots are for FINN\_STD and QFED\_STD. The plot on the right shows the progression of slope and  $R^2$  from the prior, “0”, to the posterior, “a”, for similar linear regressions in all scenarios.





23/24 June  
Inversion

**Figure 6.** Prior and posterior model versus 24 June ARCTAS-CARB observations for the 23/24 June FINN\_STD inversion. The left plot uses both IMPROVE (23 June) and ARCTAS-CARB observations in the inversion. The middle plot uses only ARCTAS-CARB. The plot on the right shows the progression of slope and  $R^2$  from the prior, “0”, to the posterior, “a”, for similar linear regressions.

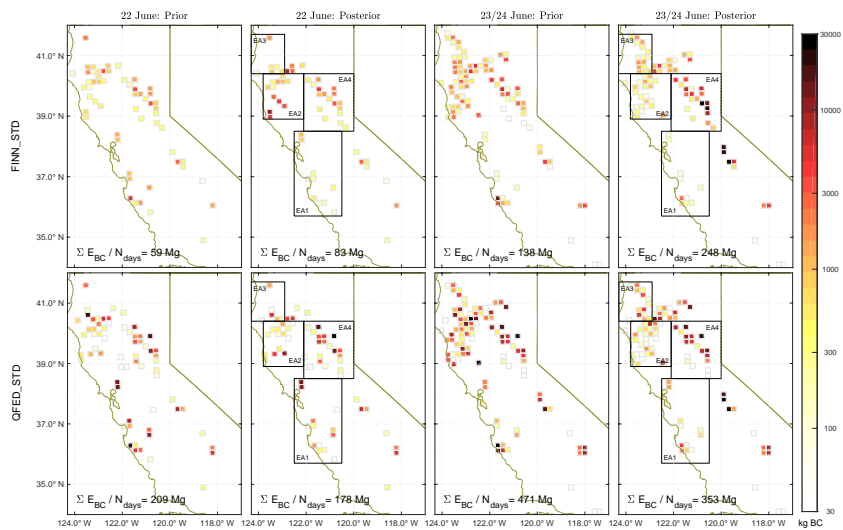


**Figure 7.** Prior and posterior grid-scale BB emissions of BC per 24 hours for FINN\_STD and QFED\_STD on 22 June, 00Z-23Z and 23 June, 00Z - 24 June 23Z. All emissions are expressed for a 24 h average. EA1-4 are outlined with black boxes.[NOTE on Figures 2, 7 and 8: we are waiting on results from QFED\_STD with IMPROVE obs included.]

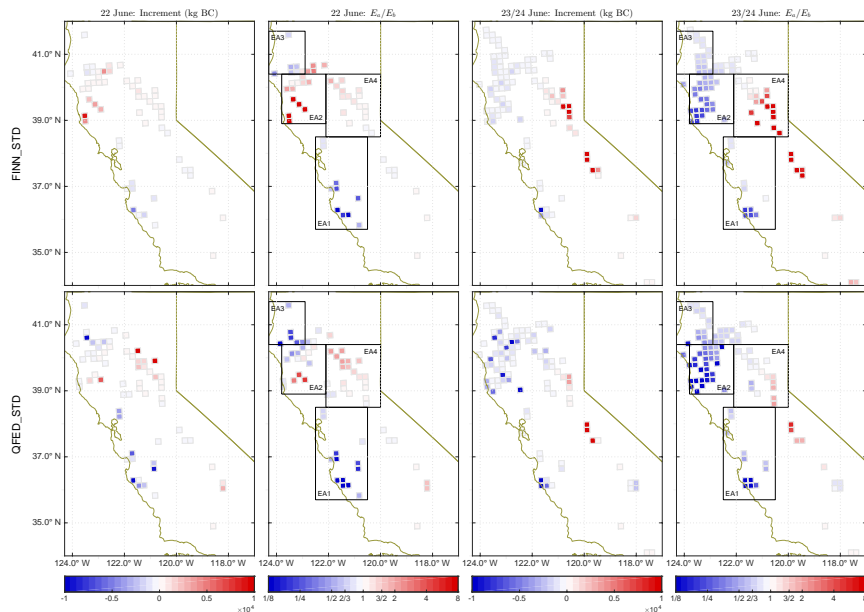


**Figure 8.** BB analysis increment (posterior minus prior) per 24 hours and posterior linear scaling factor ( $\beta$ ) for the two primary BB scenarios on 22 June 00Z-23Z and 23 June, 00Z - 24 June 23Z. EA1-4 are outlined with black boxes. [NOTE on Figures 2, 7 and 8: we are waiting on results from QFED\_STD with IMPROVE obs included.]

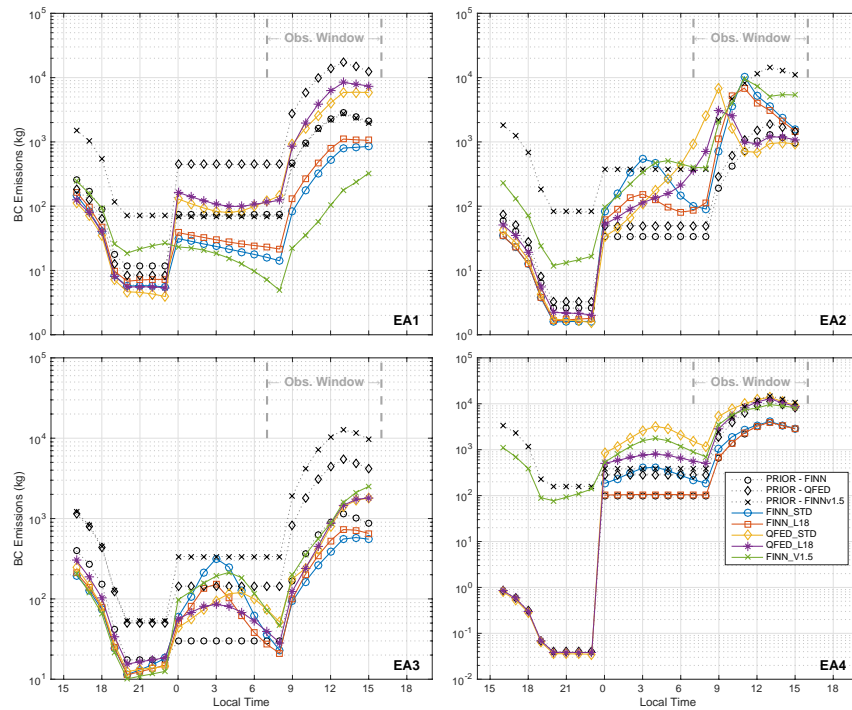


**Figure 9.** Hourly ~~prior and posterior~~ BB diurnal emission patterns for the four EAs and all inversion scenarios for 22 June, 00Z-23Z, with the time shown in LT. The priors are shown as black lines, while the posteriors from specific inversion scenarios are shown in color. Note that FINNV1.0 did not have any fires in EA4 on 21 June.

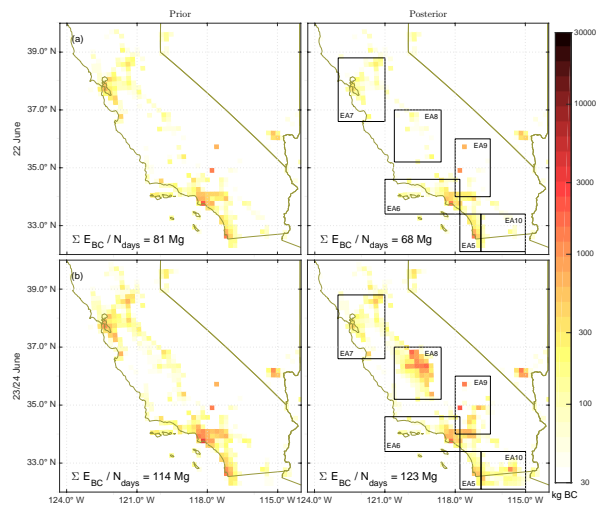


**Figure 10.** Prior and posterior grid-scale anthropogenic emissions of BC per 24 hours for FINN\_STD on 22 June, 00Z-23Z (top row) and 23 June, 00Z to 24 June, 23Z. EA5-10 are outlined with black boxes.

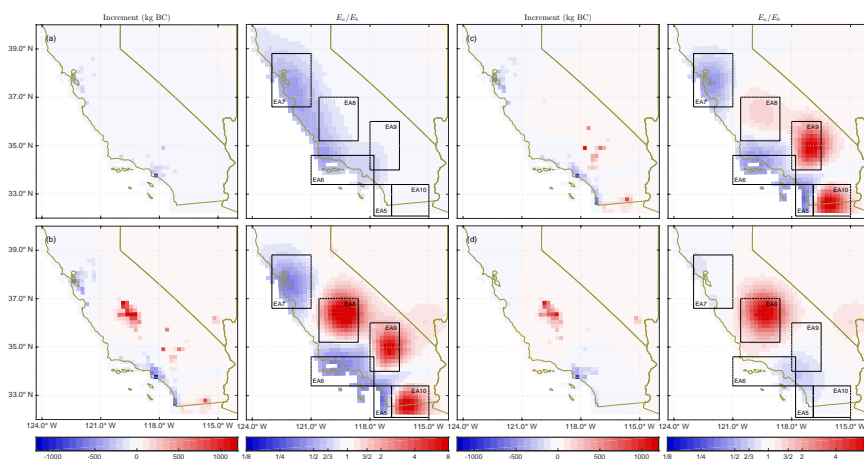


**Figure 11.** Anthropogenic analysis increment (posterior minus prior) per 24 hours and posterior linear scaling factor ( $\beta$ ) for the (a) FINN\_STD (22), (b) FINN\_STD (23/24), (c) ACFT, and (d) SURF inversion scenarios. EA5-9 are outlined with black boxes in the scaling factor plots.

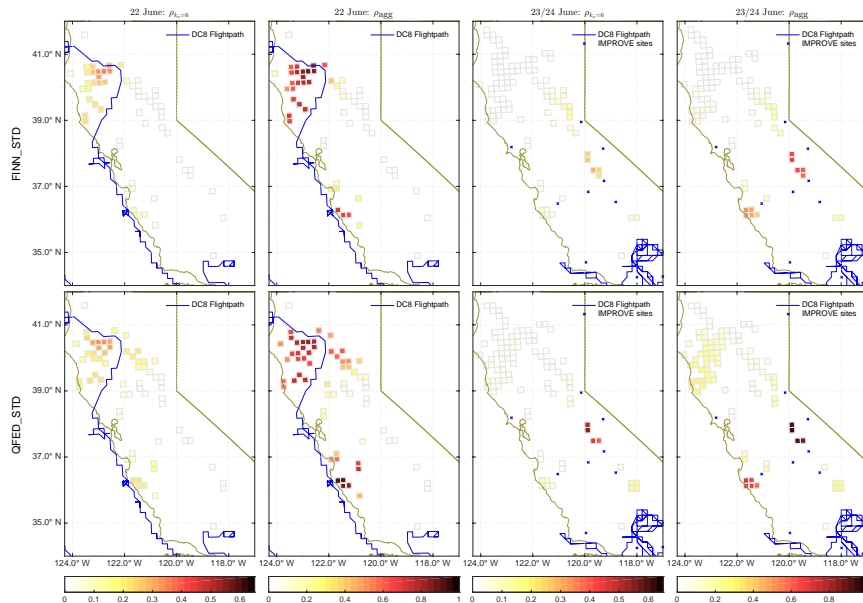


**Figure 12.** BB error reduction in the final outer loop ( $\rho_{k_o=6}$ ) and aggregated across all outer loops ( $\rho_{agg}$ ) for the two primary BB scenarios on 22 June 00Z-23Z and 23 June, 00Z - 24 June 23Z. The ARCTAS-CARB DC8 flightpath and IMPROVE sites at model grid centers are overlaid.

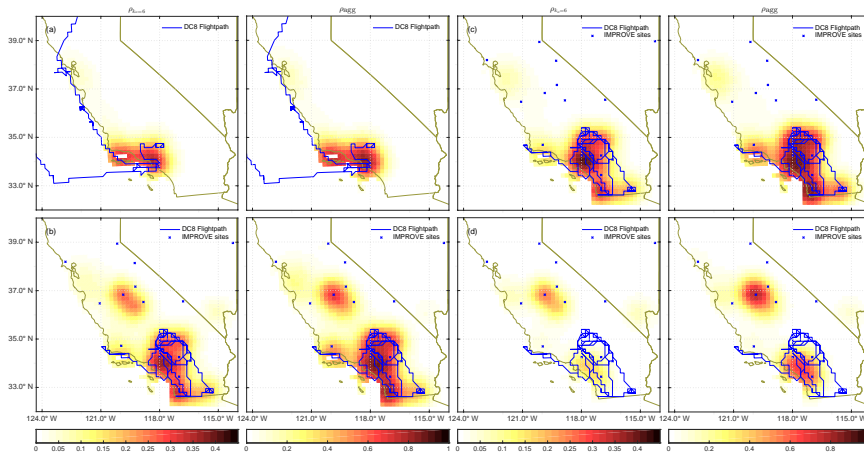


**Figure 13.** Anthropogenic error reduction in the final outer loop ( $\rho_{k_0=6}$ ) and aggregated across all outer loops ( $\rho_{agg}$ ) for the (a) FINN\_STD (22), (b) FINN\_STD (23/24), (c) ACFT, and (d) SURF inversion scenarios. The ARCTAS-CARB DC8 flightpath and IMPROVE sites at model grid centers are overlaid.



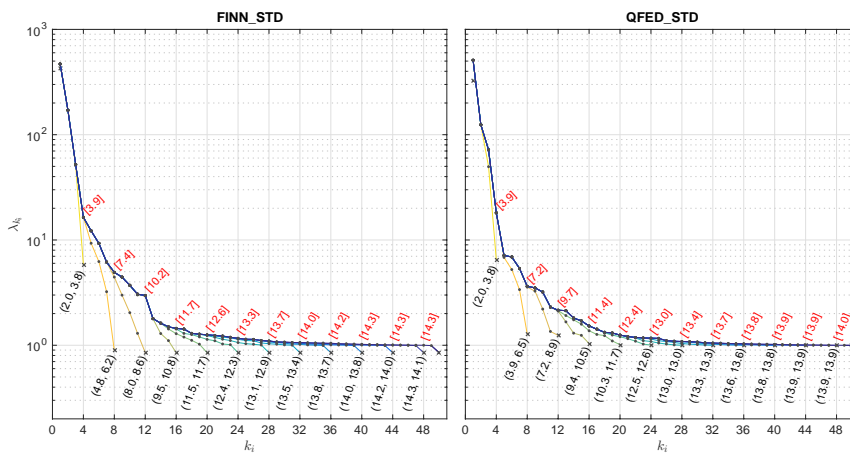


**Figure 14.** Eigenvalue spectra for FINN\_STD and QFED\_STD in the final outer loop on 22 June. The lines show the estimate of the spectrum  $[\lambda_1, \dots, \lambda_{k_i=l}]$  in every fourth inner loop iteration,  $l$ . The black numbers in parentheses are the estimates of DOF that include eigenvalues in the sets (converged to within 5% of the previous estimate, all available). The red numbers in brackets are the truncated estimates of DOF using the most completely converged set of eigenvalues available in the 50<sup>th</sup> iteration.

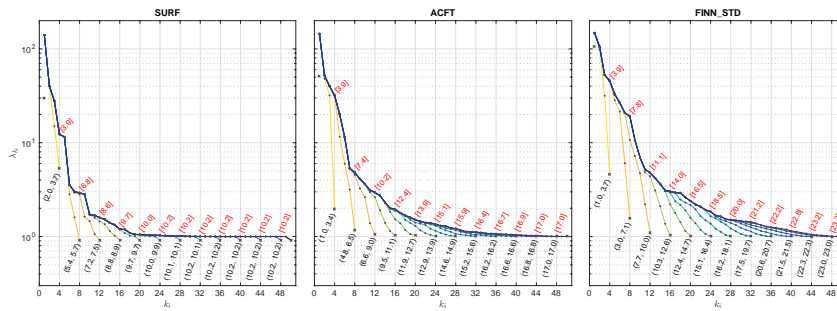


**Figure 15.** Eigenvalue spectra for SURF, ACFT, and SURF+ACFT in the final outer loop on 23 and 24 June. The lines show the estimate of the spectrum  $[\lambda_1, \dots, \lambda_{k_i=l}]$  in every fourth inner loop iteration,  $l$ . The black numbers in parentheses are the estimates of DOF that include eigenvalues in the sets (converged to within 5% of the previous estimate, all available). The red numbers in brackets are the truncated estimates of DOF using the most completely converged set of eigenvalues available in the 50<sup>th</sup> iteration.